UC Davis
UC Davis Electronic Theses and Dissertations

Title
Functional Photonic Integrated Circuits Based on Advanced Three-Dimensional Photonic Packaging

Permalink
https://escholarship.org/uc/item/91t489m0

Author
Ling, Yi-Chun

Publication Date
2023

Peer reviewed|Thesis/dissertation

eScholarship.org Powered by the California Digital Library
University of California

Functional Photonic Integrated Circuits Based on Advanced Three-Dimensional Photonic Packaging

By

YI-CHUN LING

DISSERTATION

Submitted in partial satisfaction of the requirements for the degree of

DOCTOR OF PHILOSOPHY

in

Electrical and Computer Engineering

in the

OFFICE OF GRADUATE STUDIES

of the

UNIVERSITY OF CALIFORNIA

DAVIS

Approved:

S. J. Ben Yoo, Chair

J. Sebastian Gomez-Diaz

Marina Radulaski

Committee in Charge

2023

Copyright © 2023 by
Yi-Chun Ling
All rights reserved.

To my parents, Wen-Chang Ling and Yu-Li Huang

Contents

List of Figures . . . vi
List of Tables . . . xvii
Abstract . . . xviii
Acknowledgments . . . xix

1 Background and Motivation **1**
1.1 Photonic packaging using ultrafast laser inscription . . . 2
1.2 Beam steering using optical phased arrays . . . 3
1.3 Compact integrated imaging system using metalenses . . . 4
1.4 Dissertation outline . . . 5

2 Three-Dimensional Photonic Integrated Devices Fabricated by Ultrafast Laser Inscription **6**
2.1 Principle . . . 6
2.2 Arbitrary vertical low-loss waveguides in deposited oxide of optical interposers for low-loss 3D photonic packaging . . . 8
2.2.1 System setup for ultrafast laser inscription . . . 9
2.2.2 Characterization of ULI straight waveguides on deposited oxide of optical interposers . . . 11
2.2.3 Characterization of ULI bending waveguides on deposited oxide of optical interposers . . . 15
2.2.4 Initial integration of SiN waveguides with 3D ULI waveguides through chip-to-chip coupling . . . 22
2.2.5 Alignment of SiN waveguides and 3D ULI waveguides on the same chip for ultimate intra-chip coupling . . . 24
2.2.6 Summary . . . 27
2.3 Low-loss three-dimensional fan-in/fan-out devices for multi-core fiber integration . . . 28

2.3.1 ULI system upgrade with a second-harmonic generator 29
2.3.2 Characterization of ULI waveguides inscribed by second harmonic light 30
2.3.3 Design of three-dimensional fan-in/fan-out devices for multi-core fiber integration 33
2.3.4 Fabrication and characterization results 34
2.3.5 Summary 36
2.4 Three-dimensional arrayed waveguide grating routers fabricated by ultrafast laser inscription 37
2.4.1 Arrayed waveguide grating 37
2.4.2 Design and simulation 38
2.4.3 Layout and fabrication 41
2.4.4 Characterization results 43
2.4.5 Summary 44

3 Non-Mechanical Beam Steering Using Optical Phased Array 45
3.1 Principles 45
3.2 Subwavelength silicon optical phase array with large field-of-view for near-infrared beam steering 47
3.2.1 Optimization of waveguide design 47
3.2.2 Optimization of multimode interference splitters and distributed bragg reflectors 49
3.2.3 Gratings with large emitting aperture 51
3.2.4 Component characterization 52
3.2.5 Beam steering characterization 54
3.2.6 Summary 57
3.3 Optical phased array beam steering in the mid-infrared on germanium-silicon photonic platform 58
3.3.1 Vertical emitter design 58
3.3.2 Beam steering experiments for light grating emitters 63

3.3.3 Optimization for performance of grating emitters 66
3.3.4 Design of 45-degree reflectors using focused-ion-beam etching . . . 69
3.3.5 Light grating emitters for long-wave infrared 70
3.3.6 Summary 74
3.4 Foundry-compatible two-dimensional optical phase array 75
3.4.1 3.8 μm lateral-PEPA design with AIM Photonics compatibility . . 77
3.4.2 4.6 μm lateral-PEPA design with AIM Photonics compatibility . . 78
3.4.3 Layouts and packaging 80
3.4.4 Experimental setup and characterization 82
3.4.5 Summary 85

4 Highly-Dispersive Polarization-Diversifying Metalens for Hyperspectral Imaging 86
4.1 Compressive hyperspectral imaging 86
4.2 Design of polarization diversifying highly-dispersive metalens 87
4.3 Characterization results of on-axis and off-axis metalenses 91
4.4 Summary 95

5 Conclusion and Future Directions 96

List of Figures

1.1 Schematic of (a) inter-chip interconnects on a silicon photonic integrated circuit [1] and (b) light detection and ranging (LIDAR) system [2]. 1

1.2 Demonstration of (a) a 2D-3D fan-in fan-out chip [3] and (b) a photonic wire-bonding technique [4] using ultrafast laser inscription. 2

1.3 Schematic of an OPA photonic integrated circuit (PIC) based on grating emitters for two-dimensional beam steering. 3

1.4 (a) Illustration of the concept of vertically stacking metalenses to build an ultrathin multifunctional optical system [5]. (b) Schematic of an achromatic metalens [6]. 4

2.1 Schematic diagram of 3D waveguide writing by ultrafast laser inscription. 6

2.2 Schematic diagram of the multi-scan technique 7

2.3 (a) Schematics of packaged photonic and electronic convergence system with 3D ULI waveguides for optical coupling. (b) Cross-sectional SEM pictures of deposited oxide cladding on a silicon substrate. (c) Measured wafer bow as a function of deposited oxide thickness. Schematic of (d) intra-chip and (e) chip-to-chip light coupling using 3D ULI waveguides. . 8

2.4 (a) Ultrafast laser inscription system. (b) Laser inscription on a glass substrate using a high NA objective lens. 9

2.5 (a-b) The optical setup and (c-d) the corresponding layouts on the optical bench and the wall, respectively. 10

2.6 Measurement setups for (a) optical loss and (b) optical mode profiles. (c) Top view of fabricated ULI waveguides under different exposure conditions. 11

2.7 The cross-sections of fabricated ULI waveguides on deposited 40 μm thick oxide samples under various inscription conditions. 12

2.8 Measured mode profiles of fabricated ULI waveguides on deposited 40 μm thick oxide samples under various inscription conditions. 12

2.9 (a) Measured propagation loss and (b) coupling loss of ULI waveguides on deposited 40 μm thick oxide sample as a function of the pulse energy at different scan speeds. These waveguides were fabricated by 11 scans. . . . 14

2.10 (a) Configuration of S-shaped waveguide. (b) Measurement setup. (c) Measured mode profile of a fabricated ULI waveguide on a Eagle glass sample using a scan speed of 3 mm/s and a pulse energy of 260 nJ. (d) Measured bending loss as a function of the bending angle for the bending radii of 10 mm and 20 mm. 15

2.11 (a) Measured mode profile of a fabricated ULI waveguide on a Eagle glass sample using a scan speed of 3 mm/s and a pulse energy of 260 nJ. (b) Measured bending loss as a function of the bending angle for the bending radii of 20 mm, 40 mm, and 60 mm. 17

2.12 The schematic of laser inscription for bending structures along (a) the horizontal and (b) vertical directions, respectively. (c) Captured microscope image and (d) measured mode profile of a fabricated ULI waveguide on a Eagle glass sample using a scan speed of 3 mm/s and a pulse energy of 260 nJ. (e) Measured bending loss as a function of the bending angle for a bending radius of 20 mm. 18

2.13 (a) Cross-sections of ULI waveguides at various depths within the deposited oxide. The corresponding measured mode profiles of a fabricated ULI waveguide at depths of (b) 10 μm, (c) 15 μm, (d) 20 μm, and (e) 25 μm. (f) Measured total insertion loss as a function of the waveguide depth (inset: captured microscope image of a fabricated ULI waveguide on deposited oxide using a scan speed of 3 mm/s and a pulse energy of 260 nJ). 19

2.14 (a) Schematic of a vertical S-shaped bending waveguide on deposited oxide.(b) Two ends of a fabricated S-shaped waveguide, spanning a depth range from 11 μm to 17 μm. (c) Measured mode profiles of ULI waveguides within the depth range of 16 μm to 25 μm 21

2.15 (a) Perspective-view schematic of SiN-to-ULI waveguide coupling structure. (b) Simulated coupling loss for various taper length and taper tip width. (c) Experimental setup for the loss measurement of a SiN waveguide. (d) Microscopic image for the top view of the SiN chip. (e) Top-view SEM picture of fabricated SiN taper tip. (f) Mode profile of SiN inverse taper captured by a CCD camera at 1550 nm. 23
2.16 (a) Schematic of initial coupling loss measurements between the SiN coupler and the ULI waveguide on two separate chips. (b) Experimental setup for SiN-ULI waveguide butt-coupling. (c) Alignment of the two chips and the two fibers by the use of a red laser. (d) Measured SiN chip to 3D chip coupling loss as a function of offset in horizontal and vertical directions. . 24
2.17 (a) Schematic of intra-chip coupling between SiN couplers and 3D ULI waveguides. (b) Layout of SiN couplers at the depth of 10 μm (purple), 20 μm (red), and 30 μm (blue) within the deposited oxide for intra-chip coupling with 3D ULI waveguides. Distinct alignment marks are placed adjacent to SiN couplers for the alignment of ULI waveguides. 25
2.18 Alignment marks of cross shapes with widths of (a) 2 μm and (b) 10 μm, and corresponding inverted shapes with spacing of (c) 2 μm and (d) 10 μmin. (e-h) The corresponding captured reflected beam patterns when the laser beam is scanned along the central axis of each alignment mark in the horizontal direction. 26
2.19 Fabrication results of ULI waveguides connected to SiN couplers on the same chip for intra-chip coupling. 27
2.20 Schematic of multi-core fiber integration using ultrafast laser inscription technology. 28
2.21 (a-b) The upgraded optical setup with second harmonic generator and (c-d) the corresponding layouts on the optical bench and the wall, respectively. 29

2.22 (a) Microscopic image of the cross-section of a ULI waveguide inscribed by 515 nm laser beam on Eagle glass. Measured mode profiles at 1550 nm for the ULI waveguides fabricated by (b) 9, 13, and 17 scans. Measured propagation loss and coupling loss of ULI waveguides as a function of the pulse energy at (c-d) different multi-scan times with the fixed scan speed of 10 mm/s and (e-f) different scan speeds with the fixed multi-scan times of 13. 31
2.23 (a) Measured waveguide propagation loss and (b) coupling loss of the ULI waveguides on a glass containing germanium oxide doping as a function of the scan speed at the multi-scan times at 5, 9, and 13, achieving a record low loss of 0.16 dB/cm at a scan speed of 2 mm/s and scan times of 13. . 33
2.24 (a) The input pattern and (b) the output pattern for the proposed fan-in/fan-out device. (c) The schematic diagram for the waveguide design utilizing a routing algorithm. The 2D projections of the waveguide design on (d) X-Z plane, (e) Y-Z plane and (f) X-Y plane, where light propagation direction is along the Z-axis. 35
2.25 (a) Minimum separation distance between adjacent waveguides along the propagation direction. (b) Bending radius for each waveguide along the propagation direction. 35
2.26 (a) Photo of the fabricated 3D fan-in/fan-out device for MCF integration. (b) Microscopic image of the interior where waveguides fan-out to a linear array. (c) Microscopic images of the interior where waveguides fan-in to a circular pattern. (d) Facet image of the input showing the linear array of 8 waveguides. (e) Facet image of the output showing the circular pattern of 8 waveguides. Scale bar = 100 μm. 36
2.27 (a) Operating principle and (b) schematic of an arrayed waveguide grating (AWG). 37
2.28 Schematic of three-dimensional arrayed waveguide grating fabricated by ultrafast laser inscription (ULI) technique. 38

2.29 (a) Microscopic images of the cross-section of ULI waveguides fabricated using single, 5, 9, 13, and 17 scans. (b) Measured waveguide width as a function of the multi-scan times. 39

2.30 (a) Microscopic image for the cross-section of the ULI waveguide utilized as the single-mode waveguide in the proposed AWG design. (b) The measured mode profile at 1550 nm. (c) A schematic of the single-mode ULI waveguide with estimated core dimensions. (d) The simulated mode profile at 1550 nm.(e) The calculation of the effective index for the slab waveguide. (f) Optical properties of the single-mode ULI waveguide. 40

2.31 (a) Design parameters for the AWGR and (b) calculated spectra for all the output waveguides. 41

2.32 (a) The layout of the AWGR, with a footprint measuring 54 mm by 7.91 mm. The detailed view of the star coupler shows the widened star coupler and the inclusion of dummy tapers. (b) Multi-scan routes for each part of the AWGR. 42

2.33 (a) The fabrication result of the complete AWGR. (b) Microscope images for each part of the AWGR. 42

2.34 (a) Alignment of the AWGR and the input fiber by the use of a red laser. (b) Experimental setup. (c) Measured spectra for all the output waveguides. 43

3.1 Schematic of an $N \times N$ phased array of emitters with mode size w_x and w_y, array pitch d_x and d_y, and total size $D_{xTotal} \times D_{yTotal}$. The output beam profile is determined by the product of single element radiation pattern ψ_{rad} and array factor AF. 46

3.2 Simulated angular intensity distribution in the far-field for the phased array with $N = 128$, $w_x = w_y = 1$ μm, and (a) $d_x = d_y = 4.5$ μm and (b) $d_x = d_y = 2.2$ μm as the phase difference $\Delta\phi$ between emitters is tuned to 0π, 0.5π, and 0.9π at the wavelength of 4.6 μm. 46

3.3 Schematic of an OPA device for 2D coherent optical beam steering 47

3.4 (a) Calculated sidelobe-free steering range as a function of the waveguide pitch. (b) Simulated far-field distribution of a 24-element array with waveguide pitches of 1.3 μm and 2.0 μm. 48
3.5 (a) Cross-sections of two silicon waveguides with a width of 500 nm in SiO_2 cladding. (b) Simulated coupling length as a function of waveguide pitch with silicon thicknesses of 220 nm, 300 nm, and 500 nm. 48
3.6 (a) Schematic of a MMI splitter. (b) Top view and (c) perspective view of the simulated MMI splitter. (d) Simulated intensity profile of the MMI splitter with $L_{MMI} = 16$ μm. (e) SEM picture of the fabricated single stage MMI splitter. (f) Simulated and measured excess loss of the MMI splitter as a function of MMI length. 50
3.7 (a) Schematic of the FDTD simulation setup for the grating with DBR. Calculated upward transmission as a function of the top (b) and bottom (c) oxide cladding thickness. Simulated grating emission profile (d) with and (e) without bottom DBRs. 51
3.8 (a) Schematic, top-view, and cross-sectional-view SEM images of the fabricated SiN-assisted weakly emitting grating. (b) Measured near-field infrared (IR) image of the grating along its length. (c) Measured radiator loss of the grating as a function of its length. 52
3.9 (a) Optical microscope image of the fabricated proof-of-concept 2D integrated silicon photonic unit cell. Zoomed-in views of (b) the MMI tree-based splitters, (c) the heater-based phase shifters, and (d) the grating emitter array with 2 μm waveguide pitch. 53
3.10 (a) GDS layout of a 24-element OPA and (b) the corresponding microscope image of the fabricated device. Measured near field images of the grating emitter array with the waveguide pitch of (c-h) 4 μm, (i-n) 2 μm, and (o-t) 1.5 μm. 54

3.11 (a-b) The schematic and picture of the far-field measurement setup employed to characterize our OPA devices. Measured far field images of a single grating emitter under the operating wavelength of (c) 1545 nm and (d) 1550 nm. 55
3.12 (a) Wire bonding of a 24-channal OPA device. (b) Experimental setup for OPA far-field measurement. Measured far-field IR images (c) before phase error correction (PEC) and (d) after phase error correction. 56
3.13 (a) Measured far-field image at different wavelength. (b) Measured far-field image at different phase gradient. 57
3.14 Layout of a vertical emitter and simulated emitted mode profiles for different values of H. 59
3.15 Layouts of a vertical emitter ($H = 2$ μm, $L = 2$ μm) and calculated emitting efficiency as a function of the gap between the coupler and the substrate when the bottom is a Si substrate (left) vs. a SiO_2 substrate with a SiN film (right). 60
3.16 (a) Calculated coupling efficiency as a function of coupler length for a simulated vertical emitter. (b) Layout of the power feeding network where the optical power in the bus waveguide is uniformly coupled into N vertical emitters through evanescent waves. 61
3.17 (a) Side view of a row of simulated vertical emitters with $N = 32$. Calculated normalized field intensity distribution on the top of simulated vertical emitters with (b) no change on coupler length, (c) $\Delta L = 100$ nm and (d) $\Delta L = 50$ nm. 61
3.18 Side view and top view of simulated field intensity distribution for the whole power-feeding network system. 62
3.19 (a) Schematic of SiN_x grating with custom duty cycle on the top of germanium waveguide. (b) Simulated near field for the emission from SiN_x grating. 63

3.20 (a) Microscope image of the fully packaged 12-channel OPA device. (b) Measured near-field pattern for the emission from the SiN_x grating. . . . 64
3.21 Schematic of far-field measurement setup used to characterize the OPA device. 64
3.22 (a-c) Measured far-field patterns for $\lambda = 4550$ nm, 4575 nm, and 4600 nm, respectively. (d) Measured normalized far-field intensity profile along the θ-axis for different wavelengths. 65
3.23 Measured far-field patterns (a) before and (b) after phase-error correction, respectively. (c) Three-dimensional plots for the measured far-field patterns while phase and input wavelength are tuned simultaneously. . . 66
3.24 (a) The cross section and (b) the schematic of the proposed Ge etched grating with custom duty cycle and width. (c) The contour map of the δ values, where $\delta = \beta - \beta_0$, $\beta_0 = 5.16 \times 10^6$/m, and β is the propagation constant for the etched Ge grating with varying duty cycle and width; (d) the simulated combinations of duty cycle and width for the custom grating design. (e) The simulation of emission efficiency for the 100 μm long custom grating for top emission (black) and bottom scattering (red); (f) the simulation of intensity distribution launching from $x = 0$ μm for top emission. 67
3.25 (a) Schematic of a regular grating structure. To improve the upward emission efficiency, the grating structure can be integrated with (b) a 300 nm thick Si_3N_4 layer, (c) a metal layer, or (d) a DBR underneath the grating structure. (e)-(h) Corresponding simulated grating emission profile in log scale. 68
3.26 45 degree reflectors etched by focused-ion-beam etching on Ge on Si waveguides. 69

3.27 (a) Side view, (b) top view, and (c) perspective view of the proposed single layer waveguide array. (d) Layout of 16 emitters in the simulation and the corresponding (e) side view and (f) top view of the simulated field intensity distribution for the whole power-feeding network system. 70
3.28 (a) Variation of calculated effective index with waveguide width when waveguide height is 3.5 μm. (b) Simulated TM mode profile at $\lambda = 8.25$ μm. 71
3.29 (a) MMI design parameter table for 3×3.5 μm^2 ridge waveguide platform at 8.25 μm wavelength. (b) Schematic of an MMI structure. Beam propagation simulation of MMI 3 dB power splitting for (c) $W_{MMI} = 16$ μm and (d) $W_{MMI} = 19$ μm. 72
3.30 (a) Schematic of a staircase-shaped germanium grating emitter. (b) Side view of the simulated power distribution for a 100 μm long grating emitter with the total etching depth of (b) 400 nm, (c) 300 nm, (d) 200 nm, and (e) 100 nm. 73
3.31 (a) Cross-sections of two germanium waveguides on a silicon substrate with CaF_2 cladding. (b) The corresponding calculated crosstalk ratio with varying pitch 73
3.32 Simulated far field patterns for (a) single grating emitter and (b) 24 channels grating emitter with pitch = 5.4 μm at the wavelength 8.25 μm . . . 74
3.33 (a) Schematic for a 128×128 phased arrays based on a Ge-on-SOI platform. (b) Schematic for the bus-to-row coupling. (c) Schematic for the row-to-unit coupling. (d) 3D schematic of the optical phase array including transistors, CONTROL, DATA, and Vdd lines. 76

3.34 (a) Schematic for the proposed guiding structure at 3.8 μm wavelength based on a Ge-on-SOI platform. (b) Calculated propagation loss for the fundamental TM mode when the waveguide width is varied from 0.3 μm to 0.8 μm. (c) Simulated TM mode profile for the waveguide width of 0.6 μm. (d) Calculated bending loss for the bending radius varied from 2 μm to 5 μm. 77

3.35 The coupling length (Black) and the simulated coupler efficiency (Blue) for (a) the bus-to-row couplers and (b) the row-to-unit couplers in the 128×128 phased array for 3.8 μm wavelength. 78

3.36 (a) Schematic for the proposed guiding structure at 4.6 μm wavelength based on a Ge-on-SOI platform. (b) Calculated propagation loss for the fundamental TM mode when the waveguide width is varied from 0.5 μm to 1.2 μm. (c) Simulated TM mode profile for the waveguide width of 0.8 μm. (d) Calculated bending loss for the bending radius varied from 3 μm to 6 μm. 79

3.37 The coupling length (Black) and the simulated coupler efficiency (Blue) for (a) the bus-to-row couplers and (b) the row-to-unit couplers in the 128×128 phased array for 4.6 μm wavelength. 80

3.38 Schematic diagram of 128×128 PEPA array based on AIM PDK (a) without transistors and (b) with transistors. 80

3.39 (a) Schematic diagram for PEPA arrays with different configurations. The corresponding GDS layout, and microscope image are shown in (b) and (c), respectively. Microscope images of the fully packaged 64×64 PEPA array with transistors are shown in (d-f) on different views. 82

3.40 Pictures for the items used in the optical testing bench. 83

3.41 Different approaches for coupling light into a Ge waveguide using a single mode fiber and a high NA objective lens. 84

3.42 Microscope images and measured near fields for (a)-(b) a row of four emitters and (c)-(d) a 4×4 emitter array. 84

4.1 Spectral optical flow in coded aperture snapshot spectral imagers (CASSI). 86

4.2 (a) Schematic of single dispersive CASSI. (b) Meta-CASSI. 87

4.3 Schematic diagram of the metastructure (a-b) and metalens (c-d) with properly placed and sized dimensions to achieve (e-g) the desired phase shift of 0-2π while keeping the throughput nearly 100% for the four spectral bands. The pillar widths that sit in transmission dips (highlighted by gray stripes) are excluded from the design database. 88

4.4 The rectangular metastructure design allows polarization diversifying as well as spectrally dispersive imaging as illustrated for (a) S-polarization and b) P-polarization at two different wavelengths. Calculated field intensity at the focal point for different wavelengths. Wavelength increases in steps from left to right for the four center wavelengths (c) 760 nm, (d) 1611 nm, (e) 2060 nm, and (f) 2320 nm. 90

4.5 Metalens layout for the center wavelength of 2323.1 nm and the design parameters for the F/5 metalenses at the four spectral bands 0.76 μm, 1.61 μm, 2.06 μm, and 2.32 μm. 91

4.6 Measurement setups for (a) beam profile and (b) transmission. 91

4.7 (a) Top-view microscope image for the fabricated on-axis metalens with a diameter of 2 mm. (b-i) Measured beam patterns at various positions away from the metalens. 92

4.8 (a) Simulated light propagation on the x-z plane and (b) the simulated beam profile in the focal plane along x-axis. (c) Measured beam profiles in the focal plane of the metelens along (d) x-axis and (e) y-axis with Gaussian distribution fitting. 93

4.9 (a) Top-view microscope image for the fabricated off-axis metalens. Calculated and measured field intensity at the focal point for two polarizations are shown in (b) and (c) respectively. 94

4.10 (a) Calculated and (b) measured beam profiles at the focal plane for S-polarization as the wavelength scans from 1935 nm to 1937 nm. 95

List of Tables

2.1 Measured optical loss of fabricated ULI straight waveguides on deposited 40 μm thick oxide sample under various inscription conditions. 13

2.2 Measured optical loss of fabricated ULI bending waveguides along the horizontal direction on an Eagle glass sample under various bending conditions. 16

2.3 Measured optical loss of fabricated ULI bending waveguides along the horizontal direction on an Eagle glass sample under various bending conditions. 18

2.4 Measured optical loss of fabricated ULI bending waveguides along the vertical direction on an Eagle glass sample under various bending conditions. 19

2.5 Measured optical loss of fabricated ULI straight waveguides at various depths within the 40 μm thick deposited oxide. 20

2.6 Measured optical loss of fabricated vertical S-shaped waveguides at various depths within the 40 μm thick deposited oxide. 22

2.7 Measured optical loss of ULI straight waveguides on Eagle glass inscribed by a 515 nm laser beam under different inscription conditions. 32

2.8 Measured optical loss of ULI straight waveguides on a glass containing germanium oxide doping inscribed by a 515 nm laser beam under different inscription conditions. 34

4.1 Metalens design parameters for the four spectral bands. 89

Abstract

Functional Photonic Integrated Circuits Based on Advanced Three-Dimensional Photonic Packaging

Three-dimensional (3D) photonic packaging is a pivotal technology for integrating photonics components into compact and efficient optical systems. This dissertation presents advanced techniques for achieving cutting-edge 3D packaging, such as ultrafast laser inscription (ULI), optical phased arrays (OPAs), and metalenses. In ULI, we successfully demonstrated arbitrary vertical ULI waveguides within Eagle glass and an optical interposer, achieving a 0.62 dB/cm propagation loss. Further advancements led to a record-low loss of 0.16 dB/cm using germanium-oxide doped glass. We also employed a waveguide routing tool to demonstrate a 3D fan-in/fan-out device for multi-core fiber integration with SMF-28 fiber arrays. Furthermore, we presented a first 3D arrayed waveguide grating router (AWGR) operating at 1550 nm, created through ULI. Leveraging a multi-scan technique, we achieved a 399.1 GHz channel spacing, and a 2.02 nm 3 dB-passband. The integration of the AWGR with a fan-in/fan-out structure shows its versatility in 3D photonic integration. In optical beam steering, we developed a near-infrared (NIR) OPA with a 5 mm emitting area and 1.3 μm waveguide pitch, exhibiting 3.3° axial and over 40° lateral steering. Additionally, a mid-wave infrared (MWIR) OPA based on a germanium-silicon photonic platform achieved remarkable results, including 0.18° axial and 12.7° lateral beam steering. Furthermore, a commercial foundry was employed to fabricate 64×64 OPAs with integrated transistors, operating at wavelengths of 3.8 μm and 4.6 μm. For metalenses, we developed polarization-diversifying highly-dispersive metalenses tailored for four spectral bands (0.76 μm, 1.61 μm, 2.06 μm, and 2.32 μm) to enable compressive hyperspectral imaging. These metalenses with a 20 mm diameter boast impressive spectral resolving powers (10000, 5000, 4000, and 3571, respectively). Initial tests on a 2 mm metalens designed for a 2.06 μm wavelength validated its focusing capabilities, achieving a 46 % transmission efficiency. Additionally, the off-axis metalens displayed clear polarization splitting and a 12 μm focal spot shift during a 2 nm wavelength tuning.

Acknowledgments

I would like to express my sincere gratitude to Prof. S. J. Ben Yoo for his guidance, expertise, and continuous encouragement. His mentorship has been invaluable. I am also grateful to my dissertation committee members Prof. J. Sebastian Gomez-Diaz and Prof. Marina Radulaski for reviewing my dissertation and serving on my Ph.D. committee.

I would like to express my sincere appreciation to my former labmates Dr. Chuan Qin, Dr. Jason Grenier, Dr. Guangyao Liu, Dr. Hongbo Lu, and Dr. Xian Xiao for their generous sharing of knowledge and expertise.

Numerous students and postdoctoral scholars have played pivotal roles in the progression of my research. I want to acknowledge the invaluable contributions of specific individuals to my dissertation work: In Section 2.2, Yichi Zhang helped the fabrication of optical interposers used for integration with ULI waveguides. In Section 2.3, Sumitomo Electric provided germanium-oxide doped glasses for evaluating ULI performance, and Shuyun Yuan assisted with the characterization of ULI devices. In Section 2.4, Jingwei Wan contributed to the multi-scan routing tool and initial AWGR designs. Shun-Hung Lee made significant contributions to the upgraded 3D AWGR designs, fabrication and characterization. In Section 3.2, Dr. Yu Zhang led the work, with significant contributions to the fabrication process. Kaiqi Zhang helped the device packaging and programming algorithm for phase error correction. In Section 3.3, Dr. Mathias Prost led the work, with substantial contributions to the fabrication process. Rijuta Ravichandran helped the FIB etching for 45-degree reflectors and Kaiqi Zhang contributed to device packaging. In Section 3.4, Hang Su helped the transistor designs and PEPA device layouts. Mehmet Berkay On contributed to device packaging. In Chapter 4, the fabrication of metalenses was done by Rijuta Ravichandran.

Finally, I want to express my deep appreciation to my dear Nicha, for her unwavering support, understanding, and for sharing memorable moments throughout this journey. I also extend my gratitude to my housemate, Evan, for providing support from the beginning of my Ph.D. career in the United States. To my beloved family members, your love and encouragement have been the bedrock of my motivation and accomplishments.

Chapter 1

Background and Motivation

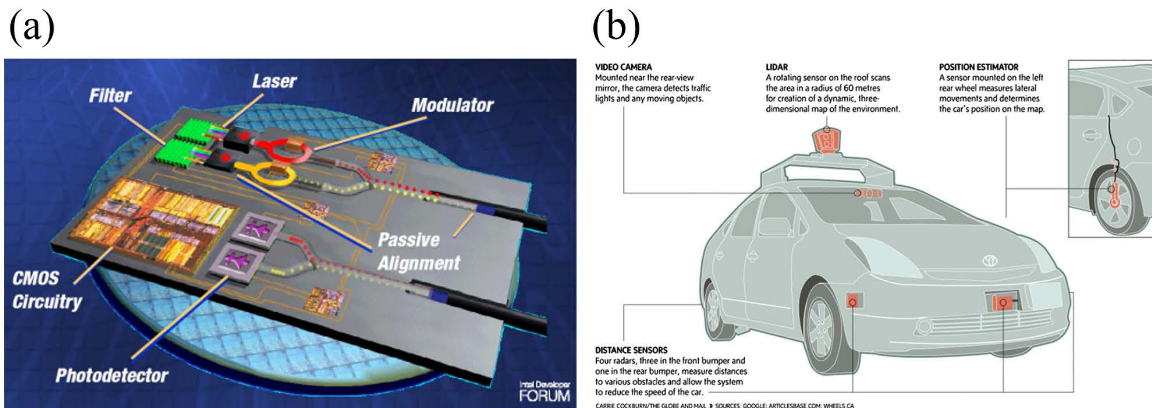

Figure 1.1. Schematic of (a) inter-chip interconnects on a silicon photonic integrated circuit [1] and (b) light detection and ranging (LIDAR) system [2].

Over the past decade, the field of photonic integration has experienced remarkable advancements. These developments have led to the emergence of chip-scale systems and optoelectronic interposers that hold the promise of revolutionizing various applications including Tb/s inter-chip interconnects and low-cost light detection and ranging (LIDAR) systems, as illustrated in Figure 1.1. In contrast to the conventional electronics domain, which primarily relies on metal-based flip-chip bonding or wire bonding for chip-to-chip interconnections, the field of photonics necessitates a more versatile three-dimensional (3D) packaging technology capable of delivering substantially improved alignment accuracy. This precision is essential for establishing low-loss connections between photonic chips, ensuring the efficient transmission of optical signals and the overall success of pho-

tonic integrated systems. In this study, we will show a variety of promising techniques for achieving state-of-the-art 3D packaging including ultrafast laser inscription, optical phased arrays, and metalenses.

1.1 Photonic packaging using ultrafast laser inscription

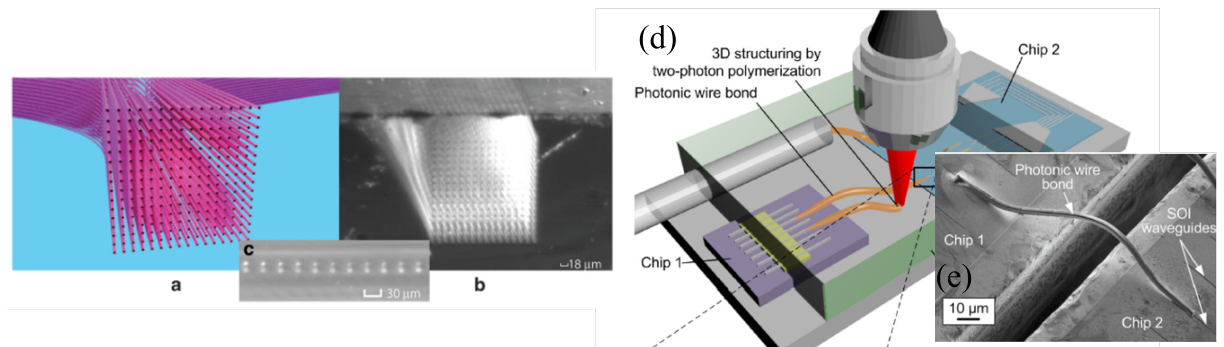

Figure 1.2. Demonstration of (a) a 2D-3D fan-in fan-out chip [3] and (b) a photonic wire-bonding technique [4] using ultrafast laser inscription.

Ultrafast Laser Inscription (ULI) has emerged as a pivotal technology in the realm of 3D photonic device fabrication, playing a vital role in enabling advanced 3D photonic packaging [3, 4] as illustrated in Figure 1.2. At its core, ULI hinges on the delivery of exceptionally short laser pulses to a target material, typically a transparent substrate or crystal. These ultrafast laser pulses possess an extraordinary concentration of energy, affording the capability for meticulous material ablation, modification, and inscription. Researchers have harnessed this remarkable technology to craft intricate microstructures, waveguides, photonic circuits, and even complex 3D optical components. In recent years, ULI has found a multitude of applications, underscoring its versatility and impact on various fronts. Notable among these applications are Photonic Integrated Circuits (PICs) [3], 3D micro and nanostructuring [7–10], and the writing of Fiber Bragg Gratings (FBGs) [11–14]. PICs, in particular, have garnered substantial attention for their potential to integrate diverse microsystems, thereby creating new functionalities. For instance, Lindenmann's research group introduced the innovative concept of photonic wire bonding, showing its feasibility through the demonstration of low-loss interconnects among photonic

chips arranged in 3D configurations [4]. Furthermore, ULI technology enables the fabrication of low-loss 2D-3D fan-in and fan-out devices, facilitating photonic packaging between distinct components, such as silicon waveguides and multicore fibers [15, 16]. Another remarkable development is the work of Yoo's group, which introduced photonic–electronic integration using ULI waveguides to achieve orbital-angular-momentum (OAM) multiplexing/demultiplexing and beam steering [3]. These breakthroughs exemplify the ongoing evolution of ULI technology and its profound impact on photonics applications.

1.2 Beam steering using optical phased arrays

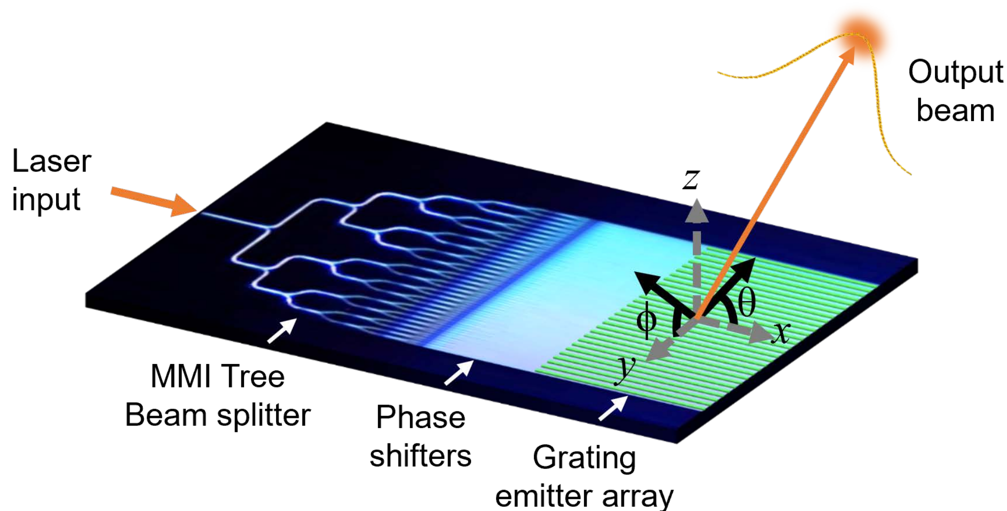

Figure 1.3. Schematic of an OPA photonic integrated circuit (PIC) based on grating emitters for two-dimensional beam steering.

Optical beam steering has been widely used in many applications, including free-space optical communications (FSOC) [17], imaging [18], and light-detection-and-ranging (LiDAR) [19]. However, most traditional beam-steering technologies rely on the optomechanical movement of mirrors and lenses, which limits the beam-steering capability. Therefore, solid-state optical beam steering based on optical phased arrays (OPAs), as shown in Figure 1.3, with no moving parts enables faster, more compact, and lower-cost devices [20–26]. OPAs consist of an array of closely spaced optical emitters or waveguides, often using semiconductor technology. By controlling the phase of light emitted from each element, they can create interference patterns that steer the direction of the resulting light

beam. Mature CMOS-compatible fabrication processes permit subwavelength element spacing while effectively managing optical loss, resulting in beam steering without sidelobes and achieving high emission efficiency. Furthermore, recent advancements in silicon photonics foundries have enabled the cost-effective production of large-scale integrated OPAs. These developments open up exciting possibilities for enhanced optical systems and applications, further advancing the field of optical beam steering.

1.3 Compact integrated imaging system using metalenses

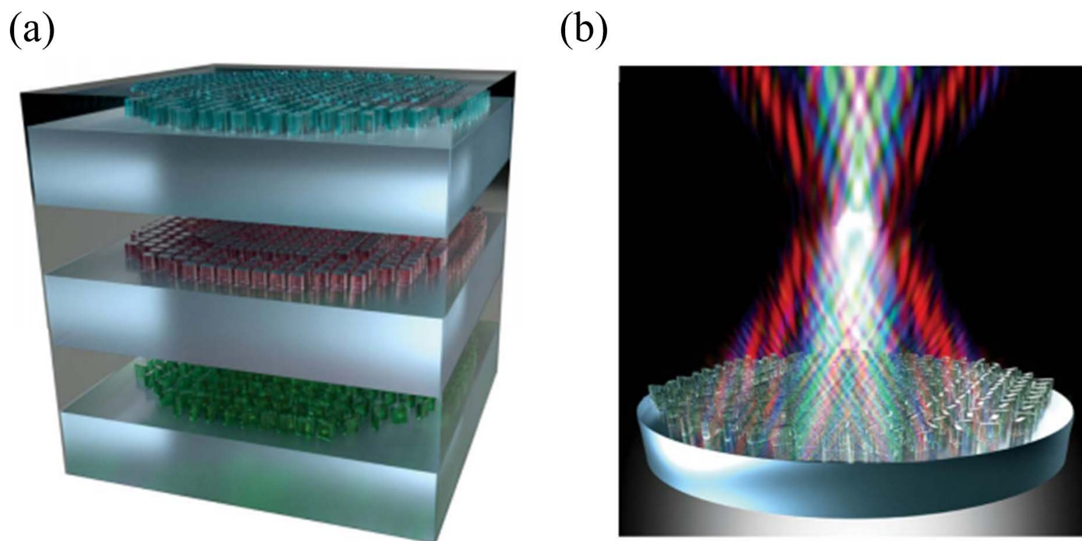

Figure 1.4. (a) Illustration of the concept of vertically stacking metalenses to build an ultrathin multifunctional optical system [5]. (b) Schematic of an achromatic metalens [6].

Among the various flat optical devices, metalenses stand out for their exceptional potential in creating ultrathin, vertically integrated systems with multifunctional focusing, as depicted in Figure 1.4(a) [5]. Metalenses offer precise control over both the phase and amplitude of light, allowing for the customization of wavefronts by adjusting the structural parameters of each constituent element within the metalens. Compared to conventional optical lens systems, metalenses exhibit several advantages, including a higher numerical aperture, absence of spherical aberration, and diffraction-limited focus-

ing [27, 28]. Furthermore, all-dielectric metalenses have been demonstrated to significantly reduce absorption losses. Figure 1.4(b) illustrates another noteworthy achievement on broadband achromatic metalenses, achieved through the meticulous design and precise arrangement of individual elements [6]. What makes metalenses even more promising is their straightforward fabrication process and versatile design, making them fully compatible with CMOS technology [29, 30]. This compatibility opens up possibilities for integration into a wide range of optical systems, including those with applications in imaging, sensing, and telecommunications.

1.4 Dissertation outline

This dissertation delves into various 3D packaging technologies applied to photonic integration systems. In Chapter 2, we leverage ultrafast laser inscription to achieve intra-chip coupling within an optical interposer, integration with multi-core fibers, and the implementation of 3D arrayed waveguide grating routers (AWGRs). Moving on to Chapter 3, we are dedicated to the exploration of non-mechanical, electronically controlled optical beam steering and formation, employing optical phased arrays (OPAs) in the near-infrared and mid-infrared spectral regions. Additionally, we work on the design and thorough characterization of OPAs fabricated by a silicon photonics foundry. Chapter 4 shows the integration of metalenses into a compressive sensing architecture, highlighting their pivotal role in achieving hyperspectral imaging. We have meticulously designed, fabricated, and characterized large-scale metalenses with millimeter dimensions, rigorously evaluating their spectral resolution capabilities. Finally, Chapter 5 provides a comprehensive summary of the dissertation's work and offers a glimpse into future research prospects.

Chapter 2

Three-Dimensional Photonic Integrated Devices Fabricated by Ultrafast Laser Inscription

2.1 Principle

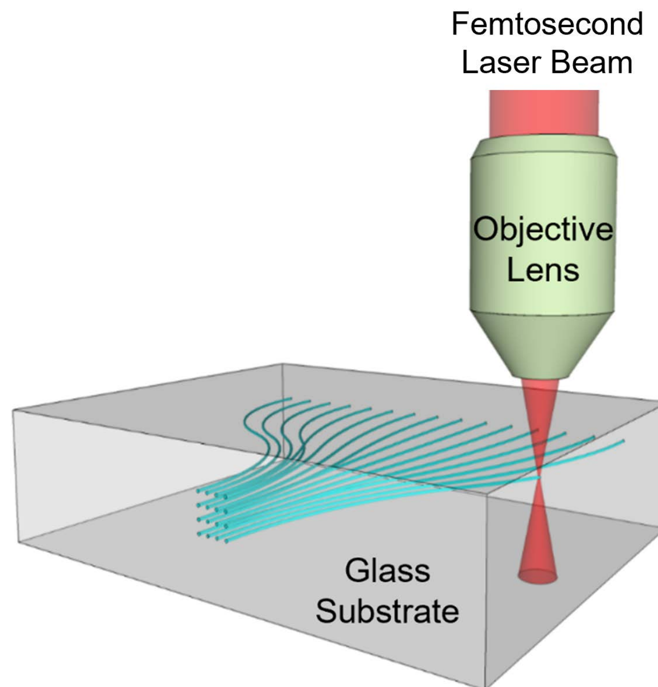

Figure 2.1. Schematic diagram of 3D waveguide writing by ultrafast laser inscription.

Ultrafast laser inscription (ULI) utilizes multi-photon ionization to induce nonlin-

ear absorption, resulting in the creation of permanent structural changes. Among these changes, three common types can be broadly classified: smooth refractive index change, birefringent refractive index modification, and microexplosion (empty voids) [31]. These types of changes are determined by exposure conditions and material properties. Figure 2.1 illustrates the schematic diagram of three-dimensional waveguide writing in a glass substrate by ultrafast laser inscription. In terms of exposure conditions, several factors are taken into consideration, including pulse repetition rate, average power, pulse energy, pulse duration, laser wavelength, laser polarization, scan speed, and cross-section engineering (multi-scan). By increasing the pulse repetition rate or average power, it is possible to achieve higher scan speeds, thereby reducing the total fabrication time. In this work, circularly polarized light is employed for laser inscription to ensure the consistent uniformity of waveguide properties across various shapes. Additionally, a multi-scan technique [32] is utilized to optimize waveguide propagation loss and tailor the optical mode profile for minimizing coupling loss. As depicted in Figure 2.2, each scan along the waveguide is laterally displaced to form a rectangular waveguide core.

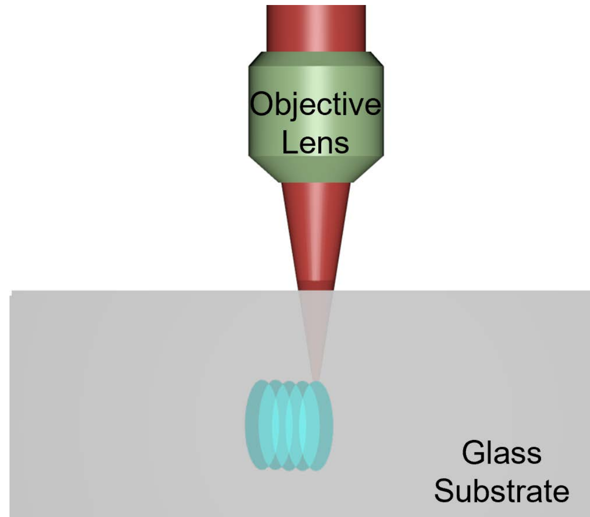

Figure 2.2. Schematic diagram of the multi-scan technique

ULI techniques are often demonstrated in the materials of glasses and crystals. Certain studies have employed doped glasses to enhance the refractive index change within the waveguide core [33, 34]. In this work, We mainly fabricated the ULI waveguides on

the boro-aluminosilicate glass (Eagle2000), which features lightweight composition, low thermal expansion, and transparent appearance.

2.2 Arbitrary vertical low-loss waveguides in deposited oxide of optical interposers for low-loss 3D photonic packaging

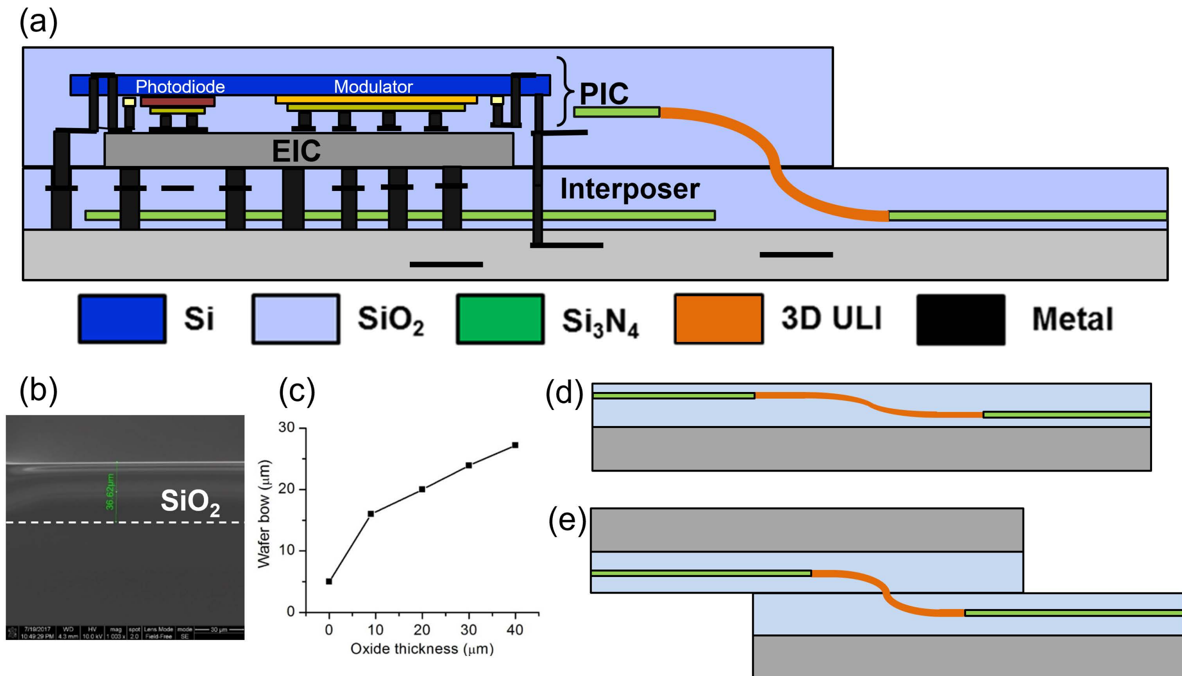

Figure 2.3. (a) Schematics of packaged photonic and electronic convergence system with 3D ULI waveguides for optical coupling. (b) Cross-sectional SEM pictures of deposited oxide cladding on a silicon substrate. (c) Measured wafer bow as a function of deposited oxide thickness. Schematic of (d) intra-chip and (e) chip-to-chip light coupling using 3D ULI waveguides.

Ultrafast laser inscription (ULI) has become an emerging technology for 3D photonic device fabrication, facilitating 3D photonic packaging [3]. Low-loss 2D-3D fan out chips [15] and photonic wire-bonding [4] have been demonstrated using this technique. However, demonstrated waveguide devices are typically on glass or polymer platforms [4, 15], which generally are not compatible with the mature CMOS fabrication. This prohibits its further application in the photonics/photonics-electronics convergence systems. In this section,

we proposed a new chip-to-chip optical coupling scheme using an arbitrary vertical S-bend low-loss waveguide fabricated on deposited oxide cladding for 3D photonic packaging.

Figure 2.3(a) shows our proposed scheme using 3D ULI waveguides on deposited oxide cladding for low-loss optical coupling between different photonic chips/photonic integrated chip and an optical interposer. As the ULI waveguide can be fabricated from 10 μm to > 100 μm in the vertical directions, it offers flexible integration with the high-speed electronic driving circuits, eliminating long wires with large parasitic capacitance. To achieve this integration, we fabricated a proof-of-concept ULI device on deposited oxide cladding on a six inch silicon wafer using standard low-pressure chemical vapor deposition. Figure 2.3(b) shows the crosssectional SEM picture of deposited 40 μm thick oxide samples. We expected the flatness of the sample over a typical chip size (1 cm) is less than 2 μm from measured wafer bow data (Figure 2.3(c)). In the following study, we will begin by characterizing the ULI waveguides in deposited oxide on silicon substrate. Subsequently, we aim to achieve intra-chip light coupling between 3D ULI waveguides and SiN waveguides, as illustrated in Figure 2.3(d). Once we successfully demonstrate low-loss intra-chip coupling, our next step will involve realizing chip-to-chip light coupling between two photonic chips using 3D ULI waveguides, as depicted in Figure 2.3(e).

2.2.1 System setup for ultrafast laser inscription

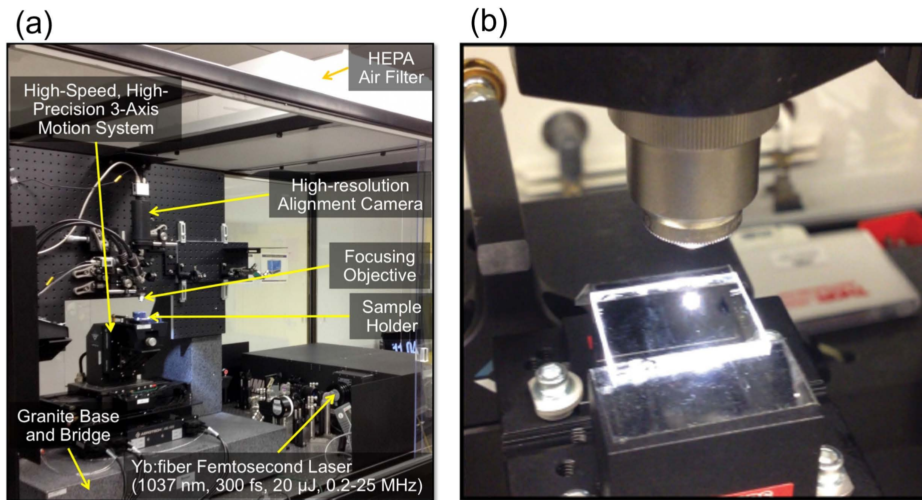

Figure 2.4. (a) Ultrafast laser inscription system. (b) Laser inscription on a glass substrate using a high NA objective lens.

Figure 2.4 (a) illustrates the setup of our ultrafast laser inscription (ULI) system. The Yb-doped fiber laser system (Clark-MXR) can generate pulse energies of up to 10 μJ, with a user-selectable repetition rate ranging from 200 kHz to 25 MHz. The output beam has a center wavelength of approximately 1038 nm, and a pulse width of about 300 fs. An aspheric objective lens with a numerical aperture (NA) of 0.55 is used to focus the laser beam onto the sample, which is positioned on a computer-controlled 3-axis stage (Aerotech), as shown in Figure 2.4 (b). The stage is capable of reaching a maximum moving speed of 2 m/s, with a remarkable repeatability down to 200 nm. A high-resolution camera equipped with lens tubes was installed on the top of the sample to precisely align the writing patterns and monitor the laser inscription in the sample. In addition, a HEPA air filter was installed on top of the ULI system to ensure a well-maintained and conducive operating environment.

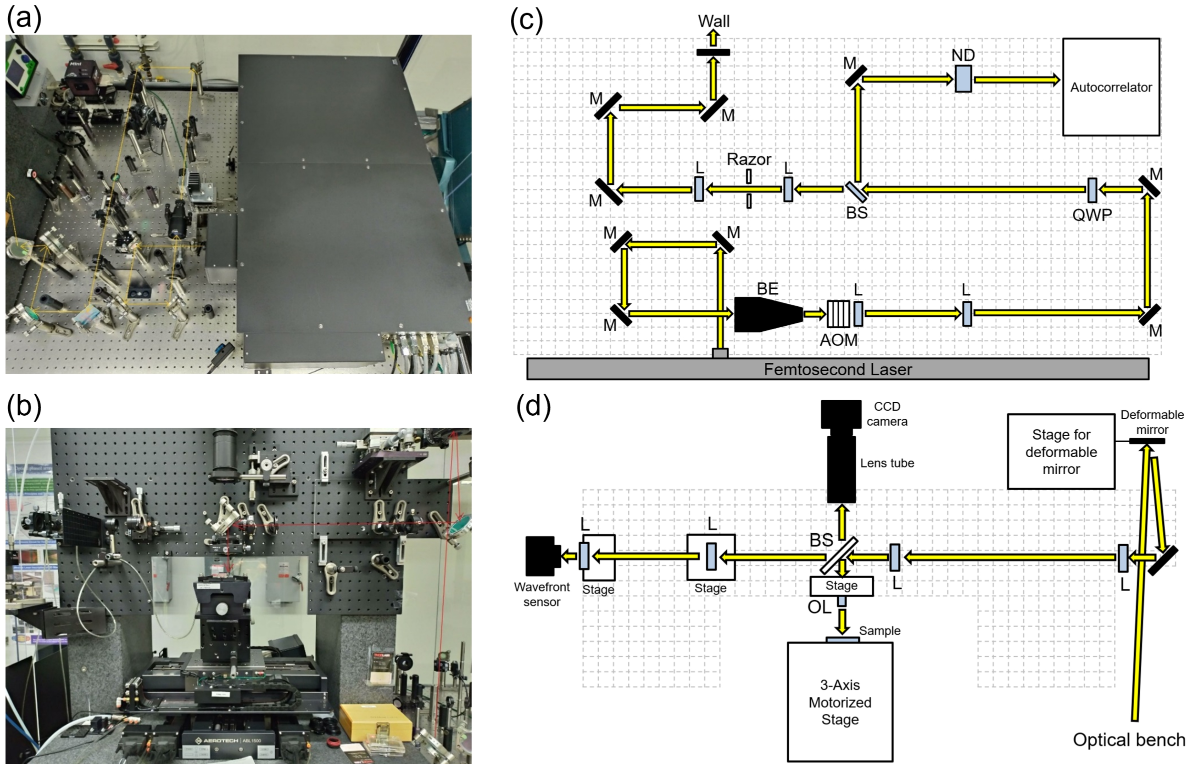

Figure 2.5. (a-b) The optical setup and (c-d) the corresponding layouts on the optical bench and the wall, respectively.

Figure 2.5 (a) and (b) show the entire optical setup within the ULI system, and the

corresponding layouts on the optical bench and the wall are illustrated in Figure 2.5 (c) and (d) respcetively. To enable rapid modulation of the optical power for laser inscription, an acousto-optic modulator (AOM) is employed in this system. Additionally, a quarter wave plate is utilized to generate circularly polarized light, as mentioned in the previous paragraph, in order to inscribe waveguides with arbitrary shapes. An autocorrelator is used to monitor the laser pulse width to ensure it stays around 300 fs during the laser inscription process. When inscribing depths are greater than 500 μm below the surface, a deformable mirror and wavefront sensor are employed to tailor the wavefront of the laser beam and correct any optical aberrations. At the end of this system, the laser beam is focused onto the sample using an objective lens with a high NA of 0.55, while the laser inscription process is closely monitored with a high-resolution CCD camera.

2.2.2 Characterization of ULI straight waveguides on deposited oxide of optical interposers

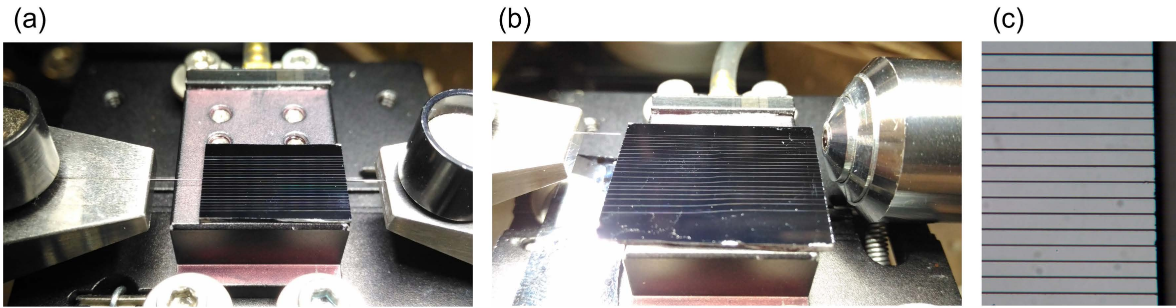

Figure 2.6. Measurement setups for (a) optical loss and (b) optical mode profiles. (c) Top view of fabricated ULI waveguides under different exposure conditions.

Figure 2.6 (a-b) illustrates the measurement setups employed for characterizing ULI waveguides on deposited 40 μm thick oxide samples. In Figure 2.6 (a), two SMF-28 fibers were used for butt-coupling with the ULI waveguides to characterize their optical losses. The mode profiles of each ULI waveguide were captured using an objective lens with 60x magnification and 0.85 NA as shown in Figure 2.6 (b). To optimize the transmission efficiency of the ULI waveguides, we use a multi-scan technique with a 200 nm lateral shift between each scan. Figure 2.6 (c) shows the top view of the fabricated ULI waveguides under various exposure conditions.

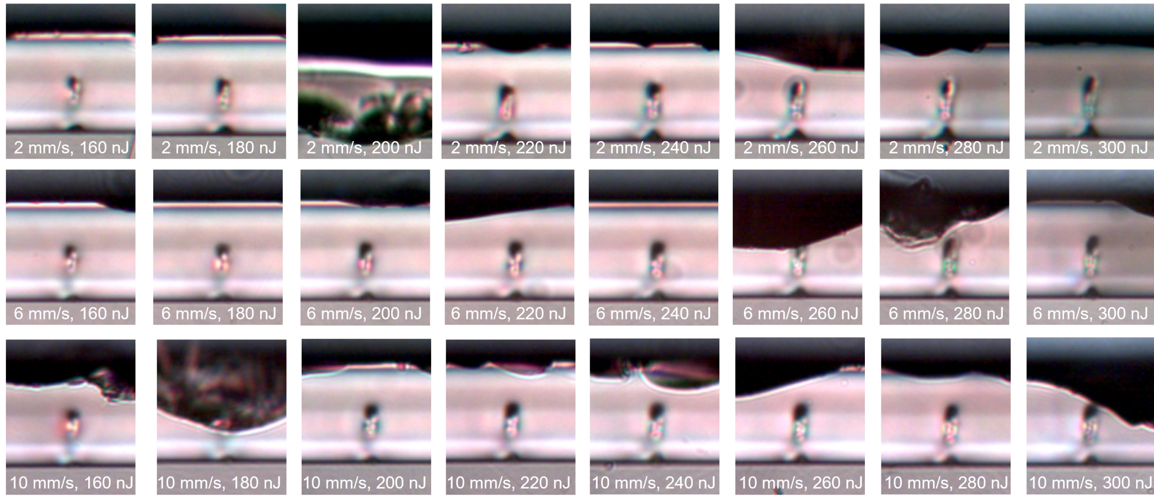

Figure 2.7. The cross-sections of fabricated ULI waveguides on deposited 40 μm thick oxide samples under various inscription conditions.

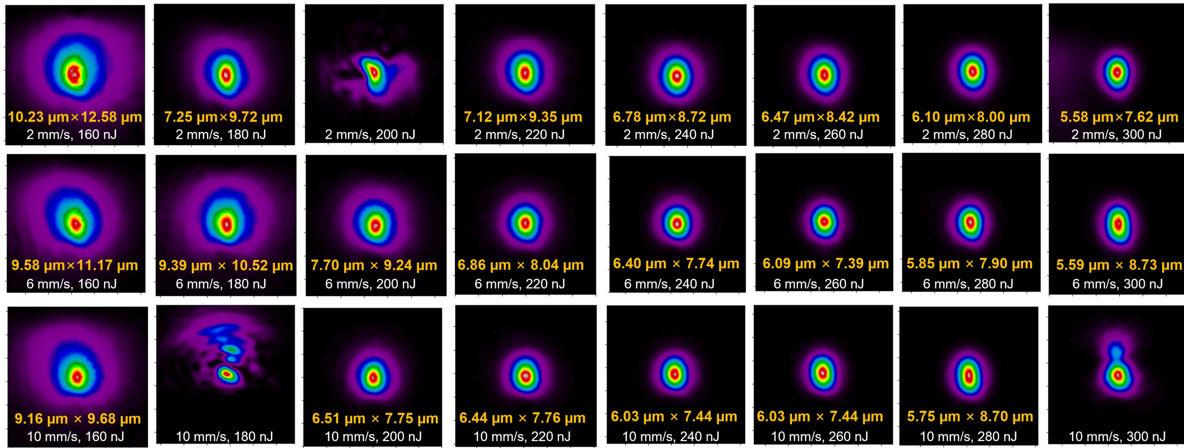

Figure 2.8. Measured mode profiles of fabricated ULI waveguides on deposited 40 μm thick oxide samples under various inscription conditions.

Figure 2.7 displays the cross-section pictures of fabricated ULI waveguides on deposited oxide samples with a thickness of 40 μm. The applied pulse energy ranged from 160 to 300 nJ, while the writing speed varied at 2, 6, and 10 mm/s. The chosen writing depth was 20 μm below the top surface to effectively eliminate the unwanted scattered light induced at the boundaries of the air and the substrate. As the initial testing, these waveguides were fabricated by 11 scans, following the previous optimized inscribing recipe for Eagle glasses. Besides, to prevent optical crosstalk between adjacent waveguides, the waveguide spacing was set to 200 μm. It is worth noting that certain waveguide facets suffered cracking as a

result of an unoptimized polishing process. Figure 2.8 shows the measured mode profiles of fabricated ULI waveguides at 1550 nm wavelength. As the pulse energy increases, the mode field diameter decreases, indicating a higher refractive index change and improved optical confinement. For instance, at a writing speed of 6 mm/s and a pulse energy of 160 nJ, the mode field diameter measures 9.58 μm by 11.17 μm. However, as the pulse energy is raised to 300 nJ, the mode field diameter decreases to 5.59 μm by 8.73 μm. It is noteworthy that the fabricated waveguide dimensions and measured mode profiles on the deposited oxide cladding are comparable to those on the glass substrate.

Table 2.1. Measured optical loss of fabricated ULI straight waveguides on deposited 40 μm thick oxide sample under various inscription conditions.

Inscription condition	Total insertion loss (dB)	Coupling loss (dB/facet)	Propagation loss (dB/cm)
160 nJ, 2 mm/s	10.6	0.07	4.38
160 nJ, 6 mm/s	8.3	0.03	3.46
160 nJ, 10 mm/s	8.1	0.05	3.35
180 nJ, 2 mm/s	6.5	0.3	2.47
180 nJ, 6 mm/s	7.4	0.03	3.08
180 nJ, 10 mm/s	11.5		
200 nJ, 2 mm/s	37.7		
200 nJ, 6 mm/s	4.3	0.24	1.6
200 nJ, 10 mm/s	4.4	0.68	1.28
220 nJ, 2 mm/s	5	0.35	1.8
220 nJ, 6 mm/s	3.9	0.54	1.19
220 nJ, 10 mm/s	4.4	0.7	1.26
240 nJ, 2 mm/s	3.9	0.48	1.23
240 nJ, 6 mm/s	3.8	0.71	1
240 nJ, 10 mm/s	4.2	0.89	1.02
260 nJ, 2 mm/s	3.5	0.6	0.97
260 nJ, 6 mm/s	3.5	0.88	0.73
260 nJ, 10 mm/s	4.3	0.86	1.08
280 nJ, 2 mm/s	2.9	0.77	0.57
280 nJ, 6 mm/s	10	0.88	3.46
280 nJ, 10 mm/s	4.8	0.82	1.32
300 nJ, 2 mm/s	23	1.04	8.77
300 nJ, 6 mm/s	9.9	0.88	3.41
300 nJ, 10 mm/s	16.6	0.83	6.26

Following the investigation of mode profiles, our focus shifts to the characterization of

optical loss, as shown in Table 2.1. The sample measures approximately 2.4 cm in length. The coupling loss is determined through the optical mode mismatch between an SMF-28 fiber and a ULI waveguide. The coupling efficiency can be computed using the overlap integral of the two electric fields, as presented below:

$$\eta = \frac{\left|\iint E_1 E_2 dxdy\right|^2}{\iint |E_1|^2 \, dxdy \iint |E_2|^2 \, dxdy} \tag{2.1}$$

where E_1 and E_2 represent the respective electric fields of an SMF-28 fiber and a ULI waveguide in this context. Given that the spatial field distributions for both SMF-28 fibers and ULI waveguides can be approximated as Gaussian distributions, Equation 2.1 can be further simplified into the following equation for the coupling loss:

$$\text{CL (dB)} = 10 \log_{10} \frac{4d_{fiber}^2 d_x d_y}{\left(d_x^2 + d_{fiber}^2\right)\left(d_y^2 + d_{fiber}^2\right)} \tag{2.2}$$

where d_{fiber} is the mode field diameter for a SMF-28 fiber and d_x and d_y are the mode field diameters for a ULI waveguide along horizontal and longitudinal directions respectively. The mode field diameter for SMF-28 fibers is 10.5 μm at 1550 nm wavelength. The propagation loss can then be determined by subtracting the coupling loss from the total insertion loss.

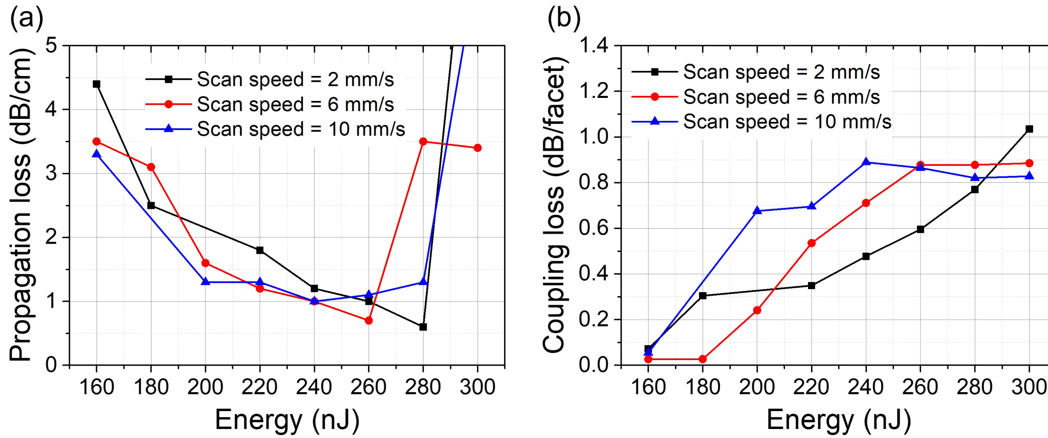

Figure 2.9. (a) Measured propagation loss and (b) coupling loss of ULI waveguides on deposited 40 μm thick oxide sample as a function of the pulse energy at different scan speeds. These waveguides were fabricated by 11 scans.

Figure 2.9 presents the propagation loss and coupling loss at different scan speeds and pulse energies. The results indicate that the coupling loss escalates as pulse energy

increases due to the growing mode mismatch between the SMF-28 fiber and the ULI waveguide. Conversely, the propagation loss initially diminishes as pulse energy rises and reaches a minimum within the range of 240-280 nJ. The optimal propagation loss of 0.57 dB/cm is achieved at a pulse energy of 280 nJ and a scan speed of 2 mm/s while the coupling loss with a SMF-28 is 0.77 dB. It is noted that despite the coupling loss can be reduced to below 0.4 dB/facet when the pulse energy is lower than 200 nJ, the corresponding propagation loss would exceed 2 dB/cm, which is unsuitable for making low-loss optical devices.

2.2.3 Characterization of ULI bending waveguides on deposited oxide of optical interposers

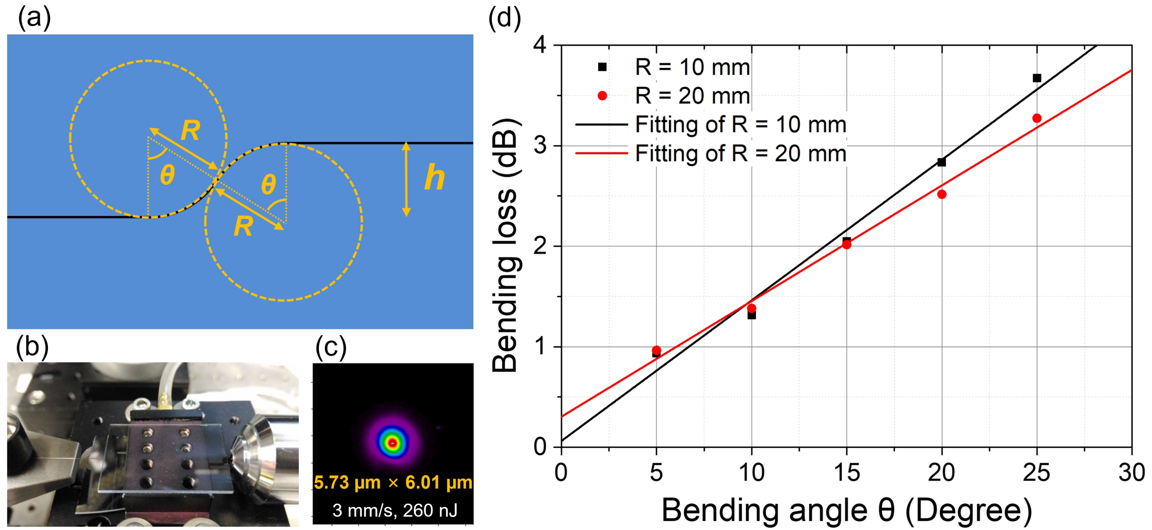

Figure 2.10. (a) Configuration of S-shaped waveguide. (b) Measurement setup. (c) Measured mode profile of a fabricated ULI waveguide on a Eagle glass sample using a scan speed of 3 mm/s and a pulse energy of 260 nJ. (d) Measured bending loss as a function of the bending angle for the bending radii of 10 mm and 20 mm.

With the completion of the characterization of straight ULI waveguides, we move on to the exploration of bending ULI waveguides. Recognizing that ULI structures require a bending radius on the order of millimeters to mitigate substantial bending losses caused by the relatively lower refractive index change, we decided to utilize S-shaped structures as depicted in Figure 2.10 (a) to study the bending loss. Figure 2.10 (b) illustates the

measurement setup for characterizing S-shaped ULI structures on a Eagle glass. For this investigation, we utilized a scan speed of 3 mm/s and a pulse energy of 260 nJ as the inscription conditions. The corresponding mode profile of the ULI waveguide is depicted in Figure 2.10 (c). The measured average propagation loss is 0.495 dB/cm. Figure 2.10 (d) presents the measured bending loss for the bending radii of 10 mm and 20 mm with the sample length of 2.95 cm. The bending loss diminishes as the bending angle decreases, reaching a minimum of approximately 1 dB at a bending angle of 5 degrees for both bending radii of 10 mm and 20 mm. The fitted data indicates a bending loss of 0.14 ± 0.01 dB/° for a 10 mm bending radius and 0.115 ± 0.006 dB/° for a 20 mm bending radius. For more comprehensive measurement results, please refer to the detailed information provided in Table 2.2.

Table 2.2. Measured optical loss of fabricated ULI bending waveguides along the horizontal direction on an Eagle glass sample under various bending conditions.

Structure type	Total insertion loss (dB)	Coupling loss (dB/facet)	Propagation loss (dB/cm)	Bending loss (dB)
Straight	4.5	1.44	0.55	
Straight	4.3	1.5	0.44	
S-shaped (10 mm, 5°)	5.1	1.4		0.94
S-shaped (10 mm, 10°)	5.6	1.5		1.31
S-shaped (10 mm, 15°)	6.2	1.47		2.05
S-shaped (10 mm, 20°)	6.9	1.47		2.83
S-shaped (10 mm, 25°)	7.5	1.39		3.67
S-shaped (20 mm, 5°)	5.1	1.42		0.96
S-shaped (20 mm, 10°)	5.5	1.5		1.38
S-shaped (20 mm, 15°)	5.9	1.47		2.02
S-shaped (20 mm, 20°)	6.3	1.5		2.52
S-shaped (20 mm, 25°)	6.8	1.45		3.27

In order to further minimize bending losses, we proceeded to fabricate ULI bending strctures with increased bending radii and reduced angles, as demonstrated in Figue 2.11. Figue 2.11(a) shows the mode profile of a straight waveguide using the same inscription condition as utilized in Figure 2.10. The measured average propagation loss is 0.565 dB/cm and the sample length is 2.95 cm. In Figue 2.11(b), we examined the bending structures incorporating bending radii of 20 mm, 40 mm, and 60 mm along with bending

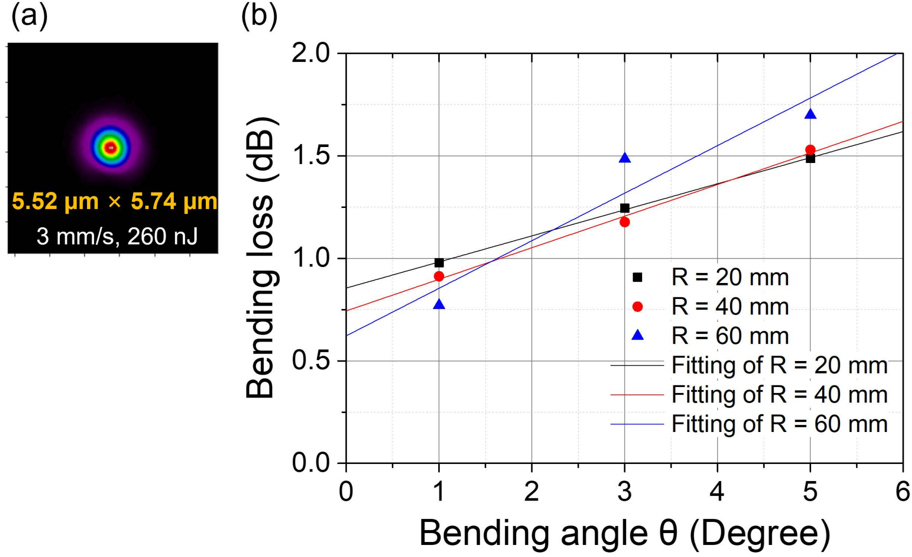

Figure 2.11. (a) Measured mode profile of a fabricated ULI waveguide on a Eagle glass sample using a scan speed of 3 mm/s and a pulse energy of 260 nJ. (b) Measured bending loss as a function of the bending angle for the bending radii of 20 mm, 40 mm, and 60 mm.

angles of 1, 3, and 5 degrees. Similarly, The bending loss diminishes as the bending angle decreases. Besides, the results indicate the bending loss can reach below 1 dB when the bending angle is 1 degree. The fitted data shows a bending loss of 0.127 ± 0.003 dB/° for a 20 mm bending radius, 0.154 ± 0.013 dB/° for a 40 mm bending radius, and 0.232 ± 0.072 dB/° for a 60 mm bending radius. For more comprehensive measurement results, please refer to the detailed information provided in Table 2.3.

The previous investigation exclusively focused on discussing bending structures in a horizontal plane, as illustrated in Figure 2.12(a). In order to create waveguides of arbitrary shapes, we extended our efforts by fabricating S-shaped structures along the vertical plane, as depicted in Figure 2.12(b). We selected a bending radius of 20 mm for this study and the total sample length is 2.9 cm. Figure 2.12(c) and (d) display the microscope image of a ULI waveguide core and the corresponding captured mode profile in Eagle glass respectively. The measured average propagation loss is 0.815 dB/cm. Figure 2.12(e) presents the measured bending loss under various bending angles. The fitted data indicates a bending loss of 0.133 ± 0.024 dB/°, which closely aligns with the results obtained for bending structures along the horizontal plane as shown in Figue 2.11(b). Notably, the bending loss

Table 2.3. Measured optical loss of fabricated ULI bending waveguides along the horizontal direction on an Eagle glass sample under various bending conditions.

Structure type	Total insertion loss (dB)	Coupling loss (dB/facet)	Propagation loss (dB/cm)	Bending loss (dB)
Straight	4.8	1.59	0.55	
Straight	5	1.64	0.58	
S-shaped (20 mm, 1°)	6.1	1.75		0.98
S-shaped (40 mm, 1°)	5.8	1.65		0.91
S-shaped (60 mm, 1°)	5.8	1.74		0.77
S-shaped (20 mm, 3°)	6.1	1.65		1.24
S-shaped (40 mm, 3°)	5.9	1.65		1.18
S-shaped (60 mm, 3°)	5.9	1.55		1.49
S-shaped (20 mm, 5°)	6.2	1.62		1.49
S-shaped (40 mm, 5°)	6.1	1.65		1.53
S-shaped (60 mm, 5°)	6.1	1.66		1.7

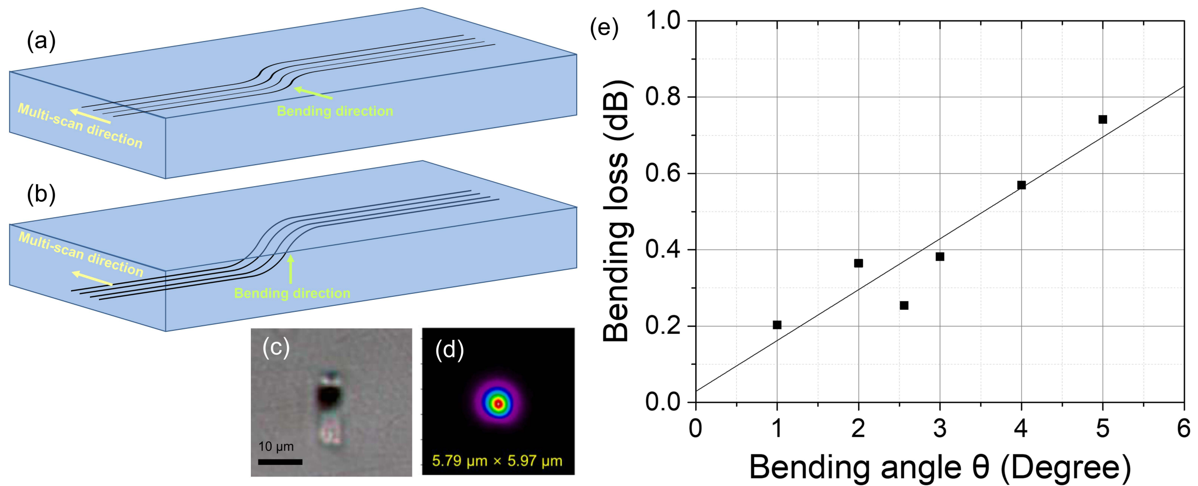

Figure 2.12. The schematic of laser inscription for bending structures along (a) the horizontal and (b) vertical directions, respectively. (c) Captured microscope image and (d) measured mode profile of a fabricated ULI waveguide on a Eagle glass sample using a scan speed of 3 mm/s and a pulse energy of 260 nJ. (e) Measured bending loss as a function of the bending angle for a bending radius of 20 mm.

of vertical bending structures is approximately 0.7 to 0.9 dB lower than that of horizontal bending structures. This disparity can be attributed to the overlap mismatch losses between the optical modes in straight and bending waveguides. For more comprehensive measurement results, please refer to the detailed information provided in Table 2.4.

Table 2.4. Measured optical loss of fabricated ULI bending waveguides along the vertical direction on an Eagle glass sample under various bending conditions.

Structure type	Total insertion loss (dB)	Coupling loss (dB/facet)	Propagation loss (dB/cm)	Bending loss (dB)
Straight	5.1	1.39	0.8	
Straight	5.1	1.35	0.83	
S-shaped (20 mm, 1°)	5.4	1.45		0.2
S-shaped (20 mm, 2°)	5.4	1.4		0.36
S-shaped (20 mm, 2.56°)	5.4	1.47		0.25
S-shaped (20 mm, 3°)	5.4	1.42		0.38
S-shaped (20 mm, 4°)	5.5	1.4		0.57
S-shaped (20 mm, 5°)	5.5	1.34		0.74

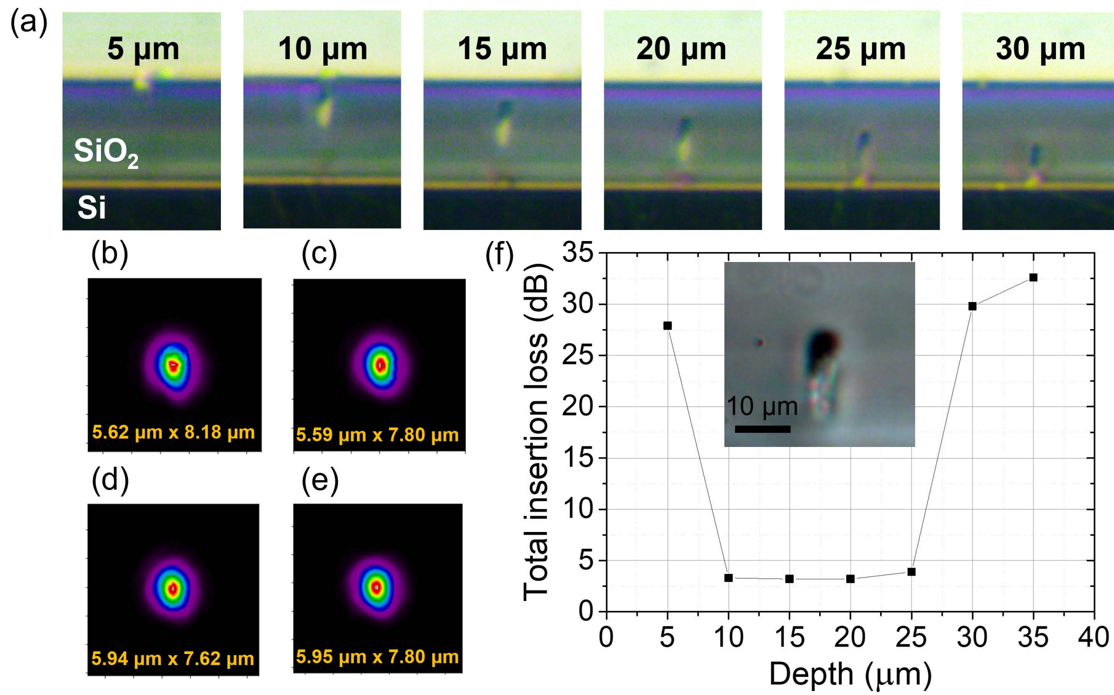

Figure 2.13. (a) Cross-sections of ULI waveguides at various depths within the deposited oxide. The corresponding measured mode profiles of a fabricated ULI waveguide at depths of (b) 10 μm, (c) 15 μm, (d) 20 μm, and (e) 25 μm. (f) Measured total insertion loss as a function of the waveguide depth (inset: captured microscope image of a fabricated ULI waveguide on deposited oxide using a scan speed of 3 mm/s and a pulse energy of 260 nJ).

Following an in-depth exploration of ULI bending structures on Eagle glass, we are now transitioning to fabricating and analyzing these structures on a 40 μm thick deposited oxide sample. It is important to note that the boundaries with the air and the

substrate may influence the inscription of ULI waveguides. Therefore, we will initiate an examination of the propagation efficiency of ULI waveguides at various depths, as depicted in Figure 2.13. Figure 2.13(a) demonstrates cross-sections of ULI waveguides at various depths within the deposited oxide. These images reveal that the ULI waveguide core experiences distortion when inscribed within 5 μm below the top surface or within 10 μm above the substrate. Figure 2.13(b-e) display captured mode profiles for the ULI waveguides at depths ranging from 10 μm to 25 μm, showcasing a remarkable level of consistency. In Figure 2.13(f), the total insertion loss for ULI waveguides at different depths is presented, with a sample length of 1.93 cm. It is noteworthy that the total insertion loss remains below 4 dB when the waveguide depth falls within the range of 10-25 μm. However, it increases significantly beyond 25 dB when the waveguide depth exceeds this range. The inset in Figure 2.13(f) shows a microscope image of a ULI waveguide core that was fabricated on deposited oxide. Table 2.5 provides an in-depth overview of the measurement results. The coupling loss falls within the range of approximately 0.8 to 1 dB per facet, which is slightly lower compared to Eagle glass due to the larger mode field diameter. Regarding the propagation loss, it reaches a minimum of 0.62 dB/cm, slightly higher than that observed for Eagle glass. This discrepancy can be attributed to suboptimal inscription conditions close to the wafer surface.

Table 2.5. Measured optical loss of fabricated ULI straight waveguides at various depths within the 40 μm thick deposited oxide.

Depth (μm)	Total insertion loss (dB)	Coupling loss (dB/facet)	Propagation loss (dB/cm)
5	27.9		
10	3.3	0.93	0.74
15	3.2	1	0.62
20	3.2	0.89	0.74
25	3.9	0.85	1.13
30	29.8		
35	32.6		

After thoroughly characterizing the straight waveguides on deposited oxide, our focus now shifts to the investigation of bending waveguides. In Figure 2.14(a), we provide a schematic depicting the inscription of a vertical S-shaped bending waveguide on deposited

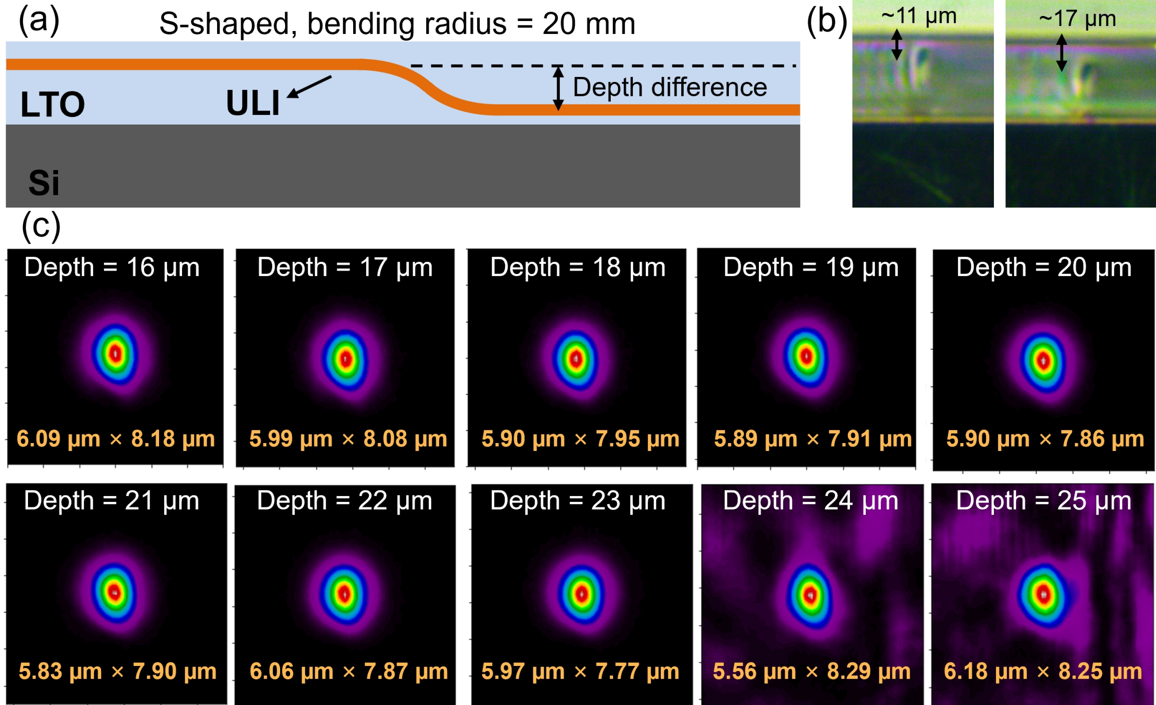

Figure 2.14. (a) Schematic of a vertical S-shaped bending waveguide on deposited oxide.(b) Two ends of a fabricated S-shaped waveguide, spanning a depth range from 11 μm to 17 μm. (c) Measured mode profiles of ULI waveguides within the depth range of 16 μm to 25 μm

oxide. For this investigation, we selected a bending radius of 20 mm, taking into consideration the thickness of the deposited oxide and the desired bending loss. Additionally, in this initial demonstration, we opted for depth differences of 6 μm and 10 μm, corresponding to bending angles of 1 degree and 1.3 degrees, respectively. Figure 2.14(b) shows the two ends of an S-shaped bending waveguide, spanning a depth range from 11 μm to 17 μm. The measured mode profiles of the ULI waveguides within the depth range of 16 μm to 25 μm are presented in Figure 2.14(c) respectively. Notably, the mode profiles from depths of 16 μm to 23 μm exhibit remarkable similarity, while distortion becomes noticeable when the depth exceeds 23 μm.

Table 2.6 displays the measurement results for the vertical S-shaped waveguides within the deposited oxide. The total length of the sample measures 1.93 cm.We observed a significant increase in total insertion loss when the waveguide depth exceeded 22 μm, a trend consistent with the change in mode profiles depicted in Figure 2.14(c). The

Table 2.6. Measured optical loss of fabricated vertical S-shaped waveguides at various depths within the 40 μm thick deposited oxide.

Depth range (μm)	Total insertion loss (dB)	Coupling loss (dB/facet)	Bending loss (dB)
10-16	4.6	0.75	1.8
11-17	5.1	0.8	2.2
12-18	4.9	0.85	1.9
13-19	5	0.86	1.98
14-20	5.3	0.86	2.27
15-21	5.4	0.89	2.33
10-20	5.7	0.71	2.99
11-21	6	0.87	2.97
12-22	7	0.8	4.11
13-23	13.3	0.85	10.31
14-24	29.1		
15-25	33.4		

calculated coupling loss ranges between 0.7-0.9 dB per facet, aligning with the findings presented in Table 2.5. Regarding bending loss, we achieved 1.8 dB for a 6 μm depth difference and 2.97 dB for a 10 μm depth difference. Comparing these results with those of Eagle glass outlined in Table 2.4, we note that the bending loss in the deposited oxide sample is relatively higher, by approximately 1.6 dB when the bending radius is 20 mm and the bending angle is 1 degree. This discrepancy can be attributed to suboptimal inscription conditions employed near the wafer surface. We anticipate that this loss can be reduced to approximately 0.2 dB (Eagle glass values are recorded at a depth of 100 μm below the surface) with improved inscription conditions.

2.2.4 Initial integration of SiN waveguides with 3D ULI waveguides through chip-to-chip coupling

In Figure 2.15(a) and (b), we present a summary of the proposed coupling scheme and the simulated coupling loss between a conventional SiN inverse taper coupler and a ULI waveguide. Before realizing the integration of SiN waveguides with ULI waveguides within the deposited oxide of an optical interposer, we commence with the initial coupling of SiN waveguides and ULI waveguides through chip-to-chip coupling. Figure 2.15(c) illustrates the measurement setup for characterizing the SiN waveguides intended for the initial

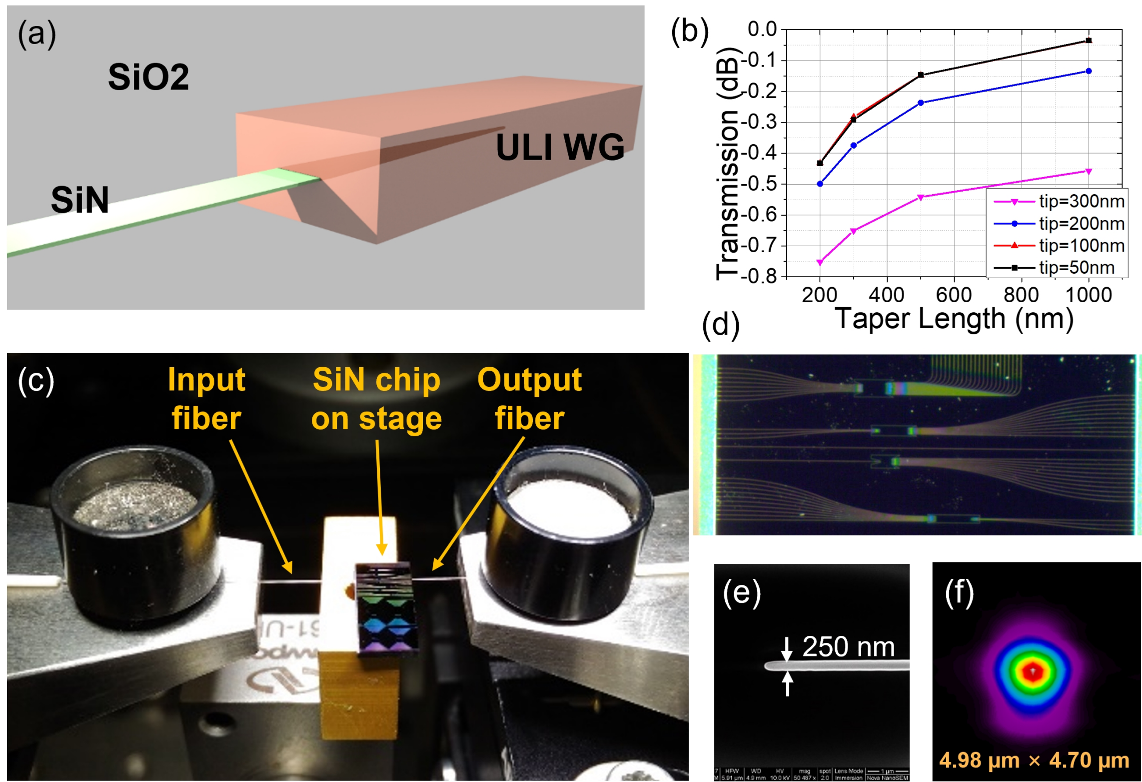

Figure 2.15. (a) Perspective-view schematic of SiN-to-ULI waveguide coupling structure. (b) Simulated coupling loss for various taper length and taper tip width. (c) Experimental setup for the loss measurement of a SiN waveguide. (d) Microscopic image for the top view of the SiN chip. (e) Top-view SEM picture of fabricated SiN taper tip. (f) Mode profile of SiN inverse taper captured by a CCD camera at 1550 nm.

integration. The microscope image of the SiN chip with testing straight waveguides is displayed in Figure 2.15. Figure 2.15(e) shows the SEM image of a fabricated SiN inverse taper using 248 nm projection lithography. Given the taper size and measured mode profile (Figure 2.15(f)), we expect a ∼0.6 dB coupling to fabricate the ULI waveguide.

After characterizing the SiN waveguides, we proceeded to perform initial coupling loss measurements between the SiN coupler and the ULI waveguide on two separate chips, as illustrated in Figure 2.16(a) and (b). The input facet of the SiN coupler and the output facet of the ULI waveguide were coupled to SMF-28 fibers. To aid in the alignment of the two chips and two fibers, we utilized a red laser to observe the light coupling on the chip facet and the subsequent light propagation within the waveguides, as depicted in Figure 2.16(c). We successfully measured a coupling loss of 2.8 dB between the SiN

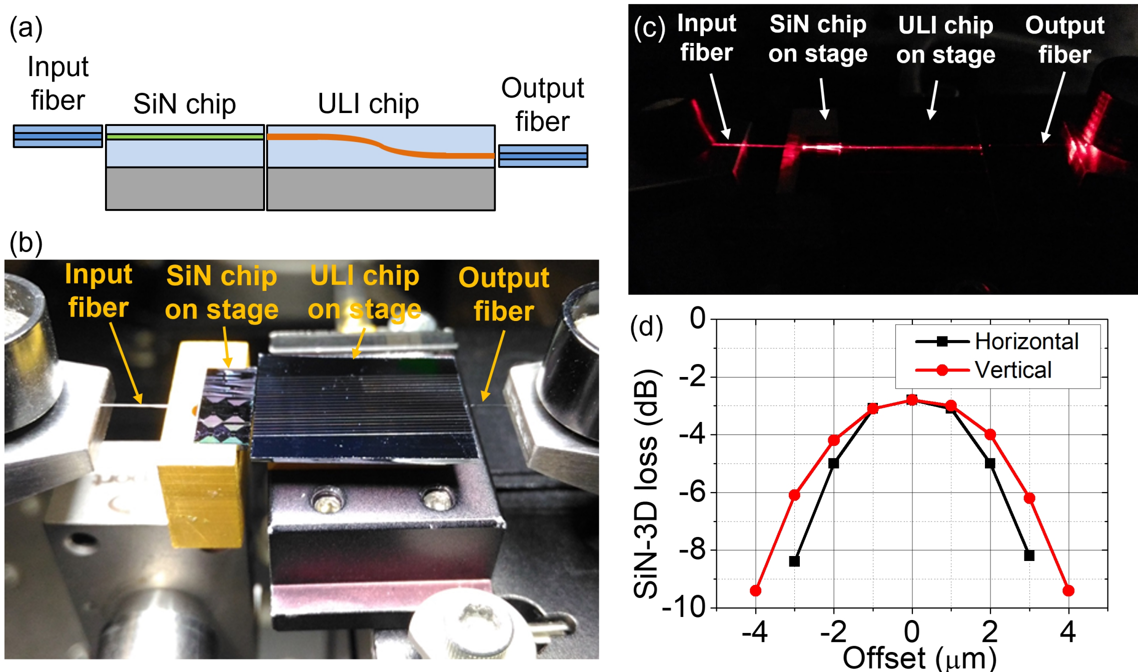

Figure 2.16. (a) Schematic of initial coupling loss measurements between the SiN coupler and the ULI waveguide on two separate chips. (b) Experimental setup for SiN-ULI waveguide butt-coupling. (c) Alignment of the two chips and the two fibers by the use of a red laser. (d) Measured SiN chip to 3D chip coupling loss as a function of offset in horizontal and vertical directions.

coupler and the ULI waveguide and we attributed the ~2.2 dB excess loss to the air gap between the two chips. Figure 2.16(d) provides a concise summary of our measured coupling loss between the SiN coupler and the ULI waveguide, plotted as a function of offset from the lowest loss point. We observe negligible loss increment within 1 μm misalignment and less than 2 dB increment within 2 μm misalignment in both horizontal and vertical directions.

2.2.5 Alignment of SiN waveguides and 3D ULI waveguides on the same chip for ultimate intra-chip coupling

The preceding subsection has demonstrated the successful integration of a SiN coupler with a 3D ULI waveguide using chip-to-chip coupling. Now, our focus shifts towards achieving intra-chip coupling between a SiN coupler and a 3D ULI waveguide. In Figure 2.17 (a), the schematic illustrates the demonstration of intra-chip coupling between SiN couplers and 3D ULI waveguides on a deposited oxide with a 40 μm thickness. The

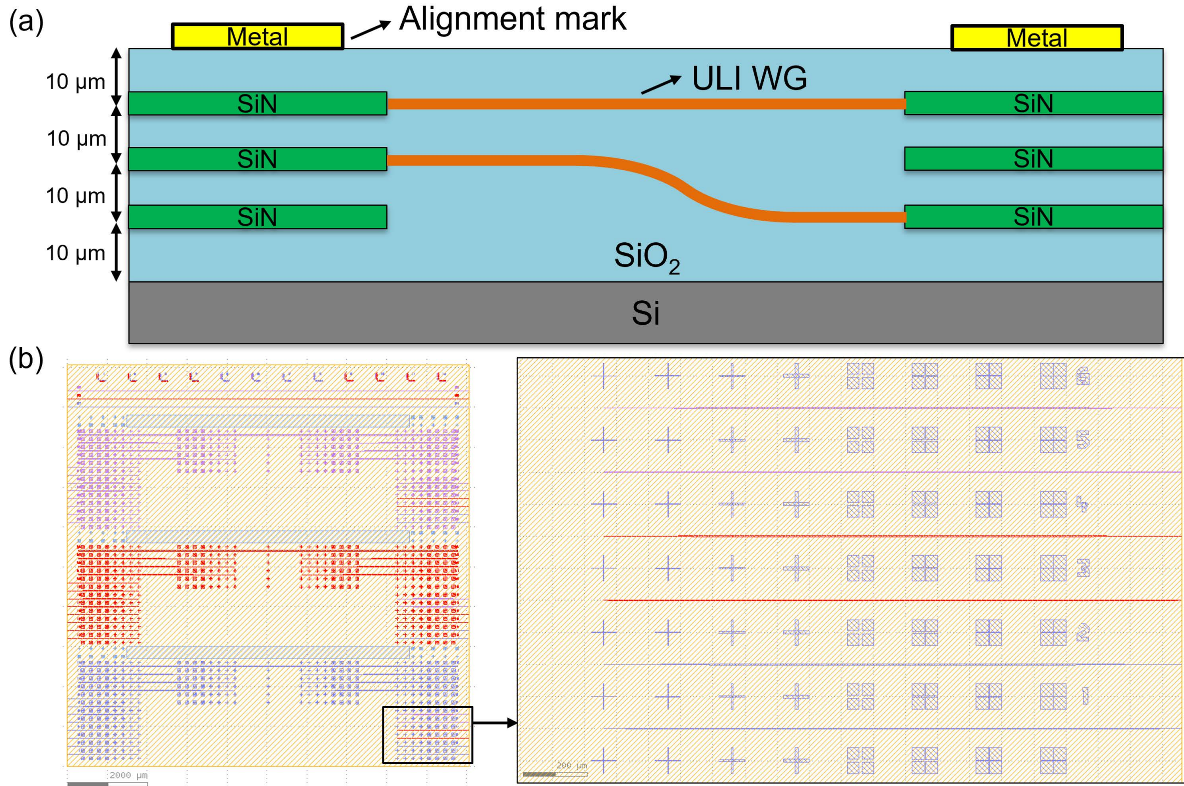

Figure 2.17. (a) Schematic of intra-chip coupling between SiN couplers and 3D ULI waveguides. (b) Layout of SiN couplers at the depth of 10 μm (purple), 20 μm (red), and 30 μm (blue) within the deposited oxide for intra-chip coupling with 3D ULI waveguides. Distinct alignment marks are placed adjacent to SiN couplers for the alignment of ULI waveguides.

SiN couplers are placed at the depths of 10 μm, 20 μm, and 30 μm within the deposited oxide, and the waveguides with arbitrary vertical shapes are inscribed to connect the SiN couplers on both sides at different depths. Figure 2.17 (b) presents an overview of the layout for the SiN couplers designed for intra-chip coupling with 3D ULI waveguides. The SiN couplers, located at depths of 10 μm, 20 μm, and 30 μm within the deposited oxide, are represented by the colors purple, red, and blue in the layout. To ensure precise alignment between ULI waveguides and SiN couplers, we have thoughtfully incorporated distinct alignment marks positioned adjacent to the SiN couplers.

In Figure 2.18, we focused the laser beam on various alignment marks to assess the corresponding alignment performance by observing variations in reflected light intensity. For the alignment marks, we chose crosses measuring 80 μm in length with widths of 2 μm

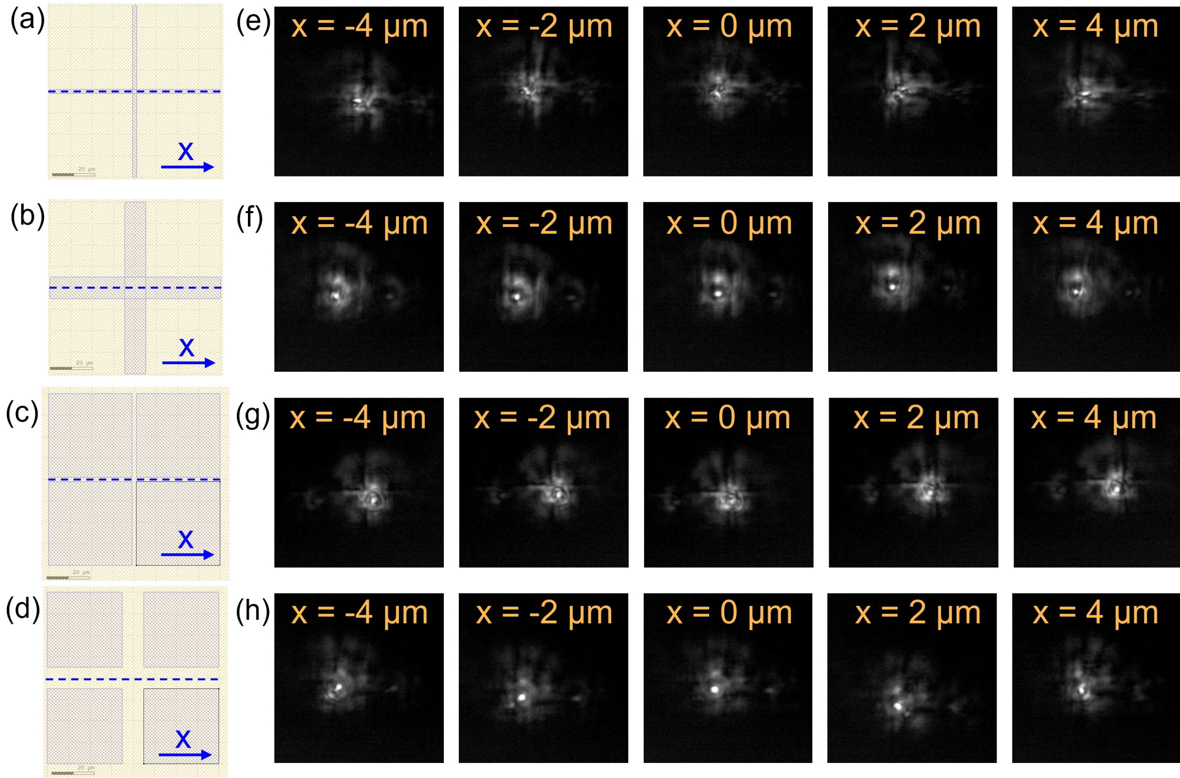

Figure 2.18. Alignment marks of cross shapes with widths of (a) 2 μm and (b) 10 μm, and corresponding inverted shapes with spacing of (c) 2 μm and (d) 10 μmin. (e-h) The corresponding captured reflected beam patterns when the laser beam is scanned along the central axis of each alignment mark in the horizontal direction.

and 10 μm, as well as their corresponding inverted shapes with spacing of 2 μm and 10 μm, as depicted in Figure 2.18 (a)-(d), respectively. In Figure 2.18 (e)-(h), we conducted a laser beam scan along the central axis of each alignment mark in the horizontal direction. We observed variations in the reflected beam intensity, which were captured by the CCD camera installed on top of the sample. The results clearly demonstrate that we achieve the maximum reflected light intensity when the laser beam is in close proximity to the center of the cross-shaped alignment mark, whereas the inverted shape of alignment marks produces the minimum intensity. Taking into account the alignment tolerance required for coupling between SiN couplers and ULI waveguides, it becomes evident that the cross-shaped alignment mark with a width of less than 2 μm is the most suitable option for this purpose.

Following the characterization of the alignment marks, our next step was to inscribe

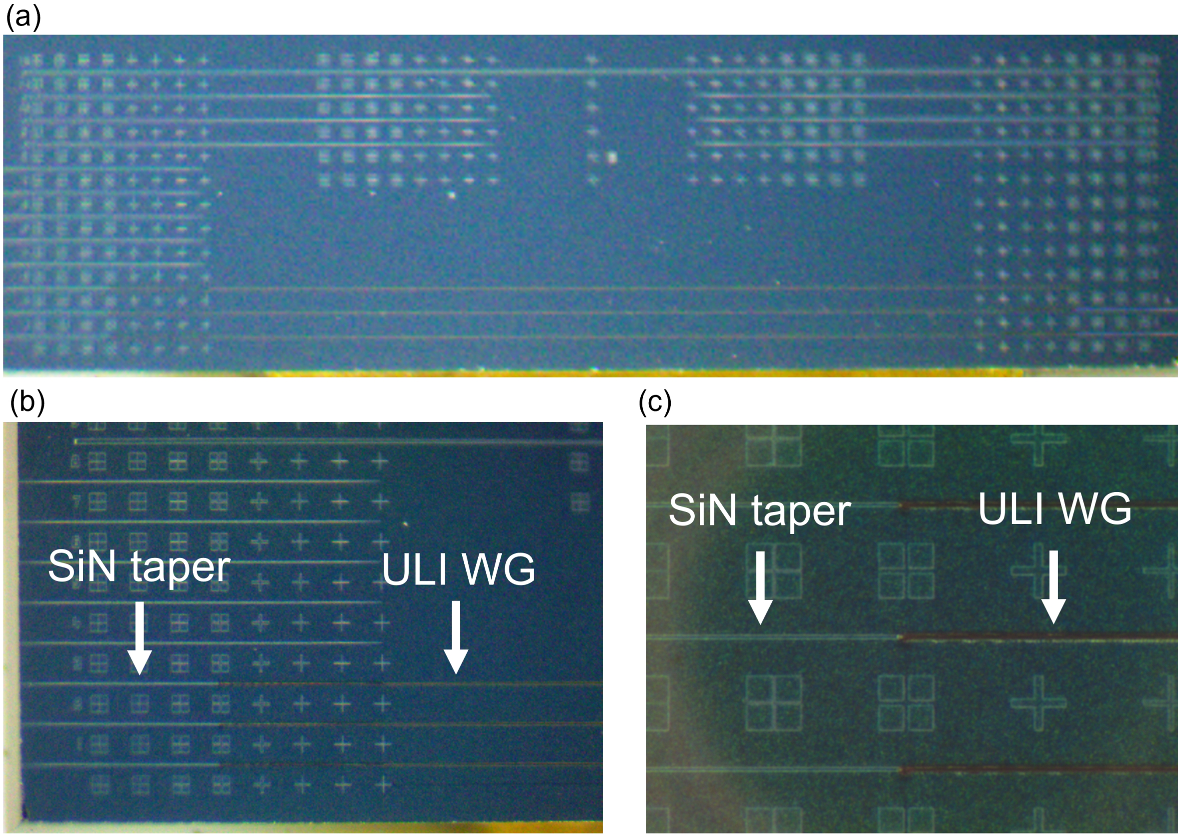

Figure 2.19. Fabrication results of ULI waveguides connected to SiN couplers on the same chip for intra-chip coupling.

ULI waveguides on the same chip along with SiN couplers, ultimately facilitating intra-chip coupling, as illustrated in Figure 2.19. In Figure 2.19(a), we can observe the inscription of ULI waveguides connecting the ends of the SiN couplers on both the left and right sides. To optimize the performance and account for propagation loss based on earlier investigations, the ULI waveguides were inscribed at a depth of 10 μm within the deposited oxide cladding. Figure 2.19(b) and (c) provide a closer view of the region where SiN couplers and ULI waveguides overlap. These results clearly demonstrate the high precision of alignment achieved between the SiN couplers and ULI waveguides, thanks to the assistance of the alignment marks.

2.2.6 Summary

We demonstrated an arbitrary vertical low-loss waveguide fabricated on deposited oxide cladding. Our measurements indicate a low propagation loss of 0.62 dB/cm and a less than

3 dB chip-to-chip coupling loss to a conventional SiN inverse taper on a fabricated sample. Our next objective is to further enhance the efficiency of optical coupling between the SiN couplers and ULI waveguides situated on the same chip through intra-chip coupling. This will provide a flexible and low-loss optical coupling for 3D photonic packaging.

2.3 Low-loss three-dimensional fan-in/fan-out devices for multi-core fiber integration

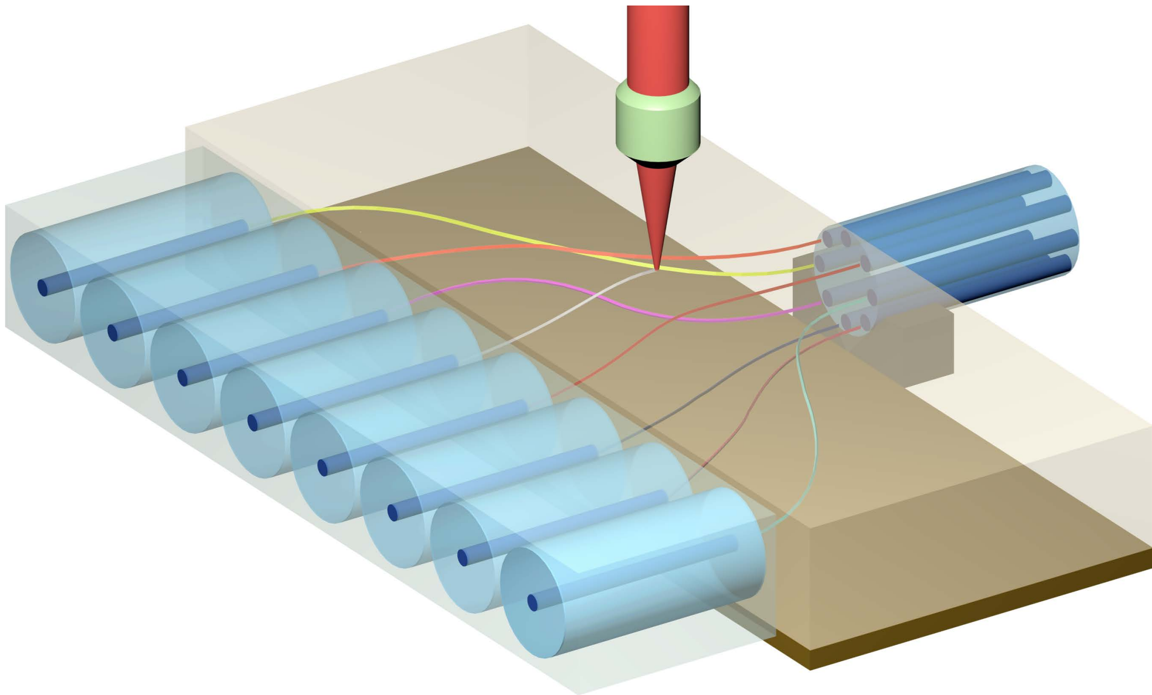

Figure 2.20. Schematic of multi-core fiber integration using ultrafast laser inscription technology.

Multi-core fibers (MCF) offer multi-fold increases in the capacity of optical transmission links by incorporating multiple strands of waveguide cores in the shared cladding [35–38]. Since all current transmission and switching systems use conventional single core fiber (SCF) interfaces, the low-loss coupling between SCFs and MCF becomes a critical issue in future high-capacity optical fiber communications. Due to the dense geometric arrangement of cores in a MCF of a limited diameter, a three-dimensional (3D) packaging method with high alignment accuracy for low-loss interconnections between the optical fibers becomes desirable.

Recently, the ultrafast laser inscription (ULI) technology emerged as a viable 3D photonic packaging method [3, 39, 40] such as low-loss 2D-3D fan-out chips [15]. In this section, we used the ULI technique to fabricate a 3D fan-in/fan-out device that allows a MCF with a circular array of cores to be integrated with a linear array of SCFs as illustrated in Figure 2.20. Further, we investigated multi-scan ULI methods on two types of glass materials to achieve low-loss optical packaging.

2.3.1 ULI system upgrade with a second-harmonic generator

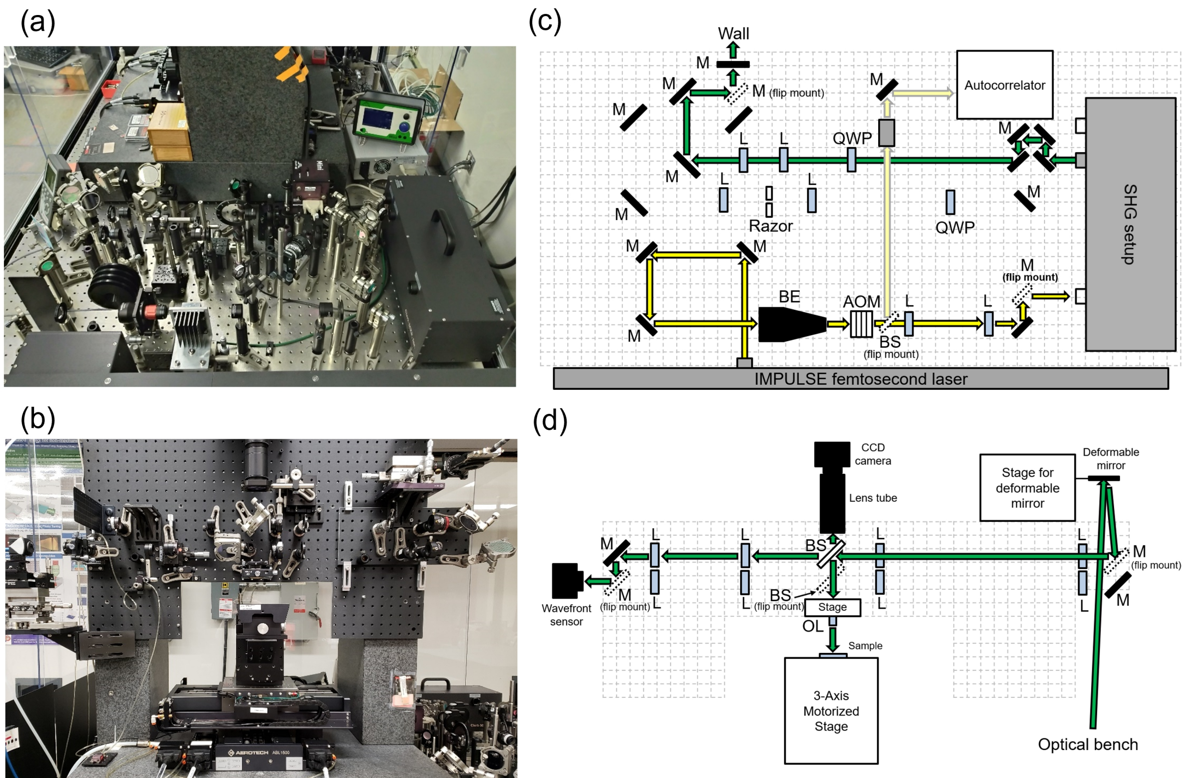

Figure 2.21. (a-b) The upgraded optical setup with second harmonic generator and (c-d) the corresponding layouts on the optical bench and the wall, respectively.

We have already presented the complete optical setup of our ULI system in Figure 2.4 and demonstrated its exceptional performance in the previous section. In order to enhance our ULI system further, we have integrated a second harmonic generator (SHG) to frequency double the Yb-doped fiber laser centered at 1030 nm to 515 nm, as depicted in Figure 2.21. Figure 2.21 (a) and (b) provide an overview of the entire optical setup within

the ULI system following the SHG upgrade, while the corresponding layouts on the optical bench and the wall are presented in Figure 2.21 (c) and (d) respectively. All optical components downstream from the SHG output were replaced with components designed for the wavelength range covering 515 nm. The laser repetition rate was operated at 500 kHz and the pulse width remained at approximately 300 fs during the laser inscription process. As the laser wavelength decreases from 1030 nm to 515 nm, we anticipate a further reduction in the focal spot size while utilizing a microscope objective with the same NA of 0.55. This will allow us to create more compact optical devices and achieve higher precision in optical alignment.

2.3.2 Characterization of ULI waveguides inscribed by second harmonic light

We first fabricated the ULI waveguides on Eagle glass to evaluate the performance of second harmonic light at 515 nm. To optimize the transmission efficiency of the waveguide, we used a multi-scan technique where each longitudinal ULI scan along the waveguide will be laterally displaced by 0.4 μm for each subsequent scan to form a rectangular composite cross-sectional ULI profile. Figure 2.22(a) shows the cross-section photograph of the fabricated waveguide with 13 scans. Since the optical index profile results from the composite of the multi-scan ULI profile, the resulting optical mode field profile of the ULI waveguide can be tailored to match that of the single mode fiber or other fibers of different sizes and shapes. Figure 2.22(b) show the measured optical mode profiles of the fabricated ULI waveguides fabricated by 9 scans, 13 scans, and 17 scans, respectively. By adjusting the number of scans, the scan speed, the average laser power, and the laser repetition rate, we can find a condition that minimizes the optical propagation loss and maximizes the optical mode matching to the optical fiber. Figure 2.22(c-f) illustrate the propagation loss and coupling loss of the fabricated waveguides under various inscription conditions on Eagle glass. These results demonstrate that we achieved a minimum propagation loss of approximately 0.23 dB/cm when the waveguide was scanned 13 times, utilizing a pulse energy of 120 nJ and a scan speed of 10 mm/s. The corresponding coupling loss to an SMF-28 fiber, calculated using Equation 2.2, was estimated to be approximately 0.81 dB

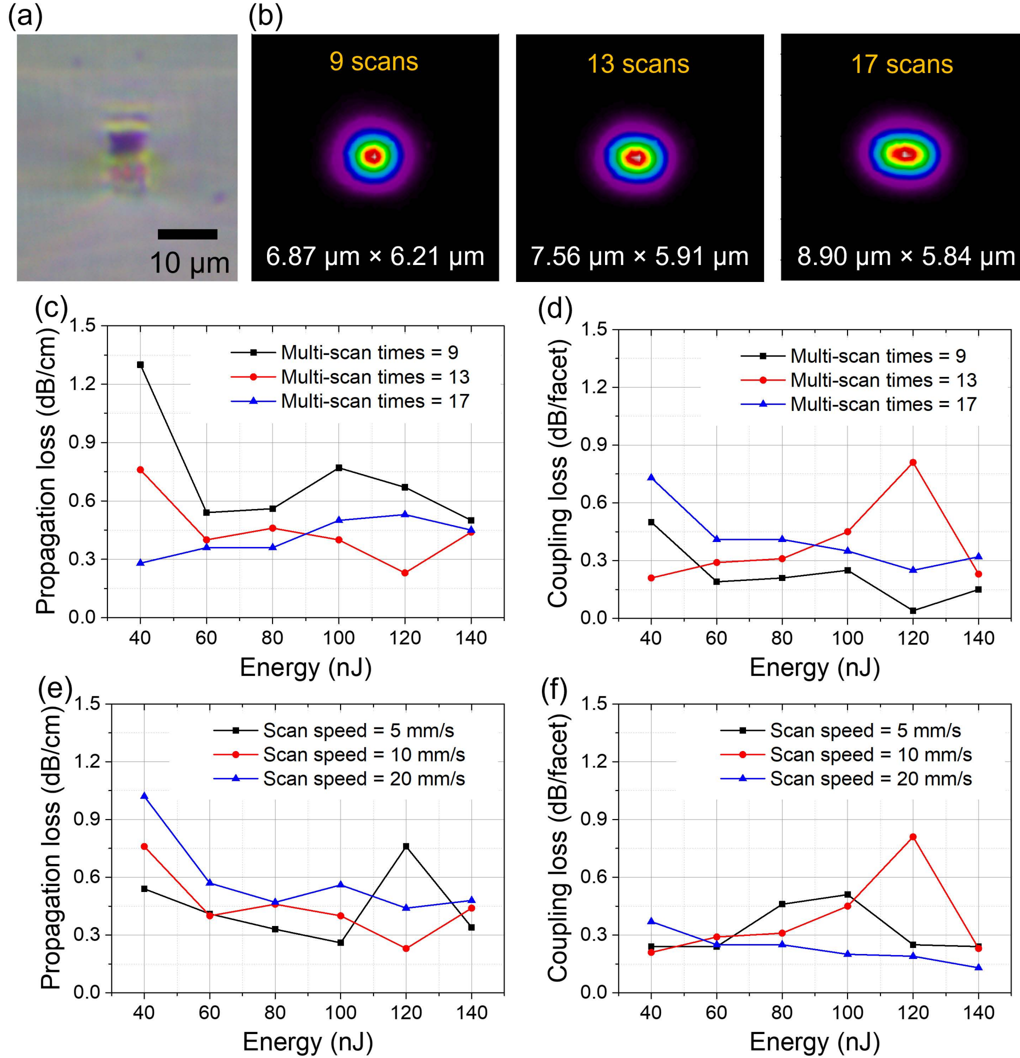

Figure 2.22. (a) Microscopic image of the cross-section of a ULI waveguide inscribed by 515 nm laser beam on Eagle glass. Measured mode profiles at 1550 nm for the ULI waveguides fabricated by (b) 9, 13, and 17 scans. Measured propagation loss and coupling loss of ULI waveguides as a function of the pulse energy at (c-d) different multi-scan times with the fixed scan speed of 10 mm/s and (e-f) different scan speeds with the fixed multi-scan times of 13.

per facet. When compared to the results obtained for 1030 nm laser inscription, as shown in Table 2.2(with a propagation loss of 0.44 dB/cm and coupling loss of 1.5 dB per facet), we achieved a remarkable improvement of approximately 48% in propagation loss and around 46% in coupling loss by using the 515 nm laser. Furthermore, we observed that under optimal conditions, specifically when the scan speed is set at 5 mm/s with pulse energies of 80, 100, and 140 nJ, the propagation loss remains below 0.35 dB/cm, and the

coupling loss stays under 0.6 dB per facet. These optimal conditions are particularly valuable for inscribing complex patterns that demand higher precision. The comprehensive measurement results are provided in Table 2.7.

Table 2.7. Measured optical loss of ULI straight waveguides on Eagle glass inscribed by a 515 nm laser beam under different inscription conditions.

Inscription condition	Total insertion loss (dB)	Coupling loss (dB/facet)	Propagation loss (dB/cm)
140 nJ, 10 mm/s, 9 scans	1.8	0.15	0.5
140 nJ, 10 mm/s, 13 scans	1.8	0.23	0.45
140 nJ, 10 mm/s, 17 scans	2	0.32	0.45
120 nJ, 10 mm/s, 9 scans	2.1	0.04	0.67
120 nJ, 10 mm/s, 13 scans	2.3	0.81	0.23
120 nJ, 10 mm/s, 17 scans	2.1	0.25	0.53
100 nJ, 10 mm/s, 9 scans	2.8	0.25	0.77
100 nJ, 10 mm/s, 13 scans	2.1	0.45	0.4
100 nJ, 10 mm/s, 17 scans	2.2	0.35	0.5
80 nJ, 10 mm/s, 9 scans	2.1	0.21	0.56
80 nJ, 10 mm/s, 13 scans	2	0.31	0.46
80 nJ, 10 mm/s, 17 scans	1.9	0.41	0.36
60 nJ, 10 mm/s, 9 scans	2	0.19	0.54
60 nJ, 10 mm/s, 13 scans	1.8	0.29	0.41
60 nJ, 10 mm/s, 17 scans	1.9	0.41	0.36
40 nJ, 10 mm/s, 9 scans	4.9	0.5	1.3
40 nJ, 10 mm/s, 13 scans	2.7	0.21	0.76
40 nJ, 10 mm/s, 17 scans	2.3	0.73	0.28
140 nJ, 5 mm/s, 13 scans	1.5	0.24	0.34
140 nJ, 20 mm/s, 13 scans	1.7	0.13	0.48
120 nJ, 5 mm/s, 13 scans	2.8	0.25	0.77
120 nJ, 20 mm/s, 13 scans	1.7	0.19	0.44
100 nJ, 5 mm/s, 13 scans	1.8	0.51	0.26
100 nJ, 20 mm/s, 13 scans	2.1	0.2	0.57
80 nJ, 5 mm/s, 13 scans	1.9	0.46	0.33
80 nJ, 20 mm/s, 13 scans	1.9	0.25	0.47
60 nJ, 5 mm/s, 13 scans	1.7	0.24	0.41
60 nJ, 20 mm/s, 13 scans	2.2	0.25	0.57
40 nJ, 5 mm/s, 13 scans	2.1	0.24	0.54
40 nJ, 20 mm/s, 13 scans	3.8	0.37	1.02

We repeated the experiment on another glass substrate containing germanium-oxide doping. Figure 2.23 shows the waveguide propagation loss and coupling loss of the ULI waveguides as a function of the scan speed at the multi-scan times at 5, 9, and 13 while maintaining a pulse energy at 100 nJ. The results indicate we achieve a record low loss of 0.16 dB/cm at a scan speed of 2 mm/s and scan times of 13 while the beam profile

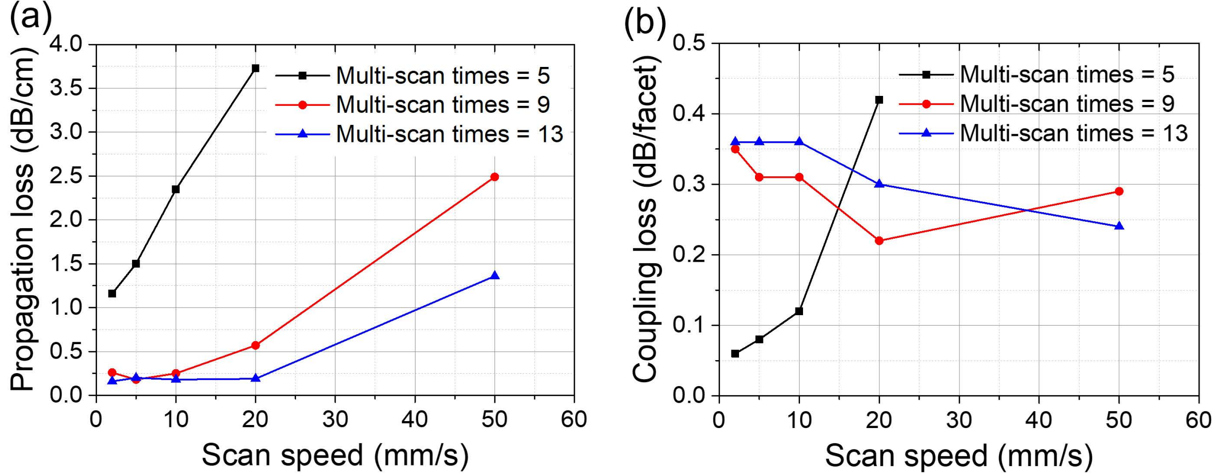

Figure 2.23. (a) Measured waveguide propagation loss and (b) coupling loss of the ULI waveguides on a glass containing germanium oxide doping as a function of the scan speed at the multi-scan times at 5, 9, and 13, achieving a record low loss of 0.16 dB/cm at a scan speed of 2 mm/s and scan times of 13.

indicates the coupling loss of 0.36 dB/facet to SMF-28 fiber. It is noted that with 13 times of multi-scan, the propagation loss remains below 0.2 dB/cm as the scan speed increases from 2 mm/s to 20 mm/s, while the coupling loss remains under 0.4 dB per facet. This remarkable outcome suggests a substantial reduction in fabrication time. Besides, when the ULI waveguide is fabricated by 9 scans, we can also achieve a propagation loss below 0.3 dB/cm and a coupling loss under 0.4 dB per facet at scan speeds below 10 mm/s. Regarding the ULI waveguides with 5 scans, the propagation losses consistently exceed 1 dB/cm when the scan speed is higher than 2 mm/s. These values are not suitable for fabricating low-loss optical devices. For more comprehensive measurement results, please refer to the detailed information provided in Table 2.8.

2.3.3 Design of three-dimensional fan-in/fan-out devices for multi-core fiber integration

Figure 2.24(a) and (b) illustrate the patterns for the waveguides at the two facets of the proposed fan-in/fan-out device. Given the standard fiber pitch for the optical fiber arrays, the input pattern was designed to be a linear array with a lateral waveguide spacing of 127 μm. The output facet for the MCF has a circular pattern of 8 waveguides with a core pitch of 40 μm. We utilized an automatic waveguide routing algorithm that assures

Table 2.8. Measured optical loss of ULI straight waveguides on a glass containing germanium oxide doping inscribed by a 515 nm laser beam under different inscription conditions.

Inscription condition	Total insertion loss (dB)	Coupling loss (dB/facet)	Propagation loss (dB/cm)
100 nJ, 2 mm/s, 5 scans	3.6	0.06	1.16
100 nJ, 5 mm/s, 5 scans	4.7	0.08	1.5
100 nJ, 10 mm/s, 5 scans	7.3	0.12	2.35
100 nJ, 20 mm/s, 5 scans	12	0.42	3.73
100 nJ, 2 mm/s, 9 scans	1.5	0.35	0.27
100 nJ, 5 mm/s, 9 scans	1.2	0.31	0.18
100 nJ, 10 mm/s, 9 scans	1.4	0.31	0.25
100 nJ, 20 mm/s, 9 scans	2.2	0.22	0.57
100 nJ, 50 mm/s, 9 scans	8.1	0.29	2.49
100 nJ, 2 mm/s, 13 scans	1.2	0.36	0.16
100 nJ, 5 mm/s, 13 scans	1.3	0.36	0.2
100 nJ, 10 mm/s, 13 scans	1.3	0.36	0.18
100 nJ, 20 mm/s, 13 scans	1.2	0.3	0.19
100 nJ, 50 mm/s, 13 scans	4.6	0.24	1.36

that (a) all ULI waveguides achieve the same optical path lengths (20 mm pathlength-matched waveguide array), (b) each ULI waveguide achieves a bending radius larger than the minimum bending radius (45.2 mm in this design) allowed to avoid bending loss beyond 0.1 dB, (c) no ULI waveguide will get closer to another waveguide than an allowed distance (30 μm in this design). Figure 2.24(c) shows the 3D schematic of the resulting eight waveguide array design and Figure 2.24(d-f) show the 2D projections of the design on the different planes.

In Figure 2.25 (a), the resulting design was confirmed to have the closest waveguide spacing to be 30.6 μm, which is large enough to avoid appreciable crosstalk between the waveguides. Additionally, Figure 2.25 (b) validates a minimum bending radius of 45.2 mm for each waveguide, ensuring negligible bending loss.

2.3.4 Fabrication and characterization results

The computer controlled 3-axis stage was employed to precisely control the motion of the sample according to the program to inscribe a 3D fan-in/fan-out device. The fan-in/fan-out structure was written at 80 $\sim$ 180 μm below the surface of the glass substrate to avoid

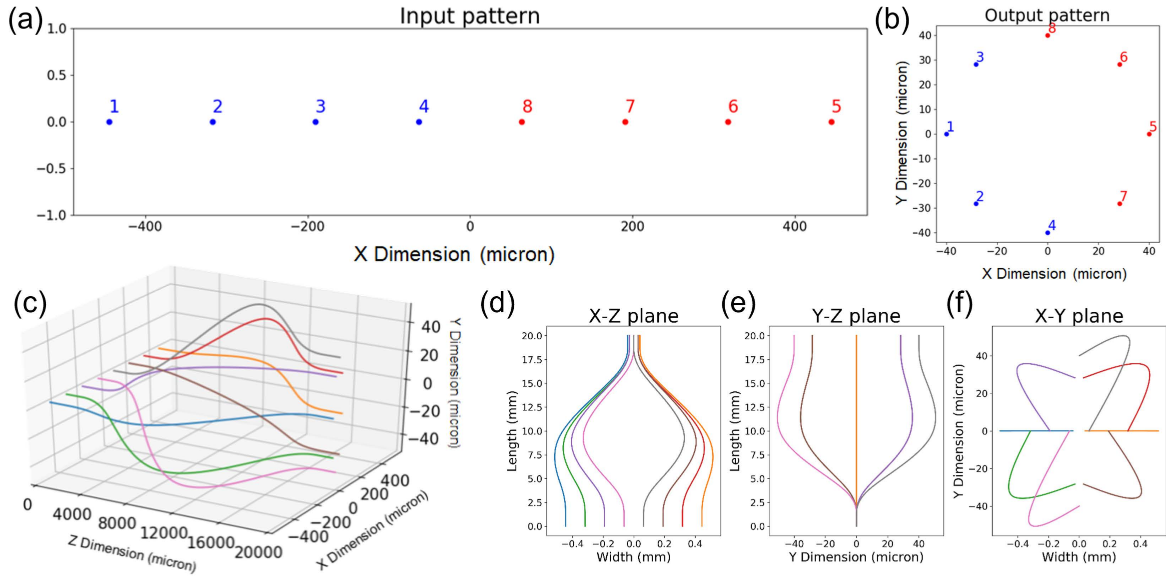

Figure 2.24. (a) The input pattern and (b) the output pattern for the proposed fan-in/fan-out device. (c) The schematic diagram for the waveguide design utilizing a routing algorithm. The 2D projections of the waveguide design on (d) X-Z plane, (e) Y-Z plane and (f) X-Y plane, where light propagation direction is along the Z-axis.

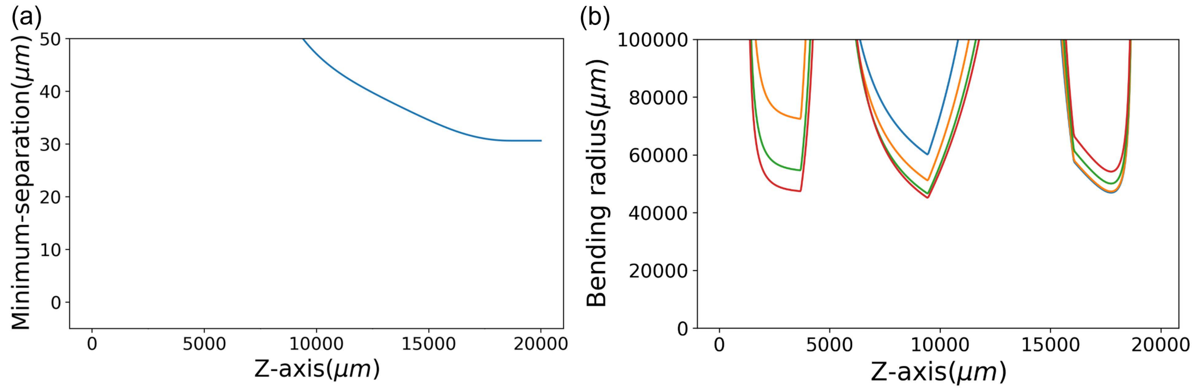

Figure 2.25. (a) Minimum separation distance between adjacent waveguides along the propagation direction. (b) Bending radius for each waveguide along the propagation direction.

the additional waveguide loss induced by the spherical aberration of the focused 515 nm pulses. Figure 2.26 (a) shows the fabricated fan-in/fan-out device with a footprint of 20 mm by 1 mm. The microscopic images shown in Figure 2.26(b) and (c) indicate good-quality waveguides inscribed by the optimum parameters chosen after the optimization process described in Figure 2.22. Figure 2.26(d) shows the inscribed waveguide at the

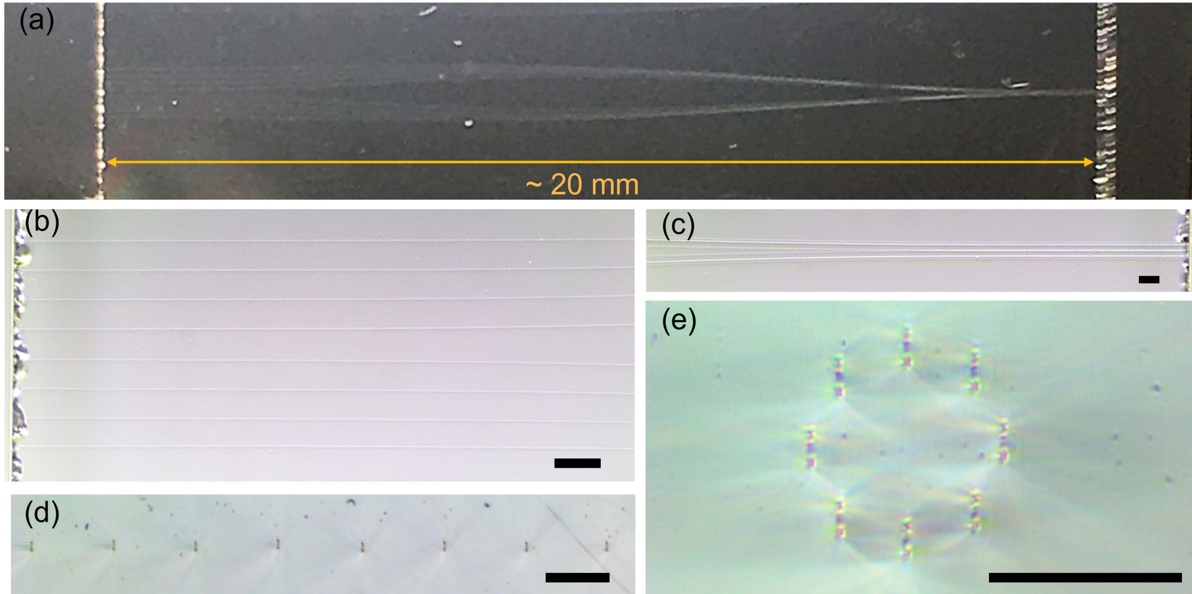

Figure 2.26. (a) Photo of the fabricated 3D fan-in/fan-out device for MCF integration. (b) Microscopic image of the interior where waveguides fan-out to a linear array. (c) Microscopic images of the interior where waveguides fan-in to a circular pattern. (d) Facet image of the input showing the linear array of 8 waveguides. (e) Facet image of the output showing the circular pattern of 8 waveguides. Scale bar = 100 μm.

fan out to eight SMF-28 and Figure 2.26(e) shows the inscribed waveguide at the fan-in to a MCF. Each cross-sectional profile of the waveguide based on the multi-scan ULI technique shows a distinctive rectangular core and the fabricated patterns show good agreement with the proposed design.

2.3.5 Summary

In summary, we demonstrate a 3D fan-in/fan-out device for MCF integration with a SMF-28 fiber array. An automatic waveguide routing algorithm for ULI was utilized to maintain the same photonic path lengths while optimizing the waveguide bending radius and inter-distance for compact and low-loss optical fan-in/fan-out. On the boro-aluminosilicate glass, we achieved a low propagation loss of 0.3 dB/cm and 0.8 dB/facet coupling loss to a SMF-28 fiber. On a glass substrate with germanium-oxide doping, we achieved an even lower propagation loss of 0.16 dB/cm and 0.36 dB/facet coupling loss to a SMF-28 fiber. These results indicate excellent prospects for realizing flexible and low-loss fan-in/fan-out devices and various 3D photonic packaging with MCF enabling high-density

and high-capacity future optical communications.

2.4 Three-dimensional arrayed waveguide grating routers fabricated by ultrafast laser inscription

2.4.1 Arrayed waveguide grating

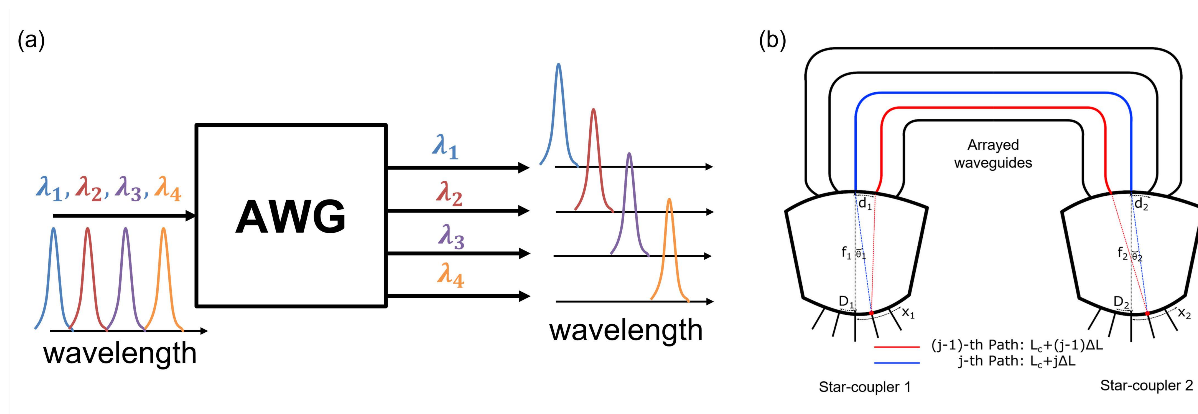

Figure 2.27. (a) Operating principle and (b) schematic of an arrayed waveguide grating (AWG).

Arrayed waveguide gratings (AWGs) have become indispensable tools for the multiplexing and demultiplexing of signals at various wavelengths, as depicted in Figure 2.27 (a).). Their versatility has led to diverse applications in fields such as optical wavelength routing [41], optical sensing [42], and spectroscopy [43]. As illustrated in Figure 2.27 (b), an AWG comprises input and output waveguides, two star couplers, and arrayed waveguides. In the first star coupler, light is diffracted within the free propagation region (FPR) and then enter the arrayed waveguides with a Gaussian distribution. Due to the linear pathlength difference between adjacent arrayed waveguides, light experiences constructive interference in the second star coupler, causing different wavelengths to be refocused into separate output waveguides. However, fabrication of traditional AWGs usually requires time-consuming lithography and chemical processes. Furthermore, these traditional AWGs are inherently two-dimensional (2D) planar devices due to fabrication constraints, potentially limiting their integration within three-dimensional (3D) packaging along with other photonic devices such as multicore fibers.

To address these challenges, we propose to employ the ultrafast laser inscription (ULI)

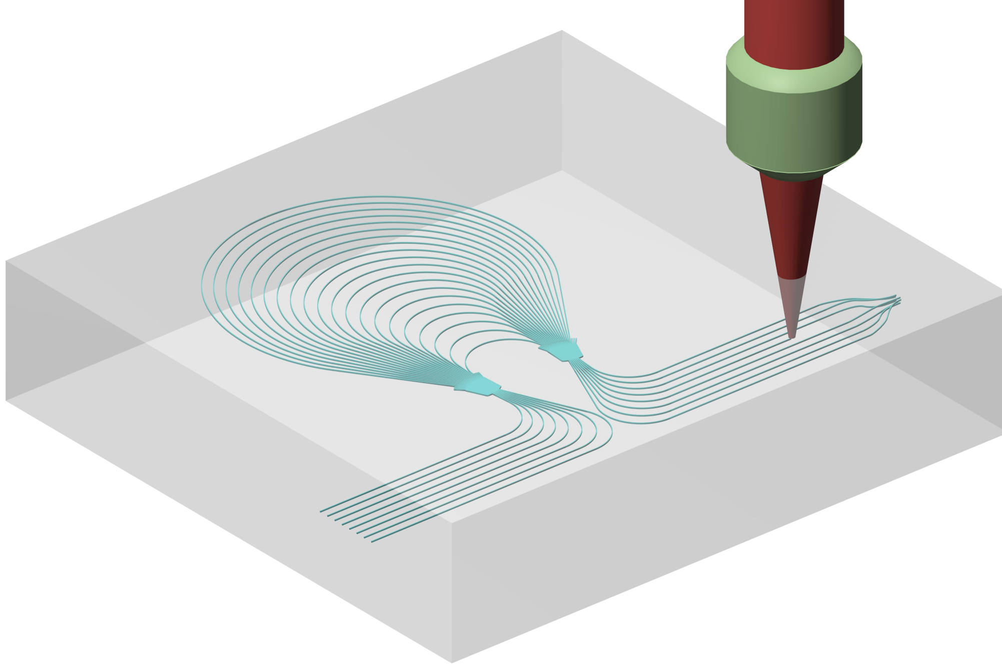

Figure 2.28. Schematic of three-dimensional arrayed waveguide grating fabricated by ultrafast laser inscription (ULI) technique.

technique to fabricate AWGs as illustrated in Figure 2.28. Through this approach, we can integrate an AWG with fan-in/fan-out structures, thus achieving a 3D AWG configuration. This newfound flexibility greatly enhances their compatibility with other photonic devices. Withford's group has previously demonstrated AWGs in the visible spectral range using femtosecond laser writing [44, 45], but their designs lacked separate output waveguides, limiting their functionality and integration with other photonic systems. Furthermore, AWGs designed for the near-infrared spectrum hold significant potential for optical fiber communication applications. In this work, we integrated the multi-scan technique with an AWG design tool to present a near-infrared arrayed waveguide grating router (AWGR) fabricated through ultrafast laser inscription. This ULI-based AWGR achieves a channel spacing of ∼400 GHz and a 3 dB-passband width of ∼2 nm.

2.4.2 Design and simulation

In the preceding subsections, we discussed our utilization of the multi-scan technique to finely tailor the shape of ULI waveguide cores, aimed at optimizing transmission efficiency. To design a high-performance ULI-based AWG, the dimensions and refractive index of

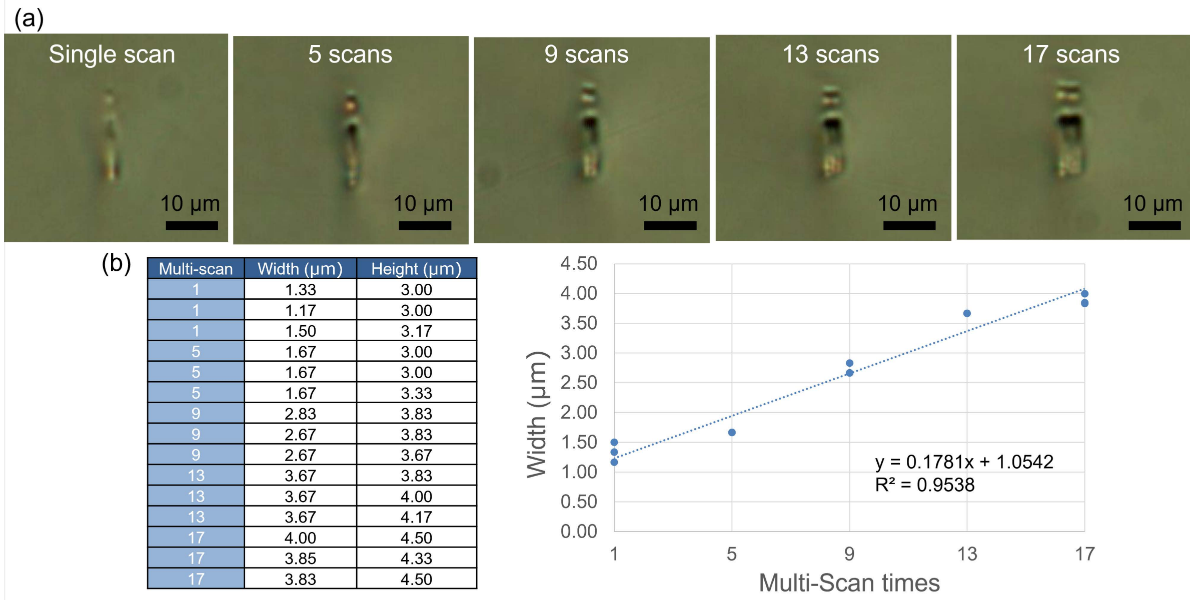

Multi-scan	Width (µm)	Height (µm)
1	1.33	3.00
1	1.17	3.00
1	1.50	3.17
5	1.67	3.00
5	1.67	3.00
5	1.67	3.33
9	2.83	3.83
9	2.67	3.83
9	2.67	3.67
13	3.67	3.83
13	3.67	4.00
13	3.67	4.17
17	4.00	4.50
17	3.85	4.33
17	3.83	4.50

Figure 2.29. (a) Microscopic images of the cross-section of ULI waveguides fabricated using single, 5, 9, 13, and 17 scans. (b) Measured waveguide width as a function of the multi-scan times.

the waveguide core play pivotal roles, necessitating thorough investigation. Therefore, in Figure 2.29, we estimate the dimensions of the waveguide cores fabricated using varying numbers of scans, ranging from a single scan to 17 scans. In Figure 2.29 (a), each longitudinal scan along the waveguide is laterally displaced by 0.2 μm for each subsequent scan to form a rectangular waveguide core. In order to ensure the stability of the motorized stage during the inscription of complex ULI structures, we reduced the scan speed from the previously determined optimal value of 10 mm/s to 2 mm/s. Consequently, the pulse energy was reoptimized to 80 nJ accordingly. Figure 2.29 (b) presents the detailed measured dimensions of the waveguide cores, and we employ fitting methods to accurately estimate the corresponding widths and heights.

To mitigate optical phase errors arising from waveguide sidewall roughness while keeping propagation loss low, we opted for the ULI waveguide with 17 scans as the single-mode waveguide in the proposed AWG design, as illustrated in Figure 2.30 (a). The corresponding beam profile at 1550 nm is captured in Figure 2.30 (b). The estimated dimension of the waveguide core is approximately 4.08 μm by 4.41 μm as shown in Figure 2.30 (c).

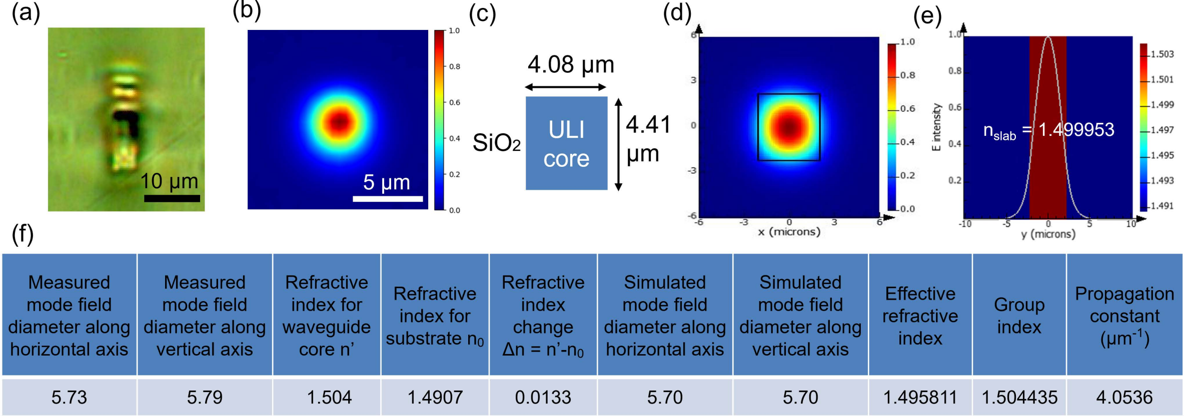

Measured mode field diameter along horizontal axis	Measured mode field diameter along vertical axis	Refractive index for waveguide core n'	Refractive index for substrate n_0	Refractive index change $\Delta n = n' - n_0$	Simulated mode field diameter along horizontal axis	Simulated mode field diameter along vertical axis	Effective refractive index	Group index	Propagation constant (μm^{-1})
5.73	5.79	1.504	1.4907	0.0133	5.70	5.70	1.495811	1.504435	4.0536

Figure 2.30. (a) Microscopic image for the cross-section of the ULI waveguide utilized as the single-mode waveguide in the proposed AWG design. (b) The measured mode profile at 1550 nm. (c) A schematic of the single-mode ULI waveguide with estimated core dimensions. (d) The simulated mode profile at 1550 nm.(e) The calculation of the effective index for the slab waveguide. (f) Optical properties of the single-mode ULI waveguide.

Once we determined the waveguide core dimension and mode field diameter, we employed Lumerical solutions to simulate the optical mode profile, aligning it with the measured results to derive the refractive index of the waveguide core. The simulated optimized mode field profile is depicted in Figure 2.30 (d), demonstrating a high degree of consistency with the measured result. It is noteworthy that We can achieve a refractive index contrast of 8.8×10^{-3}. To assess the diffraction of the slab region within the star coupler, we calculated the effective index of the slab waveguide, as presented in Figure 2.30 (e). Finally, Figure 2.30 (f) summarizes all the waveguide parameters required for designing an AWG.

We selected 1550 nm as the central wavelength for the AWG. For our initial demonstration, we set the channel spacing to 400 GHz. To minimize optical losses arising from mode mismatch between the star coupler and the arrayed waveguides, we implemented adiabatic tapers with a width of 6.04 μm at the waveguide ends. Regarding the waveguide pitch at the edge of the star couplers, we used 12 μm for input and output waveguides and 20 μm for the arrayed waveguides to prevent waveguide crosstalk. In terms of waveguide numbers, we employed 8 input/output waveguides and 32 arrayed waveguides, which is

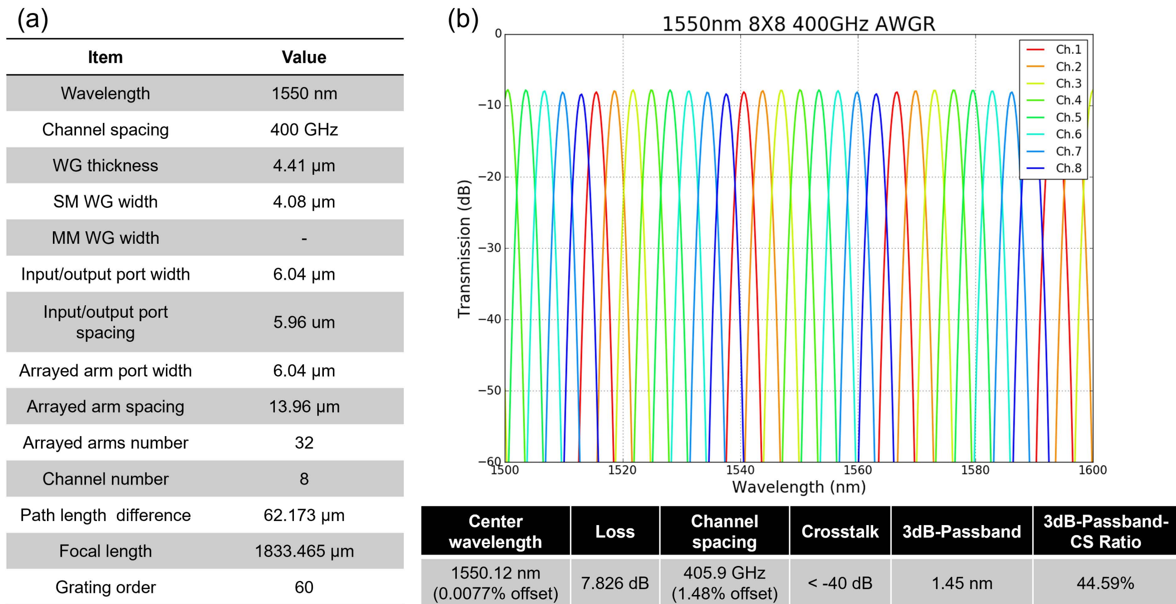

Item	Value
Wavelength	1550 nm
Channel spacing	400 GHz
WG thickness	4.41 µm
SM WG width	4.08 µm
MM WG width	-
Input/output port width	6.04 µm
Input/output port spacing	5.96 um
Arrayed arm port width	6.04 µm
Arrayed arm spacing	13.96 µm
Arrayed arms number	32
Channel number	8
Path length difference	62.173 µm
Focal length	1833.465 µm
Grating order	60

Center wavelength	Loss	Channel spacing	Crosstalk	3dB-Passband	3dB-Passband-CS Ratio
1550.12 nm (0.0077% offset)	7.826 dB	405.9 GHz (1.48% offset)	< -40 dB	1.45 nm	44.59%

Figure 2.31. (a) Design parameters for the AWGR and (b) calculated spectra for all the output waveguides.

four times the number of input/output waveguides. To ensure negligible bending loss, we set the minimum bending radius to 20 mm. Using an AWG layout tool based on Python and Ipkiss, we calculated that the required pathlength difference between adjacent arrayed waveguides is 62.173 μm. To create an arrayed waveguide grating router (AWGR), we set the grating order to 60. Figure 2.31 (a) outlines all these design parameters, and Figure 2.31 (b) displays the calculated spectra for all the output waveguides. The estimated loss for each output waveguide is approximately 7.826 dB, excluding the effects of propagation loss and defects caused by laser inscription. Furthermore, we achieved a 3 dB-passband of 1.45 nm while maintaining crosstalk below -40 dB in our design.

2.4.3 Layout and fabrication

The complete layout of the AWGR is depicted in Figure 2.32 (a). To ensure uniform effective indices for all the tapers surrounding the two star couplers, we added a few dummy tapers at their sides. The length of all adiabatic tapers is set to 300 μm to facilitate a low-loss transition of the optical mode profile. Additionally, in order to minimize noise resulting from nonuniform index profiles at the edge of the star coupler, we widened the

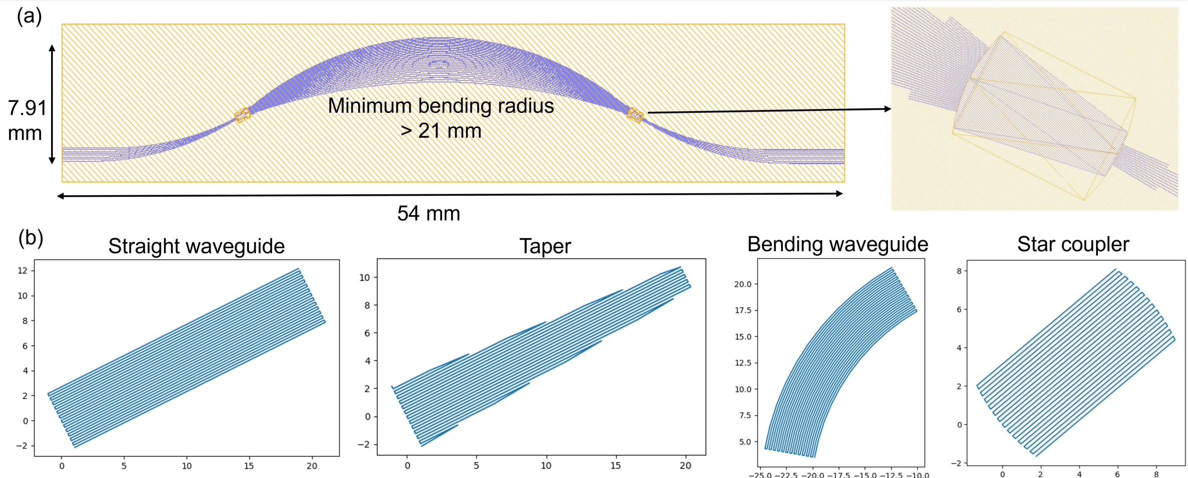

Figure 2.32. (a) The layout of the AWGR, with a footprint measuring 54 mm by 7.91 mm. The detailed view of the star coupler shows the widened star coupler and the inclusion of dummy tapers. (b) Multi-scan routes for each part of the AWGR.

star coupler, as highlighted by the orange frame in Figure 2.32 (a). This resulted in the star coupler dimensions of 2.6 mm by 1.8 mm. To guarantee negligible bending losses, we optimized the minimum bending radius to 21 mm, resulting in an AWGR footprint measuring 54 mm by 7.91 mm. In Figure 2.32 (b), we converted each part of the AWGR into multi-scan routes, with each longitudinal scan along the structure laterally displaced by 0.4 μm for each subsequent scan.

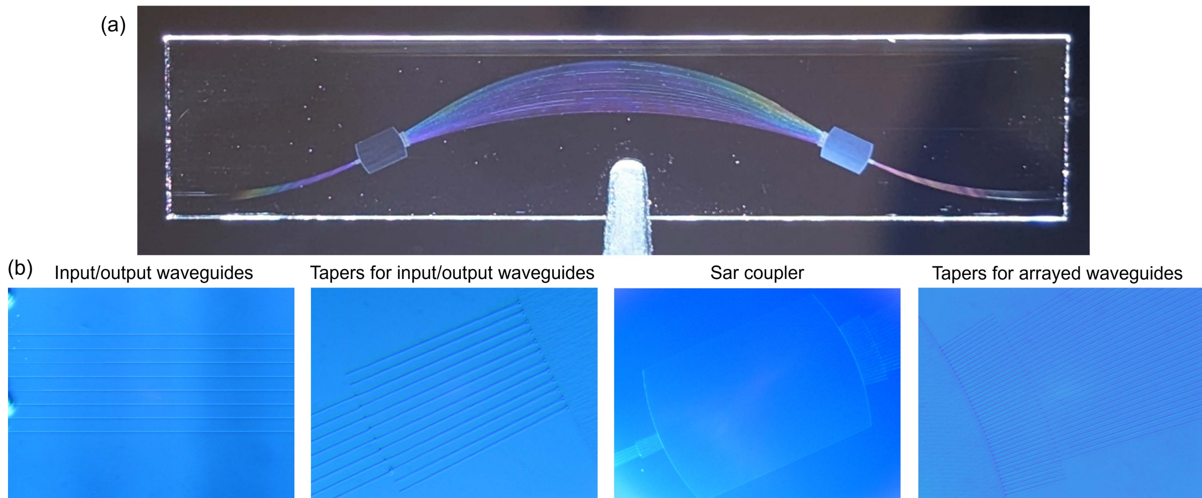

Figure 2.33. (a) The fabrication result of the complete AWGR. (b) Microscope images for each part of the AWGR.

Figure 2.32 (a) displays the fabricated AWGR on Eagle glass, with a total fabrication

time of approximately 8 hours. Meanwhile, Figure 2.32 (b) provides microscope images for each component, showing uniform and well-defined fabricated structures. However, we did observe some small defects in the form of spots at the boundaries between these components. These defects have the potential to impact the performance of adiabatic tapers and star couplers, possibly leading to increased optical losses. Apparently, these defects are a result of overlapping inscriptions between two components and a slowdown during the turning between subsequent scans. To mitigate these defects, we may consider adjusting the ramp rate of the motorized stage or further reducing the scanning speed in future designs.

2.4.4 Characterization results

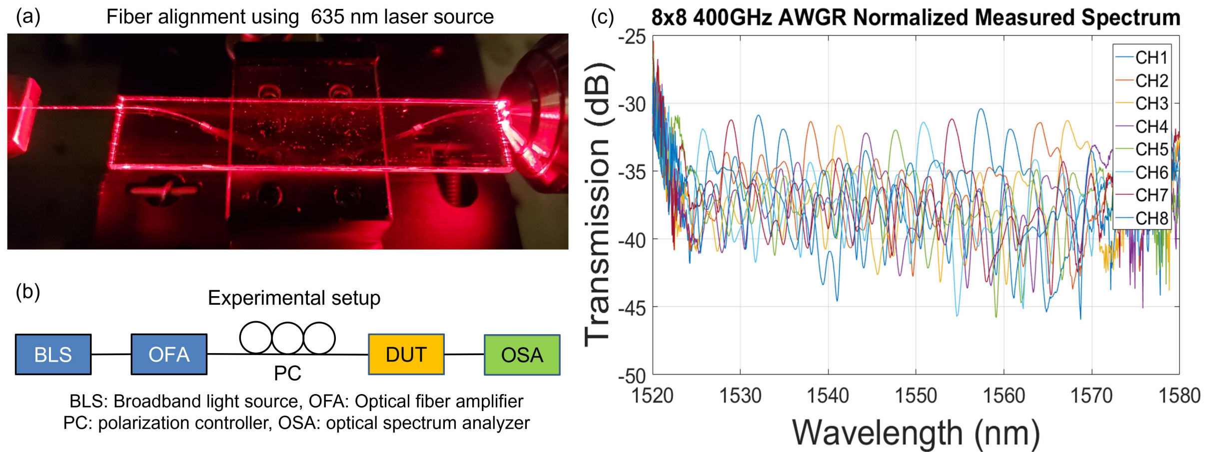

Figure 2.34. (a) Alignment of the AWGR and the input fiber by the use of a red laser. (b) Experimental setup. (c) Measured spectra for all the output waveguides.

The input and output waveguides of the fabricated AWGR were coupled to SMF-28 fibers for characterization. To aid in aligning the AWGR with the input fiber, we used a red laser to observe light coupling on the chip facet and subsequent light propagation within the AWGR, as depicted in Figure 2.34 (a). The measurement setup is schematically illustrated in Figure 2.34 (b). In this measurement, we employed a broadband light source (HP 83437A) with a peak wavelength of 1550 nm and a 3 dB bandwidth of 52 nm. To enhance the optical power, a 1.55 μm optical fiber amplifier (FITEL ErFA11106) was used, and a polarization controller ensured TE polarization for the input light. The light was coupled into the fifth input waveguide, and the output signals were directed to

an optical spectrum analyzer for analysis. The measurement results for all the output waveguides of the AWGR are presented in Figure 2.34 (c). The measured channel spacing of 399.1 GHz closely matches the designed value of 400 GHz. In the wavelength range of 1540 nm to 1560 nm, the average crosstalk was found to be 4.08 dB, and the average 3 dB-passband width was measured at 2.02 nm. The minimum measured loss was observed at 30.42 dB, occurring at a wavelength of 1557.38 nm from the eighth output waveguide. It's important to note that this result deviates significantly from the simulated values due to factors such as propagation losses and inscription defects, including spots on the taper and overlapping regions between different components.

2.4.5 Summary

We present, to the best of our knowledge, the first demonstration of a 3D AWGR operating at a wavelength of 1550 nm, achieved through ultrafast laser inscription. Leveraging a multi-scan technique, we optimized the performance of ULI structures, resulting in a remarkable refractive index contrast of 8.8×10^{-3}. Our design process employed an AWG layout tool based on Python and Ipkiss, facilitating automatic design and layout of the AWGR with specific device configurations. To ensure minimal bending losses, the minimum bending radius was optimized to 21 mm, resulting in an AWGR footprint of 54 mm by 7.91 mm. We also developed a routing tool based on Python to convert the AWGR layout into multi-scan routes for laser inscription. Our measurement results revealed a channel spacing of 399.1 GHz and a 3 dB-passband width of 2.02 nm. Additionally, we showed an AWGR device integrated with a fan-in/fan-out structure. Our ongoing objective is to further minimize optical losses in the AWGR and optimize phase errors induced by defects in the arrayed waveguides. These promising outcomes indicate the potential for realizing versatile AWGRs for 3D photonic packaging.

Chapter 3

Non-Mechanical Beam Steering Using Optical Phased Array

3.1 Principles

Optical phased arrays (OPAs) can enable non-mechanical beam steering through the phase control of each emitter. Figure 3.1 illustrates the design of an emitter aperture with mode size w_x and w_y, and the arrangement of an emitter array with pitch d_x and d_y. The radiation pattern ψ_{rad} for single emitter can be determined by

$$\psi_{rad}(\theta, \varphi, r) \propto \frac{e^{ikr}}{r} \int_{-\infty}^{\infty} \int_{-\infty}^{\infty} \psi_0(x, y) e^{ik \sin\theta (x \cos\phi + y \sin\varphi)} dx dy \tag{3.1}$$

where ψ_0 is the normalized radiation pattern. Then the array factor AF can be calculated as

$$AF(\theta, \phi) = \frac{\sin\left[\frac{\pi N d_x}{\lambda} (\sin\theta - \sin\theta_0)\right]}{\sin\left[\frac{\pi d_x}{\lambda} (\sin\theta - \sin\theta_0)\right]} \times \frac{\sin\left[\frac{\pi N d_y}{\lambda} (\sin\phi - \sin\phi_0)\right]}{\sin\left[\frac{\pi d_y}{\lambda} (\sin\phi - \sin\phi_0)\right]} \tag{3.2}$$

where N is the number of emitters and the emitter array is along the axis (θ_0, ϕ_0). The total field of the array is equal to the product of the radiation pattern ψ_{rad} for a single element and the array factor AF. Therefore, the total pattern can be controlled via the single element pattern ψ_{rad} or AF. While designing an OPA, we need to consider the requirements for the total field of view (TFOV), instantaneous field of view (IFOV or beam width), and sidelobe suppression. Here, the TFOV, which is the largest angle that OPA can steer to, is limited by the appearance of sidelobes, and the IFOV is inversely

proportional to the number of emitters *N*.

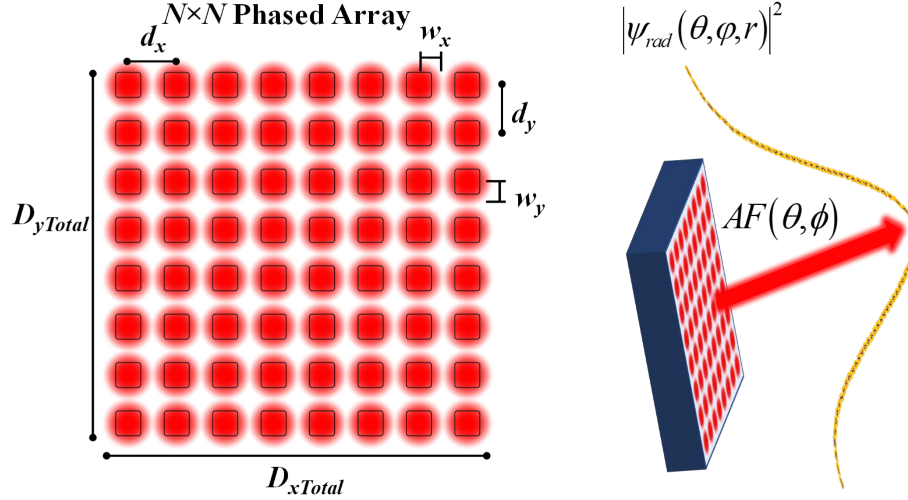

Figure 3.1. Schematic of an $N\times N$ phased array of emitters with mode size w_x and w_y, array pitch d_x and d_y, and total size $D_{xTotal}\times D_{yTotal}$. The output beam profile is determined by the product of single element radiation pattern ψ_{rad} and array factor AF.

The calculated far fields for beam steering in Figure 3.2 compare two situations where the emitter pitch is (a) greater than half wavelength and (b) less than half wavelength, as the phase difference between each emitter is tuned to 0, 0.5π, and 0.9π, respectively. When the emitter pitch is greater than half a wavelength, the occurrence of unwanted sidelobes will limit the TFOV and waste energy.

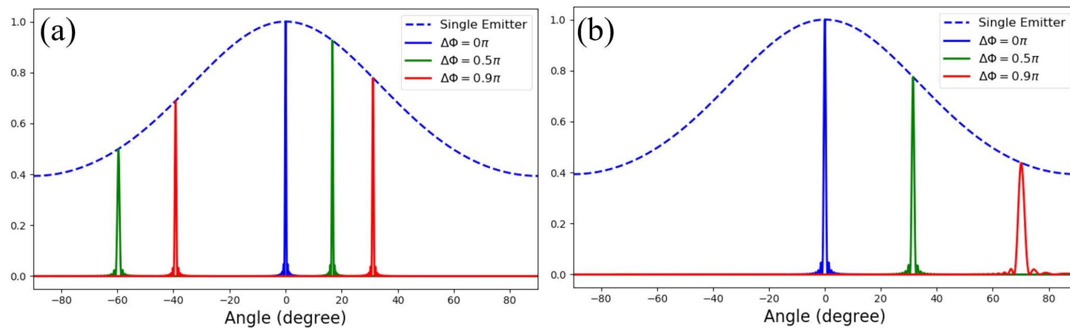

Figure 3.2. Simulated angular intensity distribution in the far-field for the phased array with $N = 128$, $w_x = w_y = 1$ μm, and (a) $d_x = d_y = 4.5$ μm and (b) $d_x = d_y = 2.2$ μm as the phase difference $\Delta\phi$ between emitters is tuned to 0π, 0.5π, and 0.9π at the wavelength of 4.6 μm.

3.2 Subwavelength silicon optical phase array with large field-of-view for near-infrared beam steering

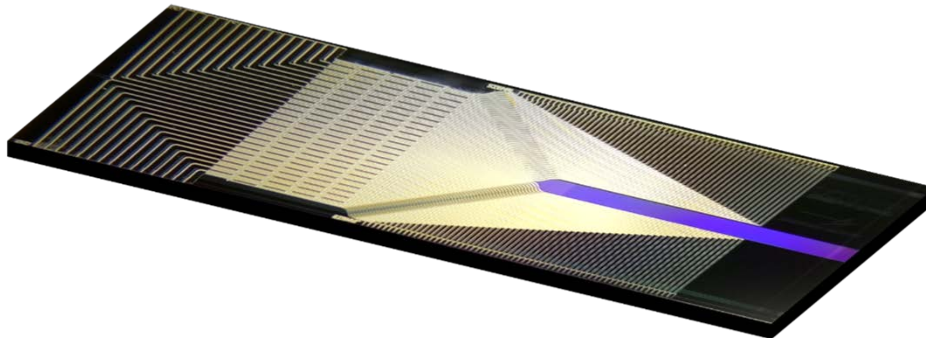

Figure 3.3. Schematic of an OPA device for 2D coherent optical beam steering

The current state of integrated OPAs typically involves element pitches that exceed the operating wavelength and a relatively small active aperture ($< \text{mm}^2$)[24, 26, 46–48]. However, this configuration imposes constraints on the field-of-regard and limits the operational range of LIDAR systems that rely on integrated OPAs. In this section, we aims to realize OPAs with subwavelength waveguide pitch and active emission area larger than 1 mm^2 on a silicon photonic platform. Figure 3.3 presents the schematic of our OPA device designed for 2D coherent optical beam steering at 1550 nm wavelength. In the following discussion, we will delve into the design optimization of key components including gratings, multimode interference splitters (MMIs), and distributed bragg reflectors (DBRs), and eventually evaluate the entire beam steering system.

3.2.1 Optimization of waveguide design

To enable beam steering with a wide field-of-regard, it is necessary to utilize a waveguide pitch in an OPA device that is smaller than the operating wavelength. In Figure 3.4 (a), we present the calculated sidelobe-free steering range for various waveguide pitches. As discussed in the previous section, sidelobes are effectively suppressed when the waveguide pitch is reduced to half of the operating wavelength, which in this case corresponds to 775 nm. Figure 3.4 (b) showcases the calculated far field patterns for an OPA consisting

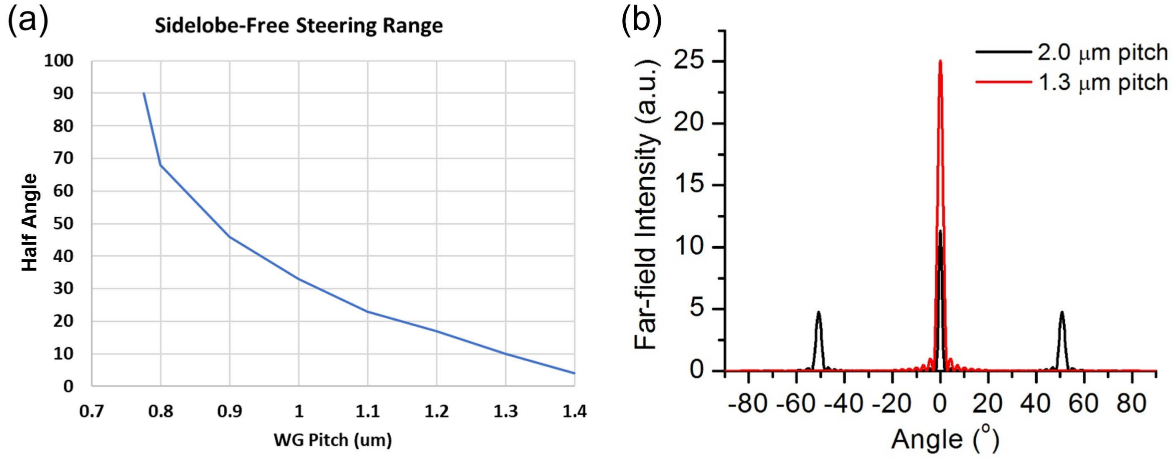

Figure 3.4. (a) Calculated sidelobe-free steering range as a function of the waveguide pitch. (b) Simulated far-field distribution of a 24-element array with waveguide pitches of 1.3 μm and 2.0 μm.

of 24 elements, considering waveguide pitches of 2 μm and 1.3 μm. The obtained results reveal that the configuration with a 2 μm waveguide pitch exhibits 0° of sidelobe-free steering range. Moreover, the presence of sidelobes in this case leads to additional power loss within the system.

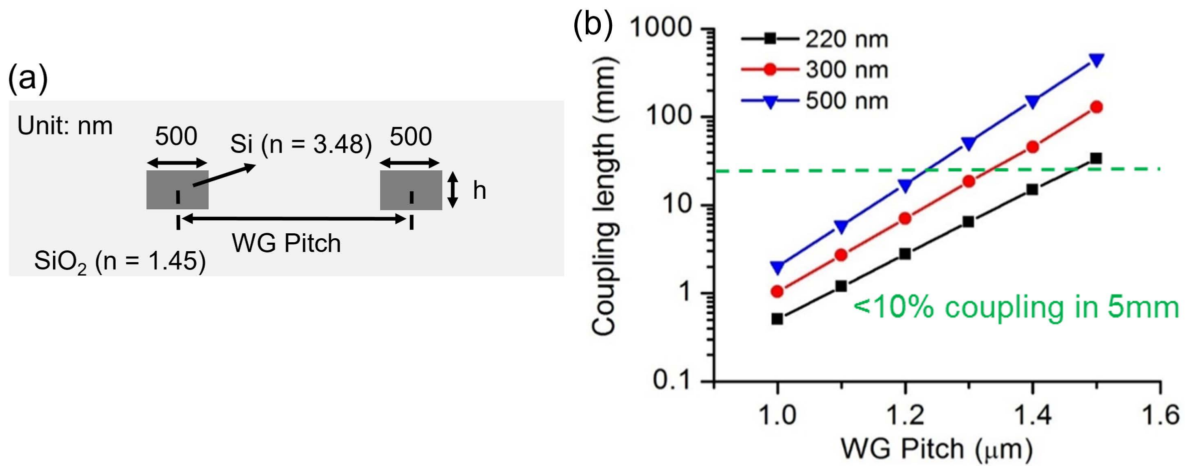

Figure 3.5. (a) Cross-sections of two silicon waveguides with a width of 500 nm in SiO_2 cladding. (b) Simulated coupling length as a function of waveguide pitch with silicon thicknesses of 220 nm, 300 nm, and 500 nm.

In addition to sidelobes, the size of the waveguide pitch also determines the level of crosstalk between adjacent elements. We employed COMSOL for simulating the optical coupling between two strip Si waveguides, each with a width of 500 nm as depicted in

Figure 3.5(a). The coupling length can be determined through the following calculation:

$$L = \frac{\lambda}{2\left|n_{\text{even}} - n_{\text{odd}}\right|} \tag{3.3}$$

Where n_{even} represents the refractive index of the symmetric mode of the super waveguide, while n_{odd} represents the refractive index of the asymmetric mode of the super waveguide. In Figure 3.5(b), we show the calculated coupling length for various waveguide pitches, considering waveguide thicknesses of 220 nm, 300 nm, and 500 nm. The results indicate that a minimum waveguide pitch of 1.3 μm is required to achieve less than 10 % coupling over a 5 mm interaction length. To minimize optical coupling, the Si thickness for the splitters and phase modulators is set to 500 nm. On the other hand, for the grating structures, a silicon thickness of 300 nm is chosen to ensure single-mode propagation.

3.2.2 Optimization of multimode interference splitters and distributed bragg reflectors

Once the laser beam is coupled into the input Si waveguide of the OPA device, it is directed to multiple waveguides using 1×2 multimode interference (MMI) splitters, as illustrated in Figure 3.6(a). To achieve equal power splitting and minimize excess loss, we utilized Lumerical FDTD Solutions for optimizing the MMI design. Figure 3.6(b-c) showcase the optimization process, resulting in an optimized design with a simulated field intensity distribution presented in Figure 3.6(d). The optimized design parameters include $W_{WG} = 0.5$ μm, $W_{taper} = 1$ μm, $L_{taper} = 5$ μm, $W_{sep} = 2$ μm, $W_{MMI} = 4$ μm, and $L_{MMI} = 16$ μm. Figure 3.6(e) shows the top-view SEM pictures of a fabricated single stage MMI splitter. In Figure 3.6(f), we present a comparison between the simulated and measured excess loss of our MMI design with different values of L_{MMI} ranging from 16 μm to 18.5 μm. The results demonstrate a remarkable consistency between the simulated and measured data, and the optimized MMI design achieved an impressive minimum excess loss of 0.08 ± 0.05 dB per MMI stage with $L_{MMI} = 16$ μm.

With the successful optimization of the MMI design, our focus now shifts towards addressing another critical aspect of loss reduction, specifically related to grating emission. In a conventional diffraction grating waveguide design, the waveguide gratings are

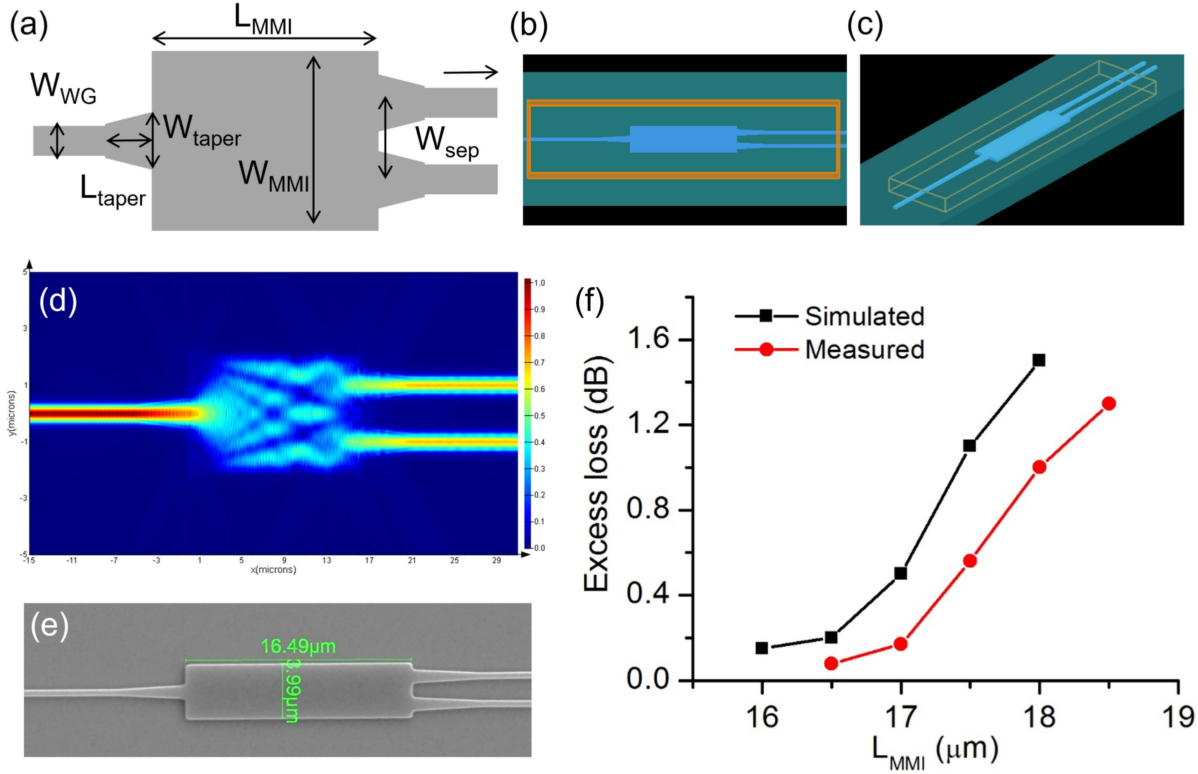

Figure 3.6. (a) Schematic of a MMI splitter. (b) Top view and (c) perspective view of the simulated MMI splitter. (d) Simulated intensity profile of the MMI splitter with $L_{MMI} = 16$ μm. (e) SEM picture of the fabricated single stage MMI splitter. (f) Simulated and measured excess loss of the MMI splitter as a function of MMI length.

designed to emit light evenly in both the upward and downward directions. This symmetrical emission pattern is a characteristic feature of standard diffraction gratings. To enhance the upward emission of light, we implemented a design strategy that involved the incorporation of two pairs of a-Si/SiO2 distributed Bragg reflectors (DBRs) beneath the grating waveguide layer. These DBRs were specifically engineered to reflect the undesired downward emission of light, redirecting it in the upward direction. In our proposed design, the distributed Bragg reflectors (DBRs) consist of three layers with thicknesses arranged from top to bottom: 108 nm, 269 nm, and 108 nm, as depicted in Figure 3.7(a). To further refine the design and explore its performance, we conducted simulations using Lumerical FDTD Solutions. Specifically, we swept the top and bottom oxide cladding thicknesses (T_{top} and T_{bottom}) of the waveguide grating illustrated in Figure 3.7(b-c) re-

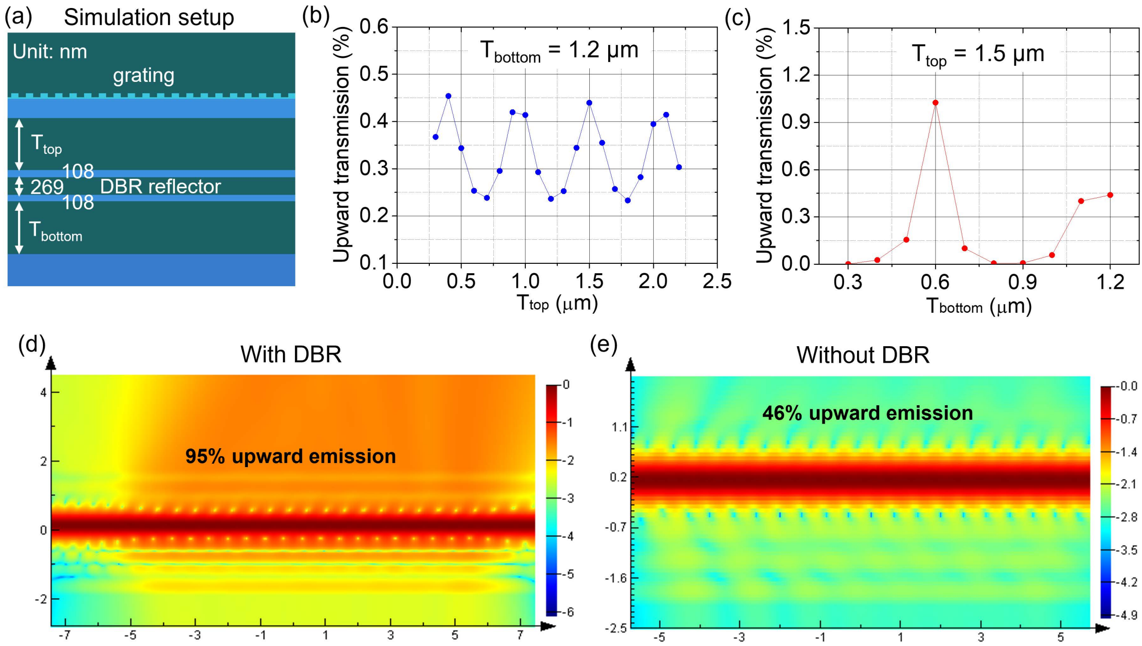

Figure 3.7. (a) Schematic of the FDTD simulation setup for the grating with DBR. Calculated upward transmission as a function of the top (b) and bottom (c) oxide cladding thickness. Simulated grating emission profile (d) with and (e) without bottom DBRs.

spectively to examine their influence on the upward emission. In Figure 3.7(d), we present the obtained optimized emitting distribution, showcasing a remarkable maximum upward emission efficiency of 95 %. This achievement is attributed to carefully chosen values of T_{top} and T_{bottom}, specifically set at 700 nm and 800 nm respectively. In contrast, when the DBR is not utilized, as demonstrated in Figure 3.7(e), the maximum upward emission efficiency drops to only 46 %.

3.2.3 Gratings with large emitting aperture

By employing a larger emitting aperture, the beam divergence can be effectively reduced, resulting in a more focused and concentrated beam that can travel longer distances with minimal loss. Besides, this enhanced beam quality enables improved range and resolution in LIDAR systems and other optical sensing technologies. To address the need for a large emitting aperture, we have proposed a novel approach utilizing a silicon nitride (SiN) assisted silicon grating with controlled emission strength. This innovative design allows us to achieve a significant increase in the emitting aperture size over a length of 5 mm, as

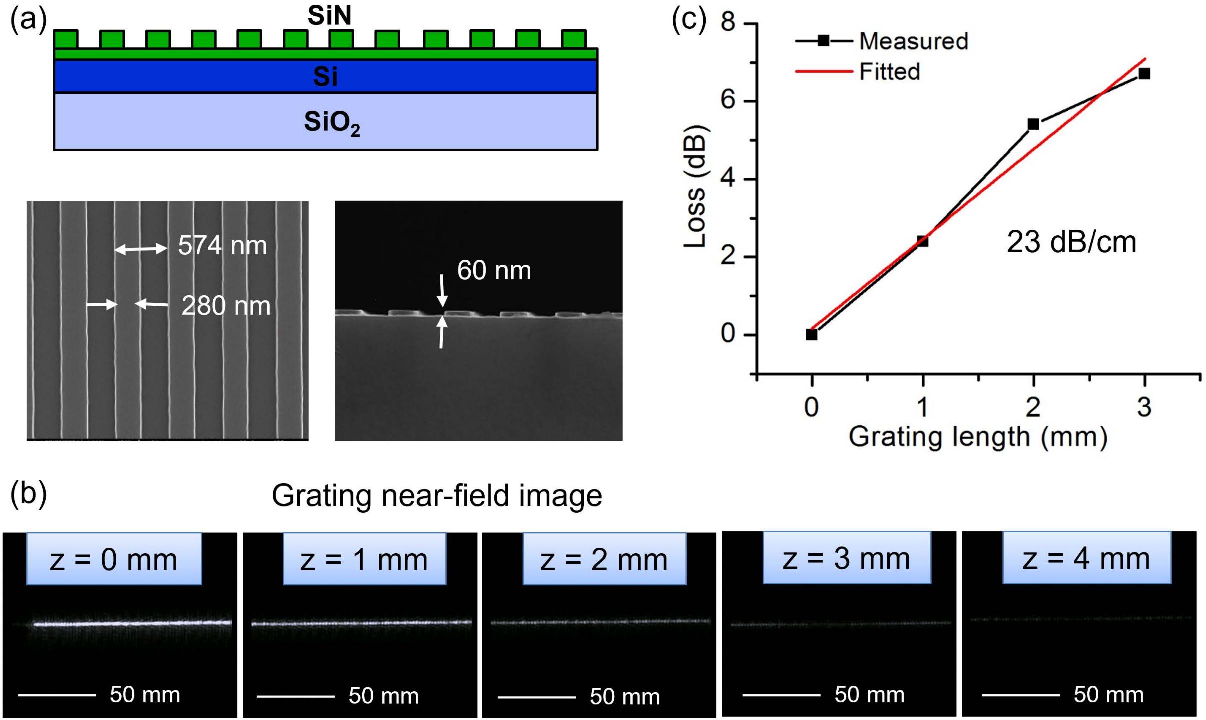

Figure 3.8. (a) Schematic, top-view, and cross-sectional-view SEM images of the fabricated SiN-assisted weakly emitting grating. (b) Measured near-field infrared (IR) image of the grating along its length. (c) Measured radiator loss of the grating as a function of its length.

demonstrated in Figure 3.8(a). In our innovative design, we have incorporated a deposition of approximately 80 nm thick silicon nitride (SiN) layer on top of the silicon waveguide. We then performed a partial etching of the SiN layer, removing approximately 60 nm of its thickness, resulting in the formation of a weakly emitting grating. By partially etching the SiN, we create a structure that emits light with reduced intensity compared to a fully intact grating. In Figure 3.8(b), we present the measurement results of the near field for a fabricated grating. To capture these images, we employed a NIR camera to scan along the length of the grating. In Figure 3.8(c), we estimated the emission rate to be 23 dB/cm by fitting the experimental data. This estimation indicates that approximately $\sim$95 % of the power is emitted over a length of 5mm.

3.2.4 Component characterization

Figure 3.9(a) shows a 120-element OPA fabricated using a standard silicon photonic fabrication process, with a waveguide pitch of 2.0 μm. Figure 3.9(b-d) present the fabrication

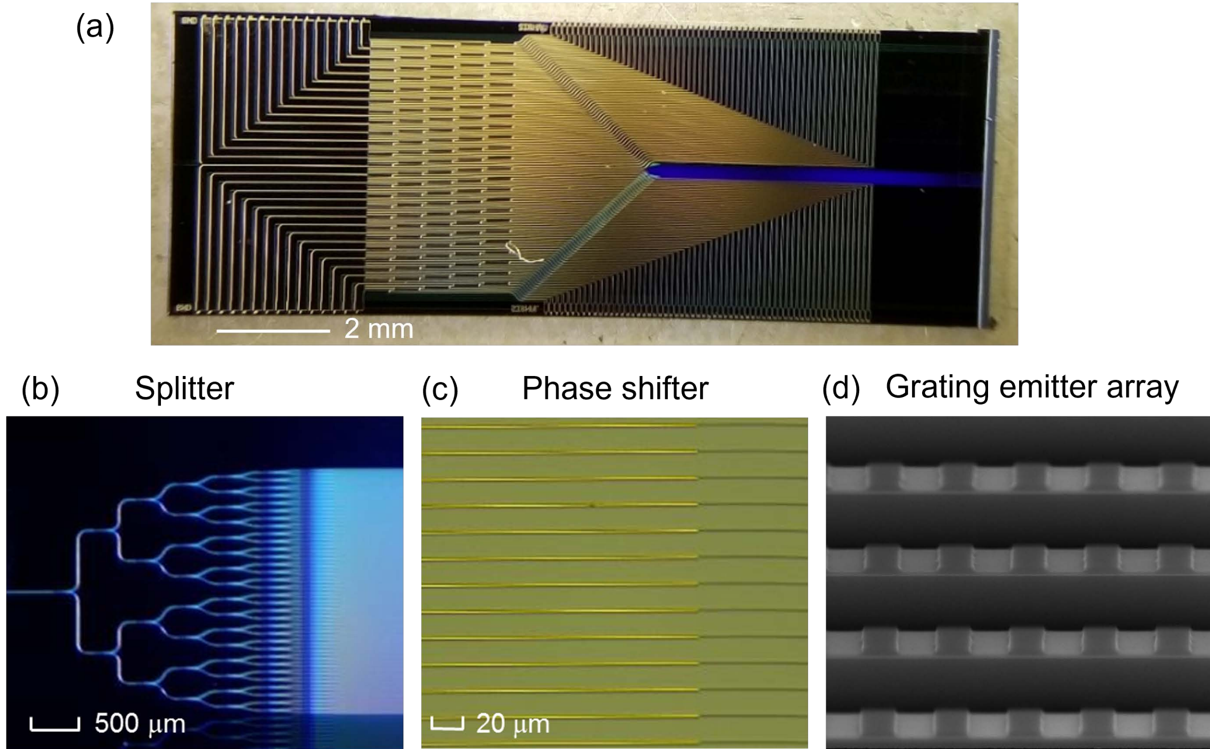

Figure 3.9. (a) Optical microscope image of the fabricated proof-of-concept 2D integrated silicon photonic unit cell. Zoomed-in views of (b) the MMI tree-based splitters, (c) the heater-based phase shifters, and (d) the grating emitter array with 2 μm waveguide pitch.

results for the MMI splitters, thermo-optic phase shifters, and SiN assisted grating emitter array, respectively. It is noted that 120 nm of Ti/Au metal is utilized to form the thermo-optic phase shifters, and the shifter pitch is fanned out to 38 μm to reduce thermal crosstalk from adjacent elements.

Figure 3.10(a) and (b) showcase the GDS layout of a 24-element OPA and the corresponding microscope image of the fabricated device. To perform the initial characterization, we designed and fabricated the OPA with three different waveguide pitches: 1.5 μm, 2 μm, and 4 μm. In Figure 3.10(c-t), we captured the near field images of these three OPAs by scanning across the entire grating. Similar to our observations in Figure 3.8(b), these grating emitter arrays demonstrate an exponential decay of emitting intensity along the length of the grating.

Building upon our examination of the near field patterns, we proceeded to investigate the corresponding far field patterns. In order to characterize the far field patterns of

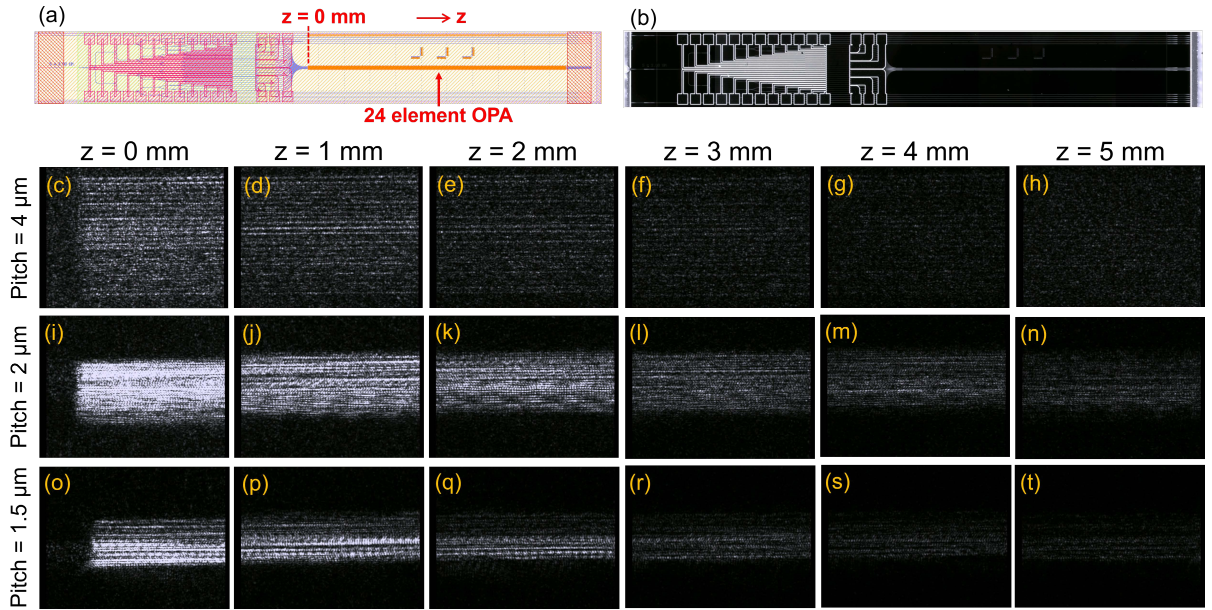

Figure 3.10. (a) GDS layout of a 24-element OPA and (b) the corresponding microscope image of the fabricated device. Measured near field images of the grating emitter array with the waveguide pitch of (c-h) 4 μm, (i-n) 2 μm, and (o-t) 1.5 μm.

our OPA beam steering device, we employed a two-lens far-field measurement setup, as illustrated in Figure 3.11(a-b). This setup consisted of a Mitutoyo objective lens (Lens 1) and an aspheric lens with a focal distance of 30 mm (Lens 2). This imaging system has a NA of 0.55, which corresponds to a field-of-regard of $\pm 33°$. After completing the setup, our initial measurement focused on capturing the far-field image of a single grating emitter. By tuning the operating wavelength in the range of 1545 nm to 1550 nm, we observed a noticeable axial beam steering effect as demostrated in Figure 3.11(c-d).

3.2.5 Beam steering characterization

Figure 3.12(a) shows the setup in which we mounted our 24-element OPA chip onto a metal chuck equipped with a thermo-electric cooler (TEC), enabling precise temperature control of the chip. To manipulate the voltages applied to the thermal tuners, we wire-bonded them to a printed circuit board (PCB) and connected them to digital-to-analog converters (DACs), as depicted in Figure 3.12(b). After that, we utilized a lensed fiber with 2 μm mode field diameter to couple the laser beam into the SiN edge coupler for our OPA device. Figure 3.12(c) presented the measured far-field IR image obtained when no

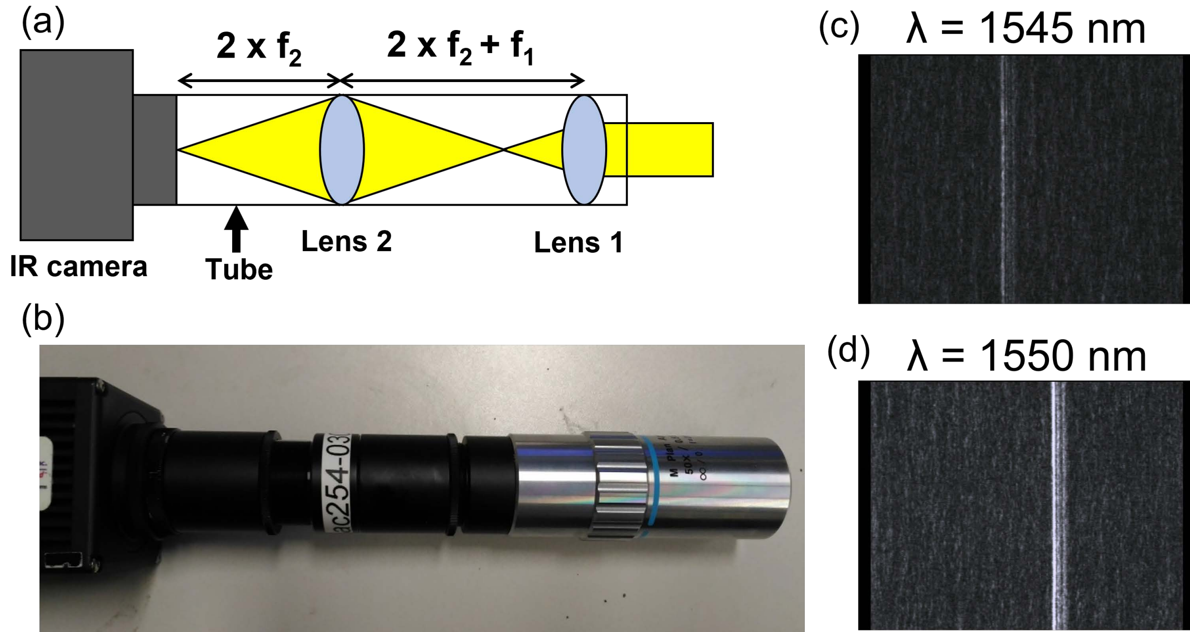

Figure 3.11. (a-b) The schematic and picture of the far-field measurement setup employed to characterize our OPA devices. Measured far field images of a single grating emitter under the operating wavelength of (c) 1545 nm and (d) 1550 nm.

voltages are applied to the thermal tuners. To mitigate the phase errors introduced during fabrication, we employed a gradient descent-based algorithm [49]. Through 10 iterations of this algorithm, we successfully corrected the phase errors and achieved a sharp beam spot at the intended far-field positions, as demonstrated in Figure 3.12(d).

Once the setup for phase error correction was fully developed, we proceeded to demonstrate two-dimensional beam steering using wavelength tuning and phase tuning. In Figure 3.13(a), we present the measured far-field images obtained by tuning the wavelength from 1540 nm to 1560 nm. These results demonstrate an efficient axial direction tuning capability, with a tuning efficiency of 0.15 °/nm. On the other hand, Figure 3.13(b) displays the measured far-field images obtained by applying three different sets of voltages to the thermal tuners. These results demonstrate a significant sidelobe-free steering range of over 40°.

It is worth noting that the measured side-lobe suppression, which is approximately 7 dB, is relatively lower compared to the simulated value of around 13 dB. We have identified two main factors contributing to this difference. Firstly, the unoptimized gradient descent

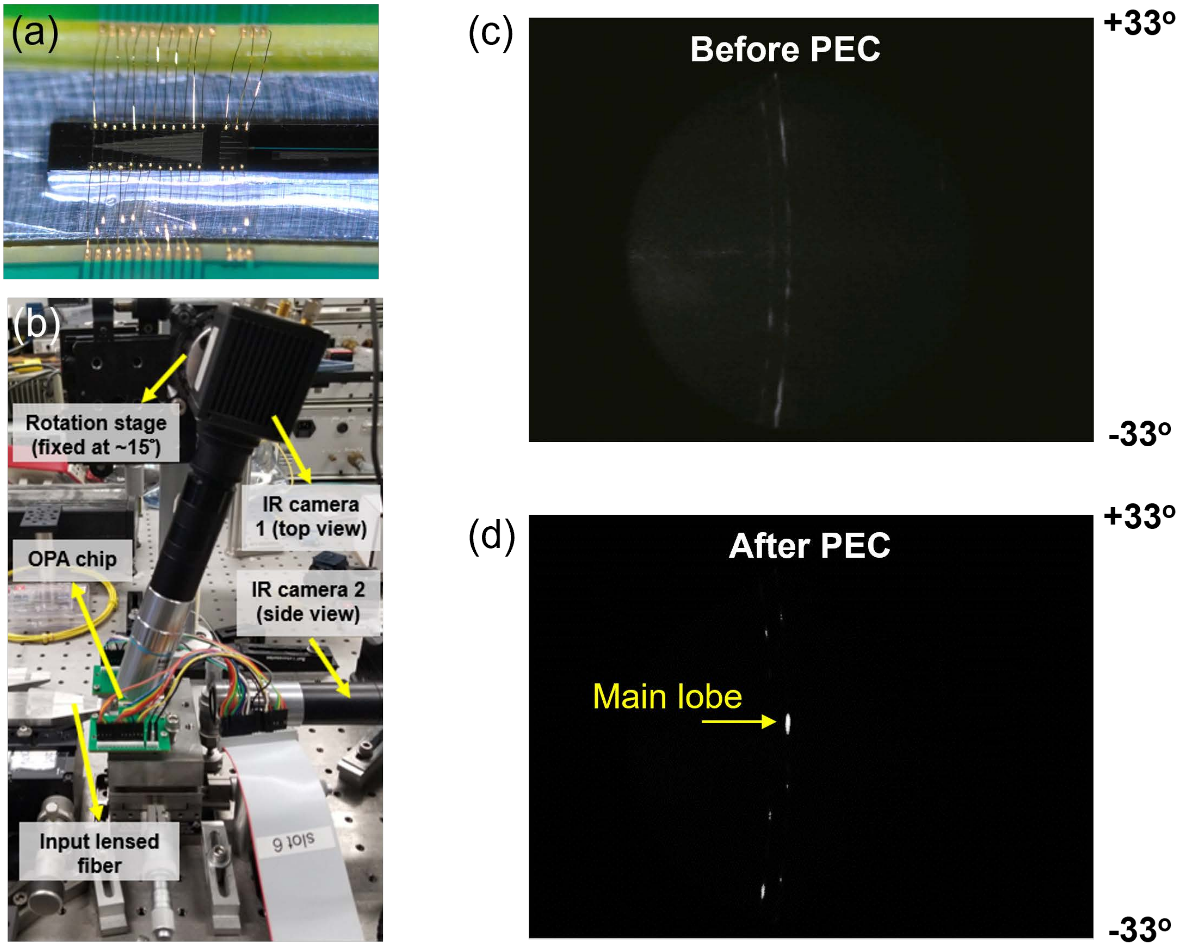

Figure 3.12. (a) Wire bonding of a 24-channal OPA device. (b) Experimental setup for OPA far-field measurement. Measured far-field IR images (c) before phase error correction (PEC) and (d) after phase error correction.

algorithm used in our experiments may have affected the performance of the beam steering system. Secondly, we also attribute the lower side-mode suppression to the presence of imperfect phased shifters. Specifically, we encountered issues with two open circuits after fabrication, and an additional open circuit problem occurred after the wire-bonding process. With the utilization of an advanced optimization algorithm [49], it is possible to achieve higher side-mode suppression.

In terms of the overall optical efficiency, it is estimated to be around -13.7dB, which can be attributed to various contributing factors. This efficiency can be decomposed as follows: the fiber-to-chip coupling loss accounts for 2.5 dB, the MMI splitting network

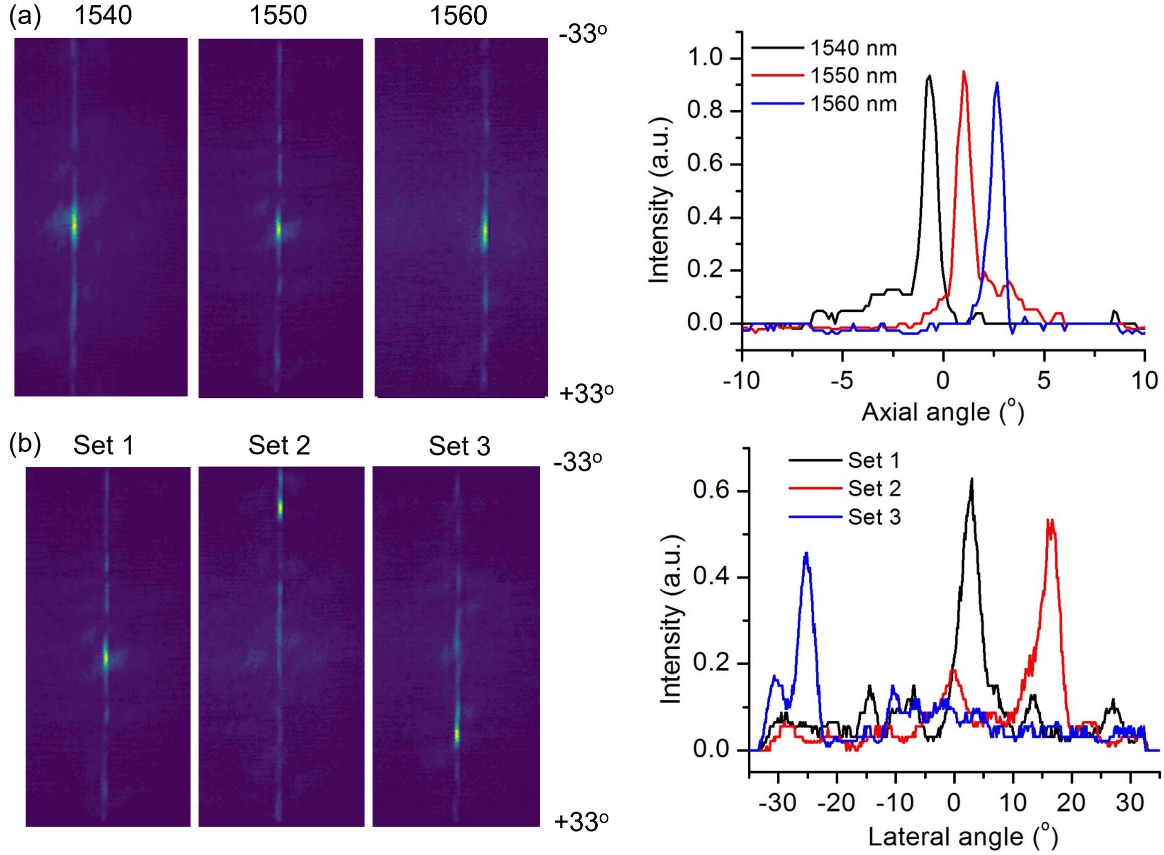

Figure 3.13. (a) Measured far-field image at different wavelength. (b) Measured far-field image at different phase gradient.

excess loss is 0.6 dB, the waveguide propagation loss is 5.2 dB, and the grating emission loss is 3.4 dB for downward emission, along with an additional 2 dB due to imperfections in co-phasing. To improve the grating emission efficiency, we anticipate a 3.2 dB enhancement by incorporating a bottom distributed Bragg reflector (DBR).

3.2.6 Summary

We successfully demonstrated an active OPA characterized by a large field-of-regard, high efficiency, and a large emitting aperture. The fabricated OPA devices comprised 24 elements, each featuring a 5 mm long emitting area and a waveguide pitch as small as 1.3 μm. Our experiments yielded impressive results, including a 3.3° axial beam steering achieved through a 20 nm wavelength tuning, and lateral beam steering capability exceeding 40°. Most notably, this lateral steering exhibited no sidelobes within the ±33° field-of-regard.

3.3 Optical phased array beam steering in the mid-infrared on germanium-silicon photonic platform

Most development of commercial solid-state LIDAR is focused on the 905 nm and 1550 nm wavelengths [50]. Extending the operational range into the mid-wave infrared (MWIR) wavelength can make such devices attractive for FSOC and gas-sensing applications [51] with lower sensitivity to atmosphere turbulence and scintillation [52, 53]. Furthermore, a longer wavelength can relax the half-wavelength pitch requirement for sidelobe-free beam steering [54] and reduce the fabrication complexity [55]. To develop a photonic platform for MWIR devices, germanium (Ge) is considered as an attractive candidate for its large transparency window of 2 μm to 14 μm [56]. Additionally, it is fully compatible with the complementary metal-oxide-semiconductor (CMOS) process and is a standard material for silicon photonics in very large-scale integration applications. A Ge-based platform also provides strong confinement in the waveguide core due to its high refractive index contrast. In this section, we propose to investigate and demonstrate non-mechanical, electronically controlled optical beam steering and beam formation by use of OPAs on a Ge-based platform. In the following work, we will use germanium (Ge) vertical emitters with HfO_2 cladding to achieve high TFOV, low IFOV, and low power consumption. The proposed vertical structure was inspired by our previous work for U-shaped photonic coupler [57].

3.3.1 Vertical emitter design

Since Ge has a large transparency window from 2 μm to 14 μm and is fully compatible with the CMOS process, a Ge-based photonics platform is an attractive candidate for mid-infrared photonics. Figure 3.14(a) illustrates the schematic of single Ge vertical emitter and Ge bus waveguide on Si substrate. Here, the vertical emitter consists of a coupler, 45° reflector, and a vertical via, and a bus waveguide is utilized to feed the light into the vertical emitters. Lumerical FDTD Solutions was utilized to simulate the optical characteristics for our structures, and a transverse magnetic (TM) polarized 4.6 μm light source was applied in the simulation. As Figure 3.14(b) shows, we changed the size of the

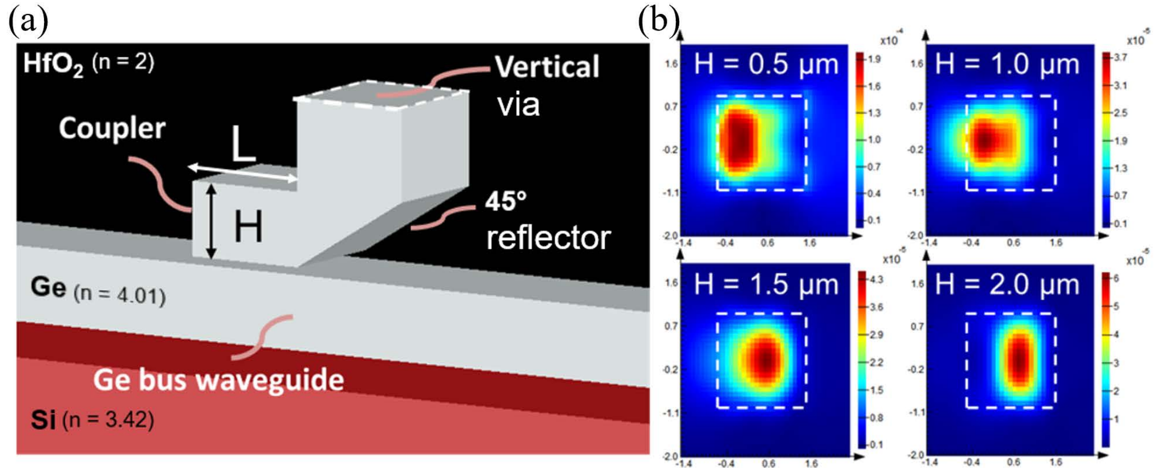

Figure 3.14. Layout of a vertical emitter and simulated emitted mode profiles for different values of H.

coupler while keeping the size of the Ge bus waveguide and the vertical via at $2{\times}2\ \mu m^2$. When H increases to 2 μm, the light can be well confined inside the vertical emitter and the mode profile of single mode can still be maintained. We attribute this to the optimal coupling under phase matching condition since the size of the coupler is equal to that of the Ge bus waveguide.

After optimizing the coupler size, we calculated the emitting efficiency for the vertical emitter. In our original design, we used Si as the material for the substrate. However, the efficiency for upward emission is slightly lower than that for downward emission, as shown in Figure 3.15. This relatively high efficiency for downward emission is due to the low refractive index contrast between the Ge bus waveguide ($n = 4.01$) and the Si substrate ($n = 3.42$). Therefore, we replaced the Si substrate with a SiN film (thickness = 200 nm) and a SiO_2 substrate to increase the contrast. Additionally, we leave a gap between the coupler and the bus waveguide to make the light in the bus waveguide be evanescently coupled into the coupler. In this way, we can vary the length of the coupler to manipulate the strength of coupling. To maximize the coupling efficiency, the gap is set to 20 nm.

In order to achieve low IFOV (smaller beam width) for beam steering, it is important to have uniform emission intensity across all the emitters by properly varying the coupling strengths of each coupler. In Figure 3.16(a), the coupler length of the vertical emitter is

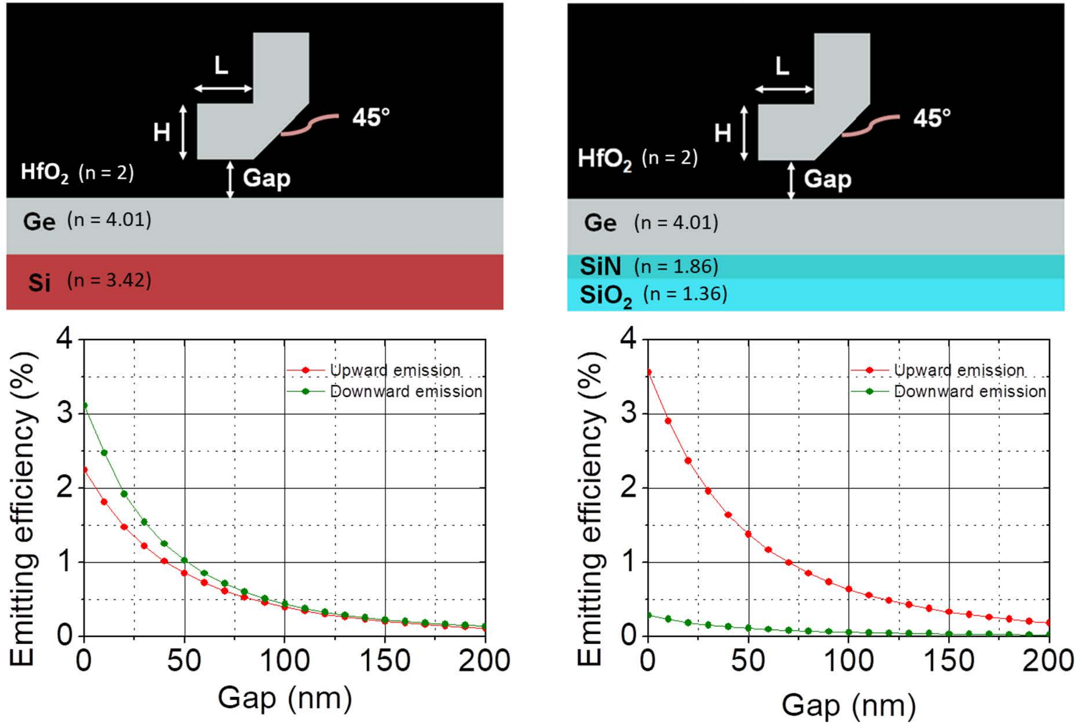

Figure 3.15. Layouts of a vertical emitter ($H = 2$ μm, $L = 2$ μm) and calculated emitting efficiency as a function of the gap between the coupler and the substrate when the bottom is a Si substrate (left) vs. a SiO_2 substrate with a SiN film (right).

varied to change the coupling efficiency between the bus waveguide and the coupler. In this manner, we can increase coupling efficiency to ∼27 % as coupler length is increased to 4 μm. Figure 3.16(b) illustrates the power-feeding network for our vertical emitter array. The coupler length is gradually increased along the emitter array to enhance the strength of evanescent coupling and maintain the same efficiency of upward-emitting light from each vertical emitter. Since we will pursue and eventually demonstrate 128×128 OPA beam steering, the ideal upward emitting efficiency for each vertical emitter is ∼0.78 % if there is no extra loss in the power-feeding network. However, we must consider the inevitable power loss in the end-of-bus waveguide, which is attributed to the maximum coupling efficiency between the bus waveguide and the coupler. The following equation describes the relationship between the upward emitting efficiency and the maximum coupling efficiency:

$$\frac{\text{Upward emitting efficiency}}{100\% - (N-1) \times \text{Upward emitting efficiency}} \leq \text{Maximum coupling efficiency} \quad (3.4)$$

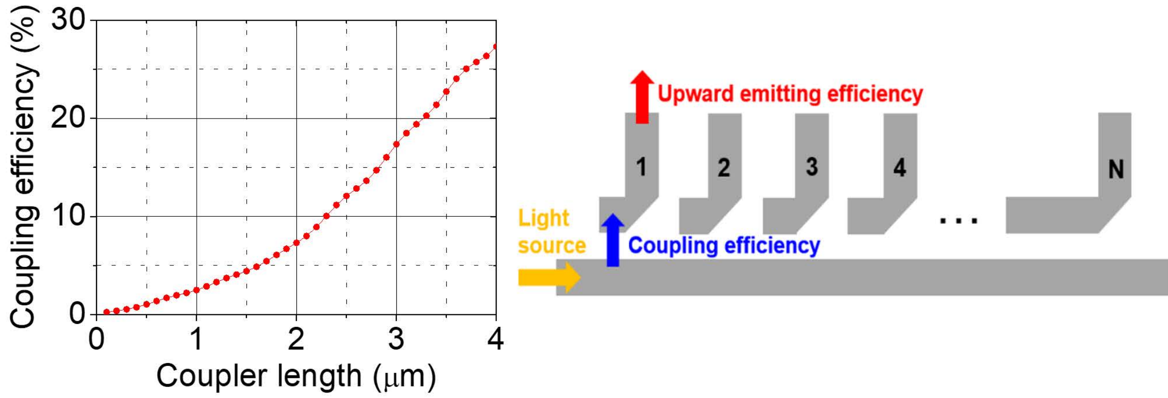

Figure 3.16. (a) Calculated coupling efficiency as a function of coupler length for a simulated vertical emitter. (b) Layout of the power feeding network where the optical power in the bus waveguide is uniformly coupled into N vertical emitters through evanescent waves.

If $N = 128$ and the practically achievable maximum coupler length is 3.5 μm, which corresponds to maximum coupling efficiency of 23 %, we can obtain an upward emitting efficiency of ∼0.76 %. Therefore, this causes only a negligible power loss of ∼2.56 %. Due to limited computational resources, the following simulation will focus on a 32-element phased array.

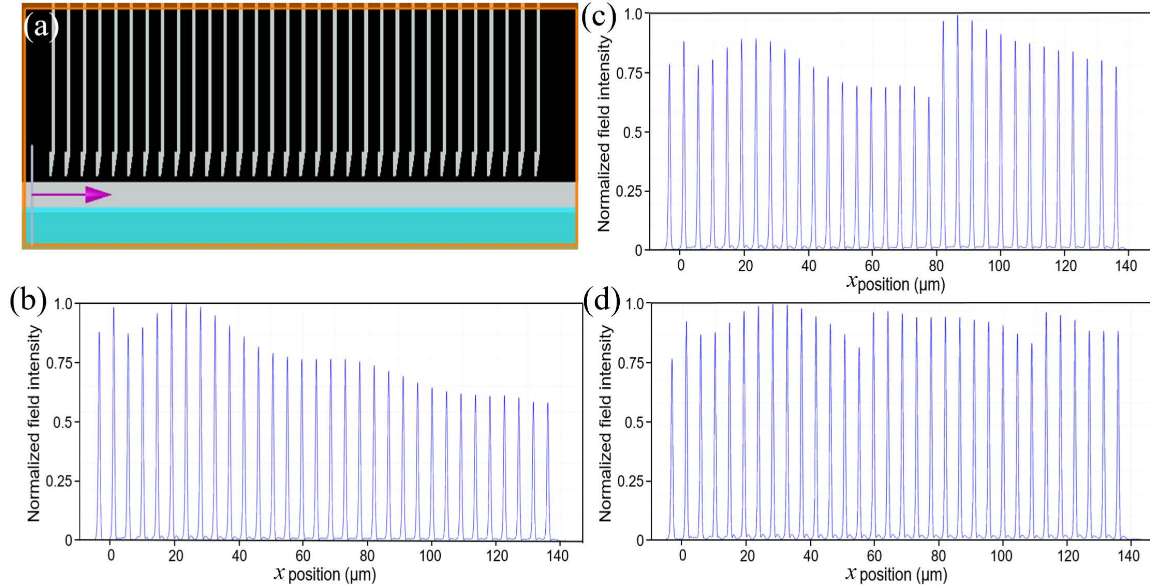

Figure 3.17. (a) Side view of a row of simulated vertical emitters with $N = 32$. Calculated normalized field intensity distribution on the top of simulated vertical emitters with (b) no change on coupler length, (c) $\Delta L = 100$ nm and (d) $\Delta L = 50$ nm.

After considering the requirements for uniform emission, we simulated a row of vertical emitters to check the global behavior of the system, as shown in Figure 3.17(a). For a decent simulation time, we limited the number of elements to 32. The first coupler length is chosen to be 0.7 μm to satisfy the requirement for the emitting efficiency when $N = 128$. The field intensity distribution in Figure 3.17(b) without varying the coupler length shows the expected upward emission calculated from a single vertical emitter. Note that the emitting power from each emitter doesn't decrease smoothly along the emitter array. This is because the light coupling from the bus waveguide to the couplers induces some perturbation in the bus waveguide, which needs to be further optimized. In Figure 3.17(c), we make the whole emission more uniform by varying the coupler length with $\Delta L = 100$ nm along emitter array. If the fabrication process is doable, we can further obtain a more uniform emission by reducing ΔL to 50 nm, as shown in Figure 3.17(d).

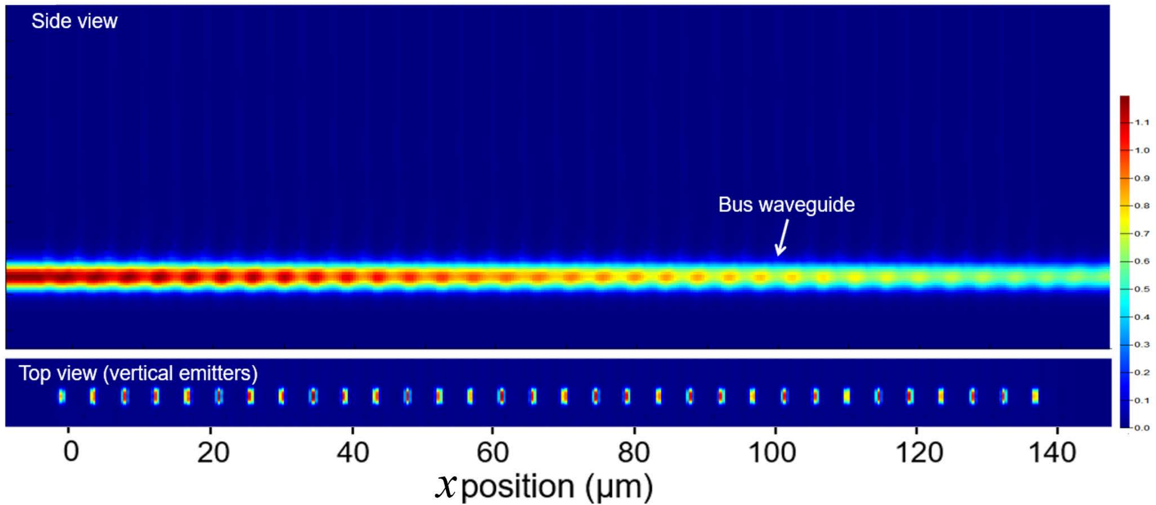

Figure 3.18. Side view and top view of simulated field intensity distribution for the whole power-feeding network system.

Figure 3.18 shows the 2D field intensity distribution for the case of $\Delta L = 50$ nm. From the side view, the light propagating inside the bus waveguide is fed into each vertical emitter and gradually decreases along the emitter array as we expected. The top view also demonstrates a very uniform emission from all 32 elements.

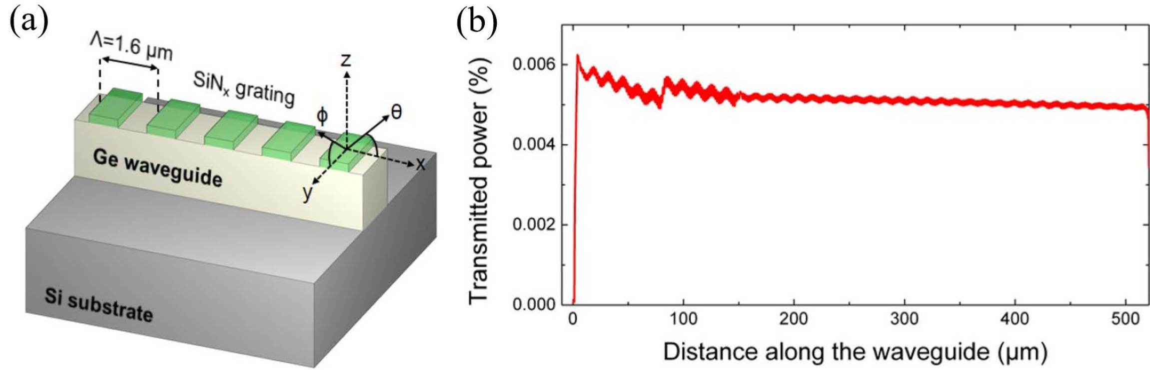

Figure 3.19. (a) Schematic of SiN_x grating with custom duty cycle on the top of germanium waveguide. (b) Simulated near field for the emission from SiN_x grating.

3.3.2 Beam steering experiments for light grating emitters

Before the fabrication technology for the Ge vertical emitter array is fully developed, we first demonstrate a 2D beam-steering PIC using grating emitter arrays for proof-of-concept. Figure 3.19(a) illustrates the schematic of the grating emitter design with custom duty cycle. Based on our previous work for the silicon photonics platform [58], we designed a SiN_x-assisted germanium grating that is apodized to achieve uniform emission as in the simulation result shown in Figure 3.19(b). Here, the duty cycle is modulated to have weak emission strength at the waveguide input and the width is varied as well to keep the propagation constant uniform. The total length of the grating is over 2 mm, which will result in a sharper IFOV in the far field for beam steering. The custom grating is composed of a 160-nm-thick SiN_x overlayer on the Ge waveguide and a grating period of 1.6 μm, which corresponds to the diffracted angle of 45° when $\lambda = 4.6$ μm.

Figure 3.20(a) presents a fully packaged non-mechanical beam-steering device including the low-loss waveguides, multimode interference (MMI) tree splitter, thermo-optical phase-shifter, fan-in structure, and a 2-mm-long 12-channel grating emitter array. The MWIR source used in the characterization is a quantum cascade laser (QCL) from Daylight Solutions operated in continuous wave with the center wavelength of 4.6 μm and the tuning capability range of 180 nm. We first measured the propagation loss using the cut-back method with cm-long spiral waveguides. The propagation loss extracted from

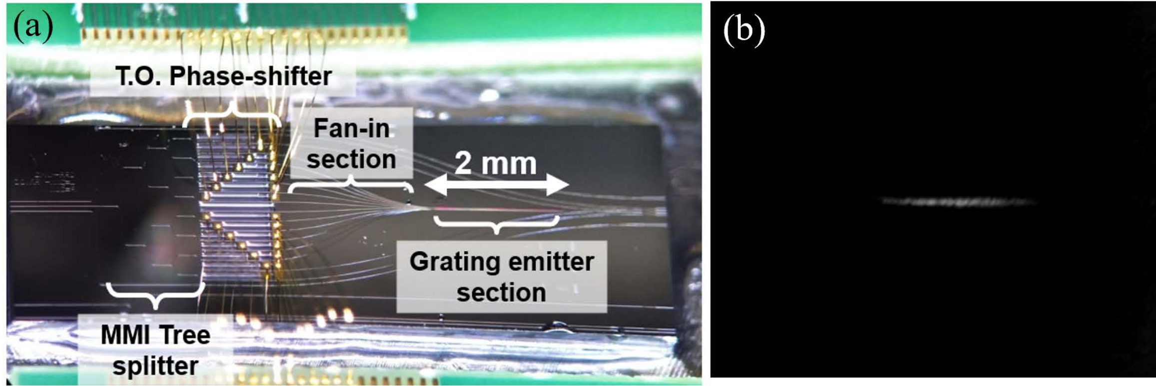

Figure 3.20. (a) Microscope image of the fully packaged 12-channel OPA device. (b) Measured near-field pattern for the emission from the SiN_x grating.

the linear fitting is found to be 1.6±0.7 dB/cm at the spectral range of 4.55-4.60 μm. The performance of the thermo-optic phase shifter was evaluated using a Mach Zehnder interferometer (MZI), and we found the power of 104±14 mW can achieve a 2π phase shift. After the light is coupled into the waveguide, the grating emitter demonstrated a uniform emitting in the near-field pattern, as shown in Figure 3.20(b).

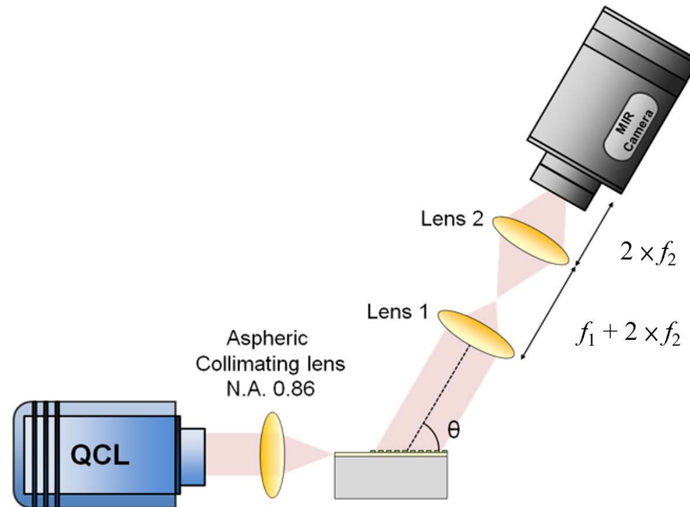

Figure 3.21. Schematic of far-field measurement setup used to characterize the OPA device.

Figure 3.21 shows the schematic of far-field measurement setup for the beam-steering experiment. An aspheric lens with $NA = 0.86$ was used to couple the light into the waveguide in the device, and a lens tube with two lenses, fixed onto an FLIR A6700sc

MIR camera, was tilted at about 45° in the vertical plane to collect the light emitted from the grating array. The angle value of beam steering was calibrated by using a rotating mirror to reproduce the beam steering with a known angle.

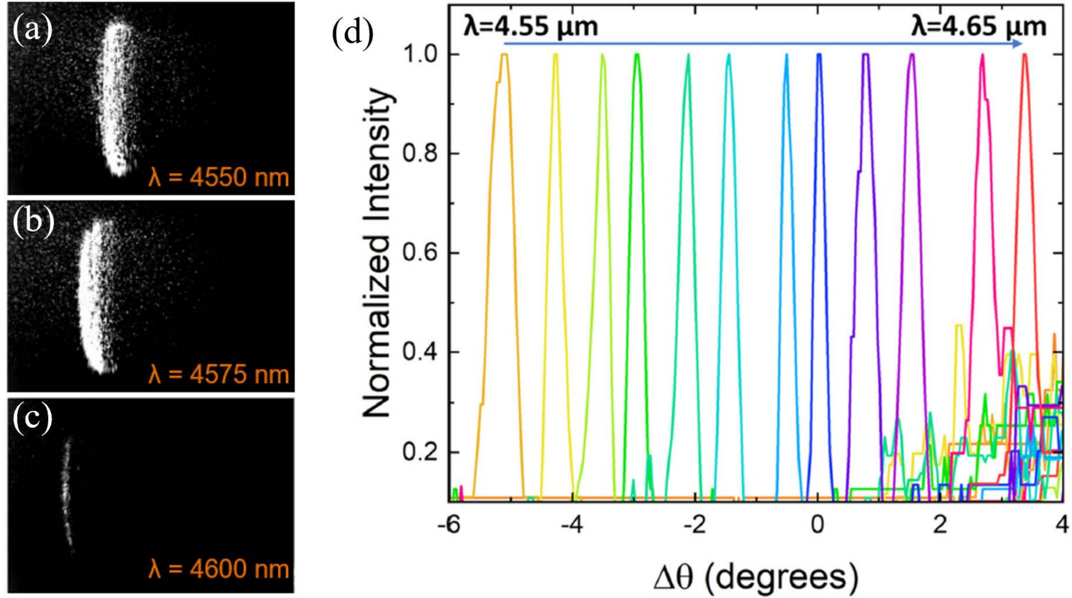

Figure 3.22. (a-c) Measured far-field patterns for λ = 4550 nm, 4575 nm, and 4600 nm, respectively. (d) Measured normalized far-field intensity profile along the θ-axis for different wavelengths.

The far-field patterns presented in Figure 3.22 demonstrate longitudinal beam steering along the θ-axis as the wavelength is tuned from 4500 nm to 4600 nm. The steering angle tunability versus the wavelength was calculated by linear fitting and found to be 0.069°/nm. Note that the inherent optical path length and the process non-uniformity for the waveguides will induce a phase error in the grating array and distort the far-field pattern for the beam steering. Therefore, an algorithm was implemented to optimize the phase tuning of phase shifters to eliminate the peaks on the background and obtain lower IFOV (smaller beam size), as shown in Figure 3.23(a). After the phase error correction, the 3 dB beam width divergence in longitudinal axis ϕ and perpendicular axis θ were measured to be 2.9° and 0.5°, respectively. In Figure 3.23(b), we achieve 2D beam steering by wavelength tuning and phase-shifter tuning. Here, the wavelength is scanned from 4580 nm to 4620 nm while the phase can be adjusted to make the beam point to any angle.

In the longitudinal direction, the range of beam steering can be up to 12.7° with beam divergence of 0.47°×2.86°.

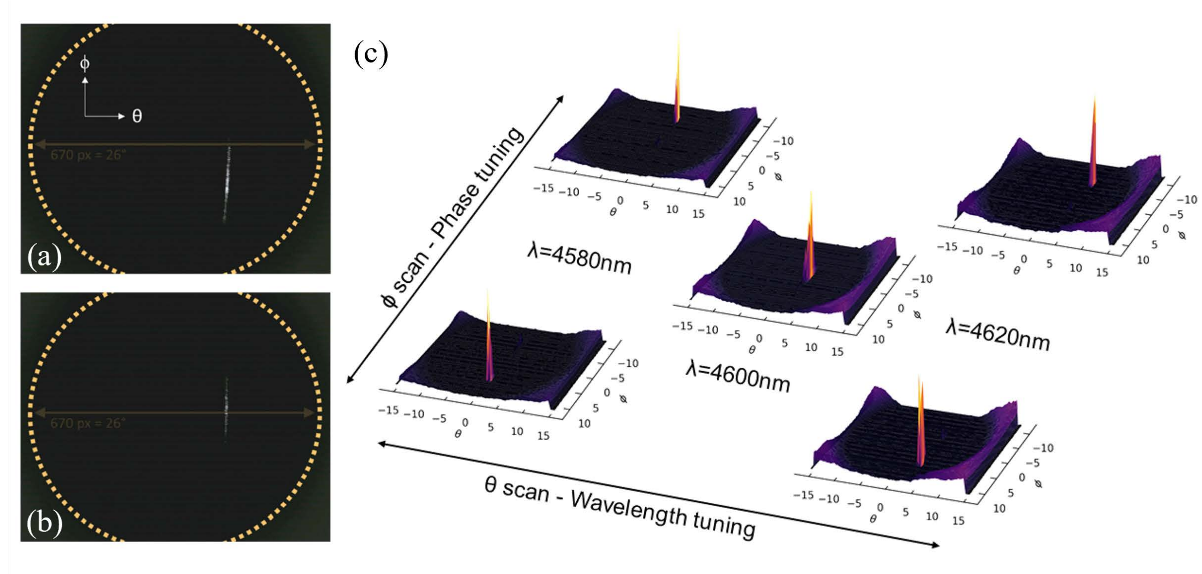

Figure 3.23. Measured far-field patterns (a) before and (b) after phase-error correction, respectively. (c) Three-dimensional plots for the measured far-field patterns while phase and input wavelength are tuned simultaneously.

3.3.3 Optimization for performance of grating emitters

To enhance both performance and stability of the grating structure, we proposed a custom 60 nm shallow-etched grating on a 2 μm-thick Ge layer as the waveguide with Si_3N_4 cladding. Figure 3.24(a) shows the schematic of the custom grating structure. The width of the Ge waveguide is 2 μm throughout the grating to maintain weak emission. On top of the Ge layer, the etched Ge grating employs various widths and duty cycles, to balance the power emission rate and to increase the effective coupling length. The period λ of the grating is 1308 nm. The incident angle θ_i is 90°. The output medium is air whose refractive index value n_O equals 1.0. According to Equation (3.5), the corresponding center output angle is 15° at 4600 nm wavelength (λ) when $m = 1$, where n_i is the effective refractive index of the grating.

$$n_o \sin\theta_o = n_i \sin\theta_i - m\frac{\lambda}{\Lambda} \tag{3.5}$$

The propagation constant of the grating structure depends on the width of the etched

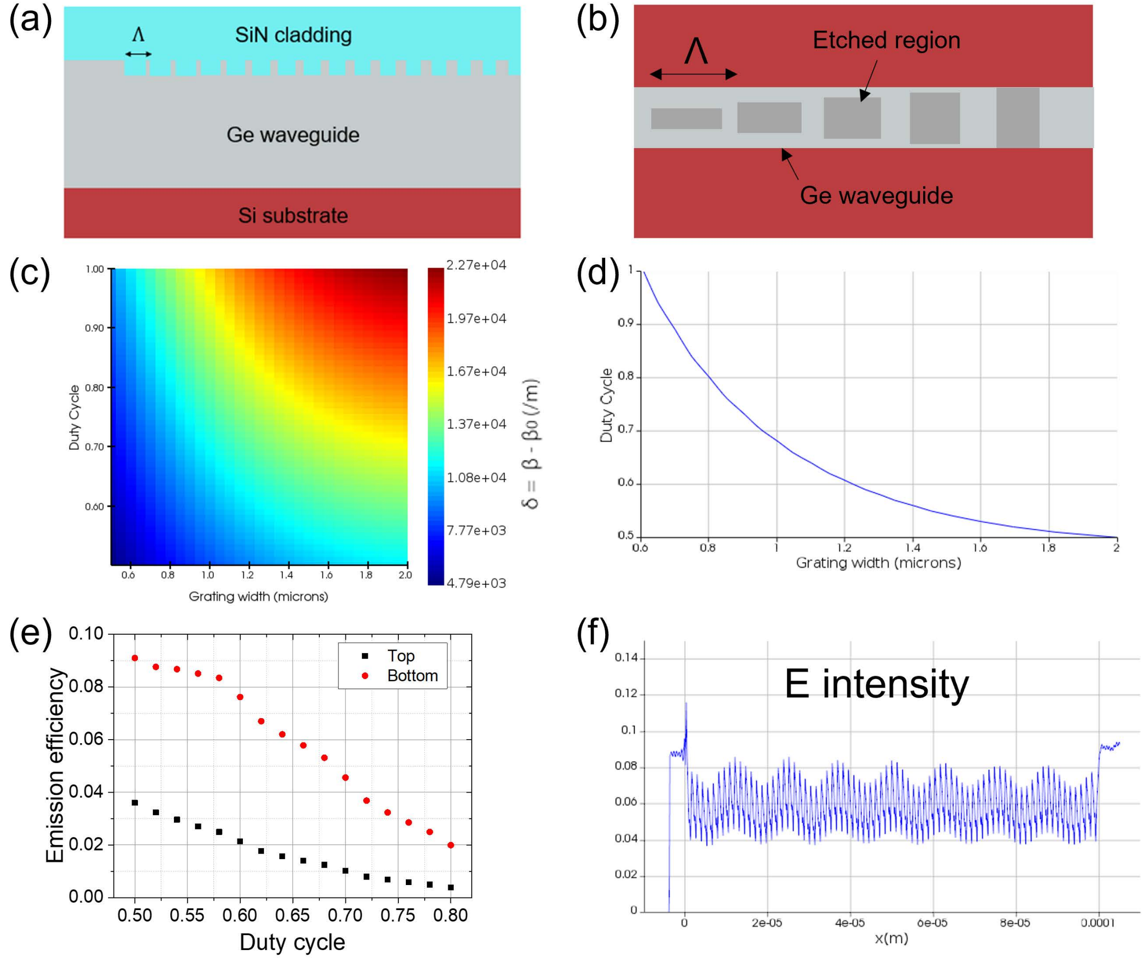

Figure 3.24. (a) The cross section and (b) the schematic of the proposed Ge etched grating with custom duty cycle and width. (c) The contour map of the δ values, where $\delta = \beta - \beta_0$, $\beta_0 = 5.16 \times 10^6$/m, and β is the propagation constant for the etched Ge grating with varying duty cycle and width; (d) the simulated combinations of duty cycle and width for the custom grating design. (e) The simulation of emission efficiency for the 100 μm long custom grating for top emission (black) and bottom scattering (red); (f) the simulation of intensity distribution launching from $x = 0$ μm for top emission.

Ge pattern and the duty cycle. To maintain the uniform propagation constant, the etched Ge pattern employs larger duty cycle with smaller width at the input end, 0.5 duty cycle with 2 μm width at the output end as depicted in Figure 3.24(b), and continuous transition in between the two ends. Figure 3.24(c) illustrates the simulated contour map of the δ values, where $\delta = \beta - \beta_0$, $\beta_0 = 5.16 \times 10^6$/m, and β is the propagation constant for the etched Ge grating with varying duty cycle and width. When the duty cycle or δ value

equals to 0, the propagation constant in the grating equals to that in the Ge waveguide. Figure 3.24(d) shows the designed duty cycles and width values for the custom grating with maintaining uniform propagation constant. The simulation tool is Lumerical MODE solution.

Figure 3.24(e) illustrates the simulated emission rate of the custom grating with varying duty cycles, where the black squares and red circles indicate top and bottom emission, respectively. The emission to the top is smaller than that to the bottom, which limits the emission efficiency to be less than 0.5. Figure 3.24(f) shows the simulation of the top emission intensity distribution assuming the input power is 1 mW. In the custom grating design, the duty cycles and width values were 0.70 and 0.97 μm at the input end, and 0.52 and 1.72 μm at the output end. The corresponding emission rate values were 1.0×10^{-4} μm^{-1} and 3.7×10^{-4} μm^{-1}, respectively. In between the two ends, the emission rate increases continuously while remaining the uniform propagation constant.

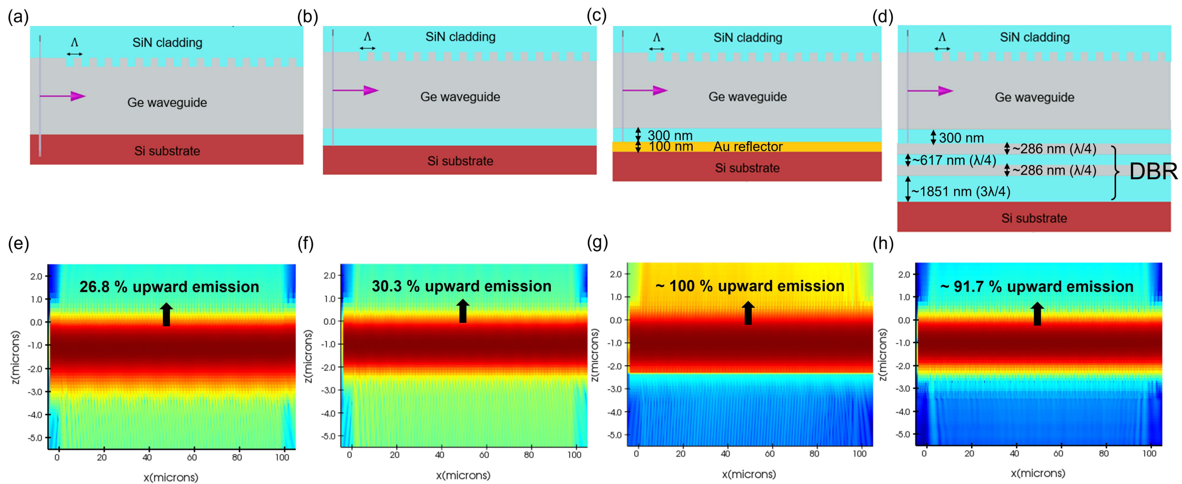

Figure 3.25. (a) Schematic of a regular grating structure. To improve the upward emission efficiency, the grating structure can be integrated with (b) a 300 nm thick Si_3N_4 layer, (c) a metal layer, or (d) a DBR underneath the grating structure. (e)-(h) Corresponding simulated grating emission profile in log scale.

To improve the upward emission efficiency for the grating emitter, we can collect the bottom emission light by integrating a reflective mirror underneath the grating, such as metal layers or distributed Bragg reflectors (DBRs). In Figure 3.25(a) and (e), the original design has only around 26.8 % upward emission. If we put a 300 nm thick Si_3N_4

layer underneath the Ge layer to increase the index contrast, the upward emission can be slightly increased to 30.3 % as shown in Figure 3.25(b) and (f). In Figure 3.25(c) and (g), a metal layer under the grating structure can boost the upward emission to almost 100 %, but the deposition of metal layers between the Si substrate and the Ge layer would be very challenging in terms of the fabrication. With 2 pairs of a-Si/Si_3N_4 DBRs as illustrated in Figure 3.25(d), the upward emission can be optimized to 91.7 %.

3.3.4 Design of 45-degree reflectors using focused-ion-beam etching

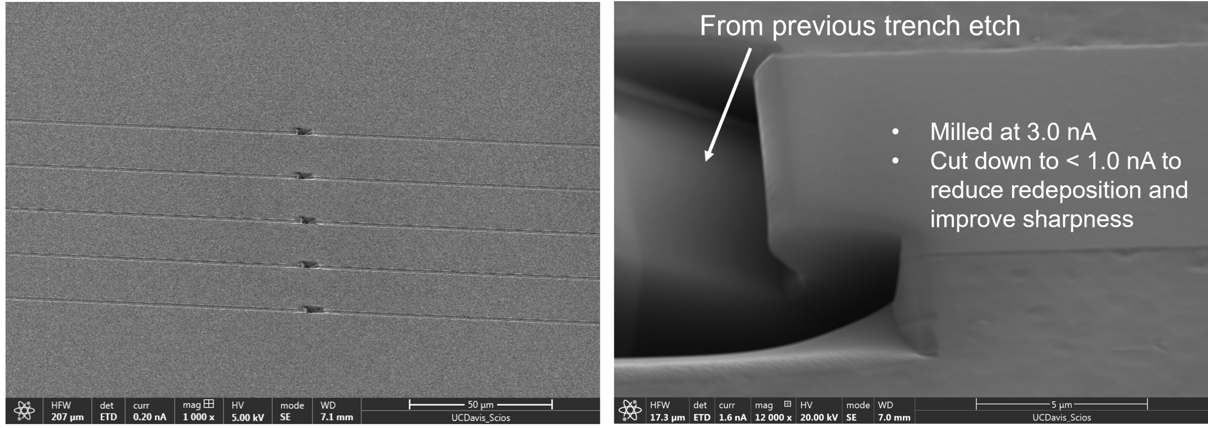

Figure 3.26. 45 degree reflectors etched by focused-ion-beam etching on Ge on Si waveguides.

While the fabrication of 45° mirrors is still underway, we have developed another simpler fabrication process to demonstrate a 3D photonic-electronic phase array (3D PEPA) as shown in Figure 3.26. In this process, small ladder shape reflectors are fabricated by 45° focused ion beam (FIB) etching, and then vertical vias are fabricated before the reflectors to guide the reflected wave.

Figure 3.27(a-c) illustrates the schematic of a Ge single layer waveguide array on Si substrate based on FIB etching. Here, a notch structure with 45° angle is utilized to feed the light into a via structure on the top. In the simulation, a transverse magnetic (TM) polarized 4.6 μm light source was applied to characterize the optical properties of the designed structure. In the following discussion, we simulated a row of vertical emitters to check the global behavior of the system as shown in Figure 3.27(d). For

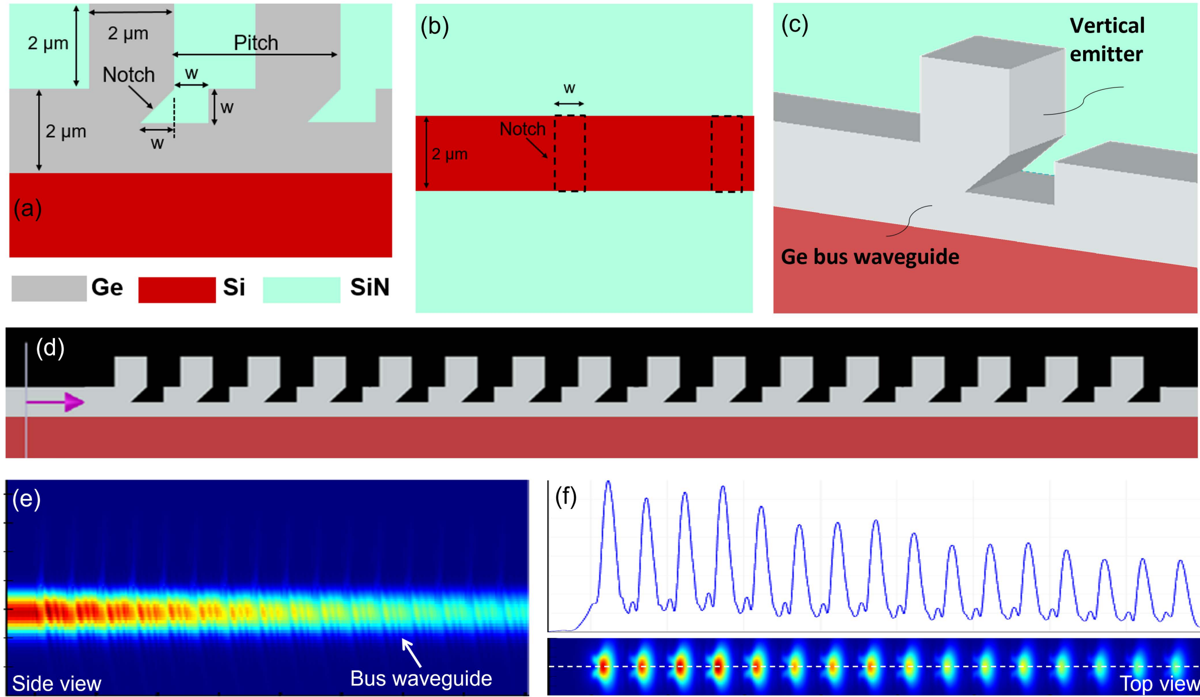

Figure 3.27. (a) Side view, (b) top view, and (c) perspective view of the proposed single layer waveguide array. (d) Layout of 16 emitters in the simulation and the corresponding (e) side view and (f) top view of the simulated field intensity distribution for the whole power-feeding network system.

a decent simulation time, we limited the number of elements to 16. After considering the arrangement for the phase control circuit and the fabrication constraints, we set the pitch for the single waveguide array to 10 μm and the notch width to 200 nm. A 2 μm via length was chosen as the same as the previous design. Figure 3.27(e) and (f) show the simulated results for the field intensity distribution on the top and side of the single waveguide array, respectively. The observed upward and downward emitting efficiency are 7.89 % and 34.15 % respectively due to the low index contrast between the Si substrate and Ge waveguide. The uniformity of the emission distribution can be further optimized by varying the notch width along the waveguide array.

3.3.5 Light grating emitters for long-wave infrared

Having covered the discussion on 2D and 3D PEPAs in MWIR in the previous section, we will now shift our focus to investigating the 2D PEPA in long-wave infrared (LWIR) in the subsequent part. Building upon our previous waveguide design, which employed a

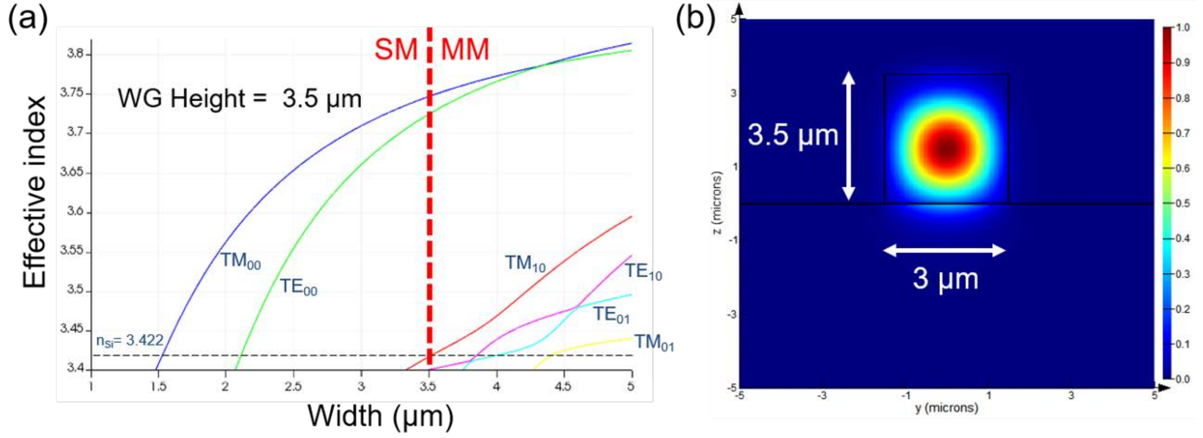

Figure 3.28. (a) Variation of calculated effective index with waveguide width when waveguide height is 3.5 μm. (b) Simulated TM mode profile at $\lambda = 8.25$ μm.

2×2 μm^2 dimension for 4.6 μm wavelength, we have opted for a thicker waveguide height of 3.5 μm to ensure effective confinement at 8.25 μm wavelength. In Figure 3.28(a), we calculated the effective indices for all the supported modes while the waveguide height is 3.5 μm and the waveguide width is varied from 1 μm to 5 μm. The result indicates that TM polarized single mode operation can be satisfied when the waveguide width is smaller than 3.5 μm. Therefore, 3×3.5 μm^2 was selected to be the waveguide size for 8.25 μm wavelength. Figure 3.28(b) shows the simulated profile for the TM mode. As the mode is strongly confined inside the Ge core due to the high contrast index, the choice of the cladding has a minor effect on the waveguide properties. Besides, we verified that the minimum bending radius value of 50 μm would guarantee negligible excess optical losses (<0.1 dB/90°) due to bending, thanks to the relatively strong optical mode confinement in the waveguide.

In our previous work, we have developed the MMI structured beam-splitter for the integration of MWIR QCL and our Ge waveguides designed for 4.6 μm wavelength. Similarly, to feed the light from 8 outputs of 8.25 μm LWIR QCL to the 128 bus Ge waveguides, we developed another 8×16 beam splitter for it. It is based on cascaded MMI Tree. Due to the void defect which may happen in the gap between the two output tapered waveguides, we take the size of gap into consideration in our design. In Figure 3.29, we designed MMI for 3 dB splitting at the 8.25 μm wavelength. Here are two different designs presented

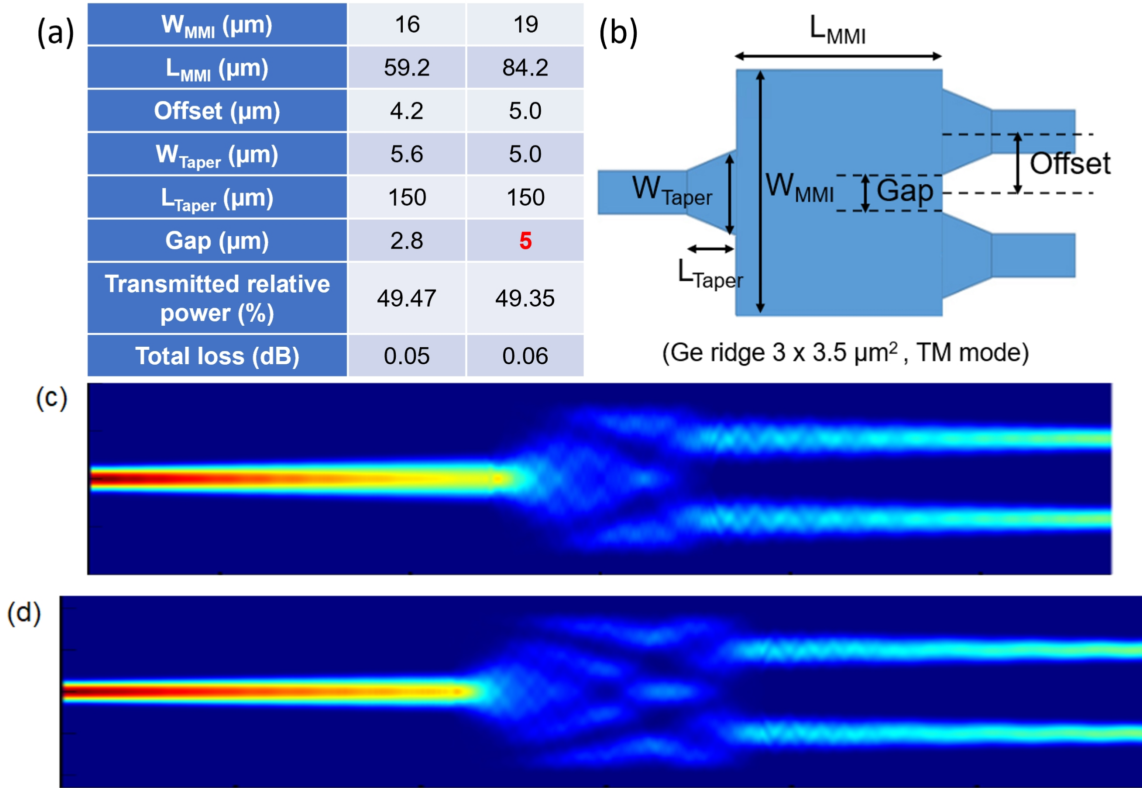

W_{MMI} (μm)	16	19
L_{MMI} (μm)	59.2	84.2
Offset (μm)	4.2	5.0
W_{Taper} (μm)	5.6	5.0
L_{Taper} (μm)	150	150
Gap (μm)	2.8	5
Transmitted relative power (%)	49.47	49.35
Total loss (dB)	0.05	0.06

Figure 3.29. (a) MMI design parameter table for 3×3.5 μm^2 ridge waveguide platform at 8.25 μm wavelength. (b) Schematic of an MMI structure. Beam propagation simulation of MMI 3 dB power splitting for (c) $W_{MMI} = 16$ μm and (d) $W_{MMI} = 19$ μm.

to accommodate process fabrication variation. Larger gap is the priority, but a trade-off will be made for a compact design to allow tight integration.

Next, we design and simulate a beam steering device using grating emitters in LWIR for a proof-of-concept. It will help us have a better understanding of a LWIR photonic platform and beam-steering characterization experiments as it is easier to fulfill this fabrication. First of all, we chose CaF_2 as the cladding material thanks to the low material absorption in LWIR and it is also doable for the deposition as a cladding to have more space for multilayer integration and metal crossing above the waveguides. In Figure 3.30(a), staircase-shaped grating with 2-mm length was chosen due to its stronger upward coupler strength and weaker substrate leakage. In Figure 3.30(b-e), we evaluate the performance of this grating under 100-μm-total length and confirm the optimized etching depth for this two-step grating structure. The simulated results indicate that the grating emitter

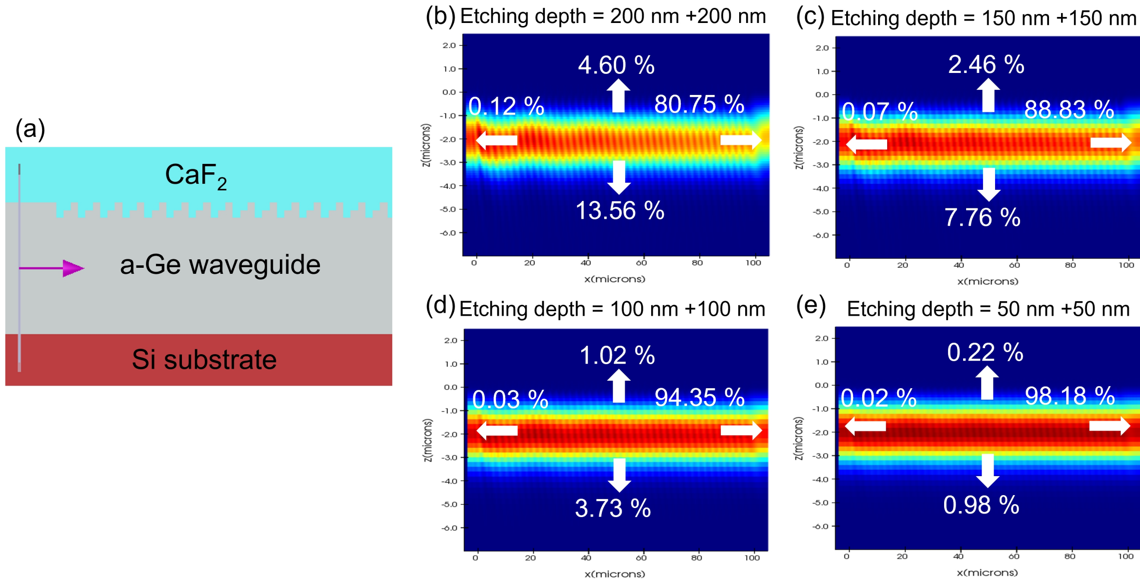

Figure 3.30. (a) Schematic of a staircase-shaped germanium grating emitter. (b) Side view of the simulated power distribution for a 100 μm long grating emitter with the total etching depth of (b) 400 nm, (c) 300 nm, (d) 200 nm, and (e) 100 nm.

would have a smoother emitting profile when the etching depth for each step is around 100 - 150 nm. Furthermore, we can utilize the proportional relationship to calculate the power emitting in each direction after 2 mm propagation. For the grating emitter with 300 nm total etching depth, we can obtain 22 % and 69 % for the upward and downward emitting efficiency, respectively. The period of this grating is set to 2399 nm to have a diffraction angle around 15° calculated by grating equation.

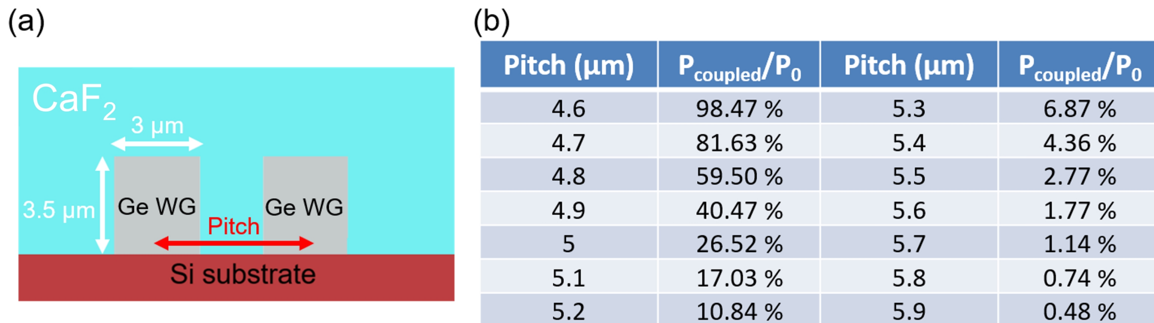

Pitch (µm)	$P_{coupled}/P_0$	Pitch (µm)	$P_{coupled}/P_0$
4.6	98.47 %	5.3	6.87 %
4.7	81.63 %	5.4	4.36 %
4.8	59.50 %	5.5	2.77 %
4.9	40.47 %	5.6	1.77 %
5	26.52 %	5.7	1.14 %
5.1	17.03 %	5.8	0.74 %
5.2	10.84 %	5.9	0.48 %

Figure 3.31. (a) Cross-sections of two germanium waveguides on a silicon substrate with CaF_2 cladding. (b) The corresponding calculated crosstalk ratio with varying pitch

To achieve sidelobe-free beam steering, the separation of emitters should be smaller

than a half wavelength. However, once the waveguides get too close, the crosstalk coupling between them will become significant and the phase control for each emitter will be challenging. Figure 3.31 shows the crosstalk ratio between the two adjacent germanium waveguides with varying pitch as defined in the schematic. The result indicates that the crosstalk becomes more negligible as the pitch increases to 5.4 μm.

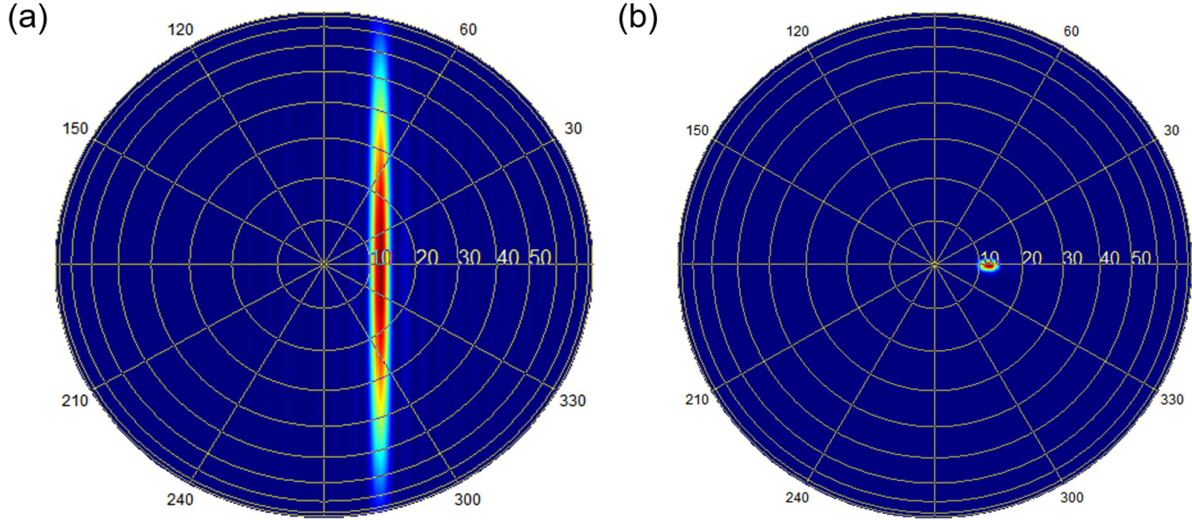

Figure 3.32. Simulated far field patterns for (a) single grating emitter and (b) 24 channels grating emitter with pitch = 5.4 μm at the wavelength 8.25 μm

Previous MWIR emitter grating design suffered from an emission angle close to 45° at the center wavelength, which made the experimental work complex. For this LWIR grating emitter, we revised the grating design to bring the angle close to 15° from the normal of the chip at the center wavelength 8.25 μm. Figure 3.32 shows the far field patterns for a single grating emitter and a 24-channel grating emitter with the pitch of 5.4 μm, respectively.

3.3.6 Summary

To our knowledge, this is the first demonstration of 2D beam steering in MWIR using a germanium-silicon photonic platform. We have successfully presented a fully packaged non-mechanical beam-steering device featuring a 2-mm-long 12-channel grating emitter array. This achievement has led to a remarkable reduction in beam divergence, down to 0.18° in the perpendicular direction, with wavelength tunability of 0.069°/nm. In the

lateral direction, we have demonstrated a substantial beam-steering angle of 12.7° with beam divergence of $0.47° \times 2.86°$. To further enhance the performance of the grating emitters, we can tailor the grating structures to create a uniform emitting profile and introduce reflectors beneath the emitters to increase emitting efficiency. Moreover, the same approach can be adopted to design LWIR beam steering devices.

3.4 Foundry-compatible two-dimensional optical phase array

During the COVID-19 shutdown, we leveraged commercial foundries to design and fabricate PEPA devices for the beam steering demonstration. In order to comply with the design rules of commercial foundries, we changed the vertical column Ge emitters to lateral Ge emitters with vertical emission. The vertical emission can be achieved by the 45 degree reflectors fabricated using focused ion beam (FIB) etching as described in Figure 3.26. Moreover, commercial foundries can allow the silicon layer to be doped by n-type and p-type dopants to create bipolar n-p-n transistors. These transistors can form active matrix and deliver current to the germanium waveguides for thermo-optical tuning. In the forthcoming discussion, we present the proposed schematic of a lateral PEPA array that can be implemented through AIM Photonics. The optimization process began with an investigation into the propagation loss and bending loss of the emitter structure, considering various waveguide widths and bending radii. To ensure a uniform emitting profile, the coupler efficiency was calculated by varying the coupler length, and the corresponding lengths were subsequently incorporated into the layout of the lateral PEPA arrays. Following the fabrication of the PEPA devices by AIM Photonics, they underwent additional packaging on printed circuit boards (PCBs) utilizing the wire bonding technique. Furthermore, a MWIR measurement setup was developed to thoroughly assess the optical properties of the designed structures.

In Figure 3.33(a), we propose a large-scale compact beam steering system consisting of 128×128 phased arrays based on a Ge-on-SOI platform. Here, a 45-degree reflector in each unit is utilized to emit the light upward. To achieve low instantaneous field of view

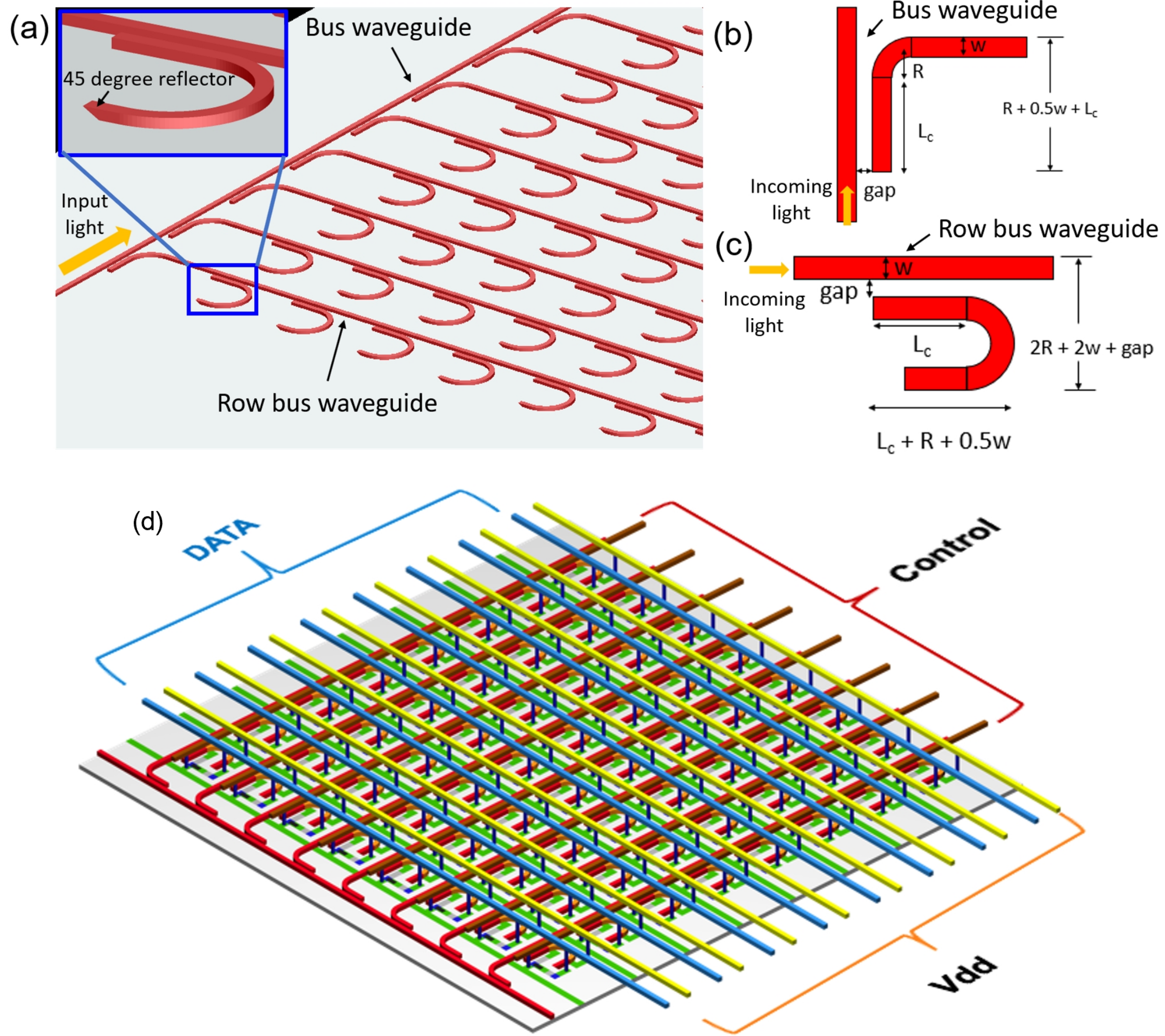

Figure 3.33. (a) Schematic for a 128 × 128 phased arrays based on a Ge-on-SOI platform. (b) Schematic for the bus-to-row coupling. (c) Schematic for the row-to-unit coupling. (d) 3D schematic of the optical phase array including transistors, CONTROL, DATA, and Vdd lines.

(IFOV) for beam steering, it is important to have uniform emission intensity across all the reflectors by properly varying the coupling strengths of each coupling region. Therefore, in the following discussion, we will investigate how to equally split the power into each row bus waveguide and each unit by modulating the bus-to-row coupling efficiency and the row-to-unit coupling efficiency as the schematics shown in Figure 3.33(b) and (c), respectively. Due to the considerable absorption loss of SiO_2 cladding at LWIR and 800 nm thick Ge layer, 3.8 μm and 4.6 μm were selected for the designed wavelengths of

foundry-compatible lateral-PEPA devices.

3.4.1 3.8 μm lateral-PEPA design with AIM Photonics compatibility

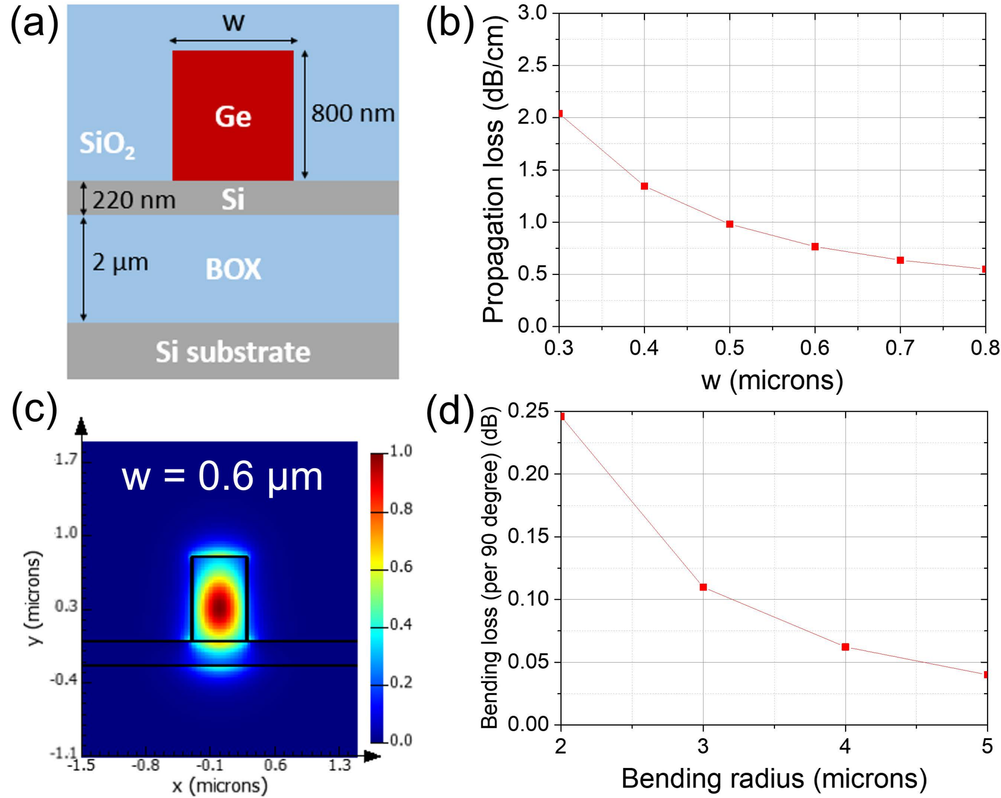

Figure 3.34. (a) Schematic for the proposed guiding structure at 3.8 μm wavelength based on a Ge-on-SOI platform. (b) Calculated propagation loss for the fundamental TM mode when the waveguide width is varied from 0.3 μm to 0.8 μm. (c) Simulated TM mode profile for the waveguide width of 0.6 μm. (d) Calculated bending loss for the bending radius varied from 2 μm to 5 μm.

According to AIM PDK, the guiding structure is a ridge waveguide based on a Ge-on-SOI platform as shown in Figure 3.34(a). The Ge waveguide height is 800 nm, while the Si layer and the buried oxide (BOX) layer are 220 nm and 2 μm in thickness, respectively. In Figure 3.34(b), we calculated the propagation loss for the fundamental transverse magnetic (TM) mode when the Ge waveguide width is varied from 0.3 μm to 0.8 μm. In order to ensure a good optical confinement and low propagation loss, 0.6 μm was selected

to be the waveguide width for 3.8 μm and the corresponding simulated mode profile is shown in Figure 3.34(c). Besides, we verified that the bending radius value of 2 μm would guarantee negligible excess optical losses thanks to the relatively strong optical mode confinement in the Ge waveguide.

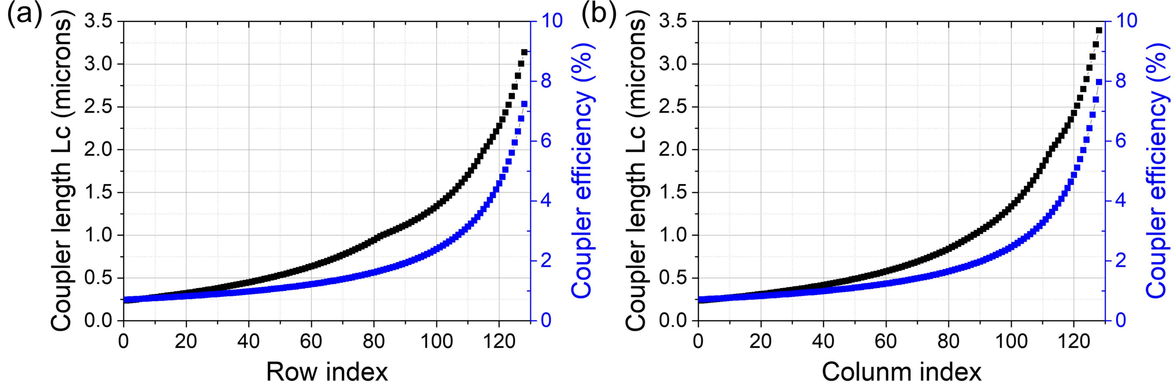

Figure 3.35. The coupling length (Black) and the simulated coupler efficiency (Blue) for (a) the bus-to-row couplers and (b) the row-to-unit couplers in the 128×128 phased array for 3.8 μm wavelength.

In Figure 3.35(a), the bus-to-row coupler length is varied from 0.24 μm in the first coupler to 3.14 μm in the last coupler with a constant gap of 500 nm, corresponding to the coupling efficiency of 0.71 % and 7.25 %, respectively. The bending radius was set to 2 μm according to the previous investigation for the bending loss. Similarly, the length of the row-to-unit coupler is varied from 0.24 μm (coupling efficiency = 0.72 %) to 3.40 μm (coupling efficiency = 7.98 %) as shown in Figure 3.35(b). In order to design a unit to be as compact as possible, we lower the required maximum coupling efficiency to reduce the maximum coupler length, which causes power loss of 9.1 % in the end of the bus waveguide and 8.3 % in the end of the row bus waveguides. Consequently, we can achieve the pixel size of 7 μm $\times$ 7 μm.

3.4.2 4.6 μm lateral-PEPA design with AIM Photonics compatibility

In Figure 3.36(a), we present another waveguide design for 4.6 μm wavelength without SiO_2 top-cladding because SiO_2 has higher loss at 4.6 μm than that at 3.8 μm. Similarly, the thickness of each layer is the same as described in the design for 3.8 μm wavelength.

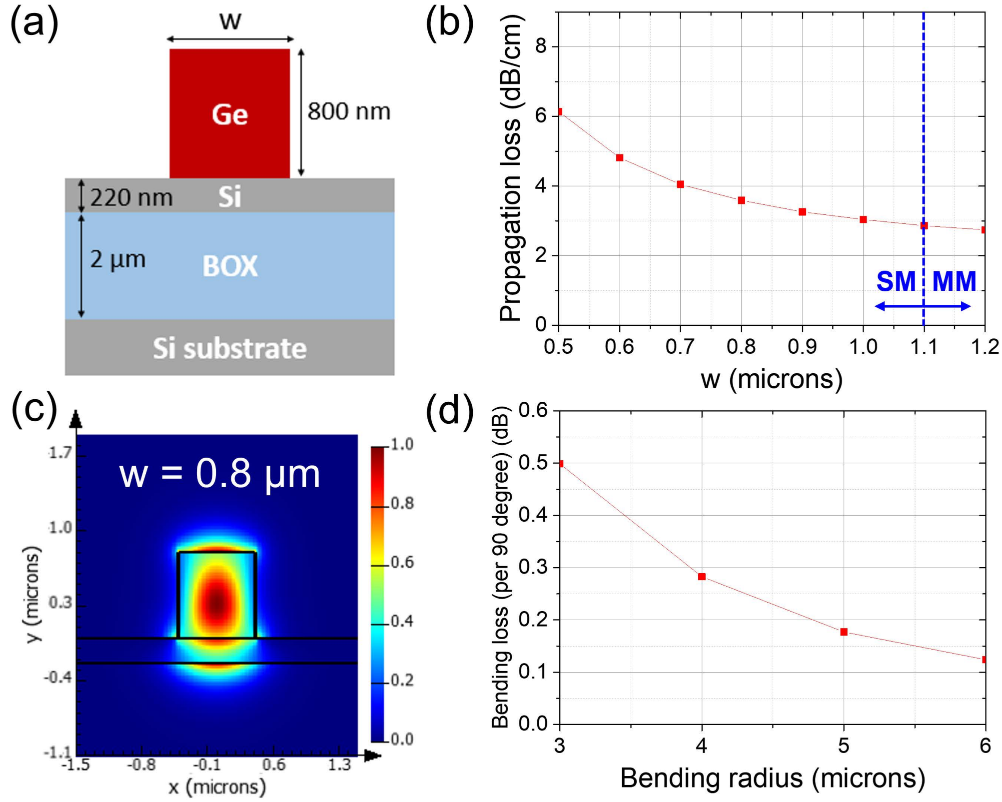

Figure 3.36. (a) Schematic for the proposed guiding structure at 4.6 μm wavelength based on a Ge-on-SOI platform. (b) Calculated propagation loss for the fundamental TM mode when the waveguide width is varied from 0.5 μm to 1.2 μm. (c) Simulated TM mode profile for the waveguide width of 0.8 μm. (d) Calculated bending loss for the bending radius varied from 3 μm to 6 μm.

In Figure 3.36(b), we investigated the propagation loss for the fundamental TM mode in the Ge ridge waveguide, and found the single mode operation can be satisfied when the waveguide width is smaller than 1.1 μm. In order to ensure a good optical confinement and low propagation loss, 0.8 μm was selected to be the waveguide width for 4.6 μm and the corresponding simulated mode profile is shown in Figure 3.36(c). To guarantee a negligible bending loss, we calculated the bending loss with varying the bending radius from 3 μm to 6 μm in Figure 3.36(d), and the bending radius value of 4 μm was chosen to be used in the 128×128 phased array for 4.6 μm wavelength.

As we described in the previous paragraph about how to design large-scale phased arrays with uniform emission intensity, we vary the coupler lengths for the bus-to-row

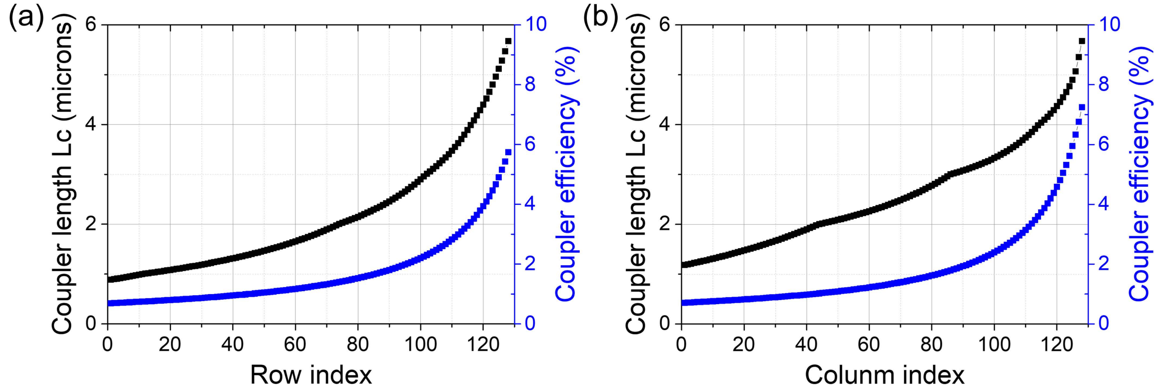

Figure 3.37. The coupling length (Black) and the simulated coupler efficiency (Blue) for (a) the bus-to-row couplers and (b) the row-to-unit couplers in the 128×128 phased array for 4.6 μm wavelength.

couplers and the row-to-unit couplers in the design for 4.6 μm wavelength as shown in Figure 3.37. The coupler gap was set to 750 nm to have a suitable coupling strength between Ge waveguides. The bus-to-row coupler length is varied from 0.89 μm (coupling efficiency = 0.69 %) to 5.67 μm (coupling efficiency = 5.74 %) and the row-to-unit coupler length is varied from 1.18 μm (coupling efficiency = 0.71 %) to 5.68 μm (coupling efficiency = 7.25 %) to have a uniform emission across all the reflectors. Due to the low maximum coupling efficiency, the power loss in the end of the bus waveguide and the row bus waveguide are expected to be 11.4 % and 9.1 %, respectively. With the compact design of each unit, we can achieve the pixel size of 11 μm $\times$ 11 μm.

3.4.3 Layouts and packaging

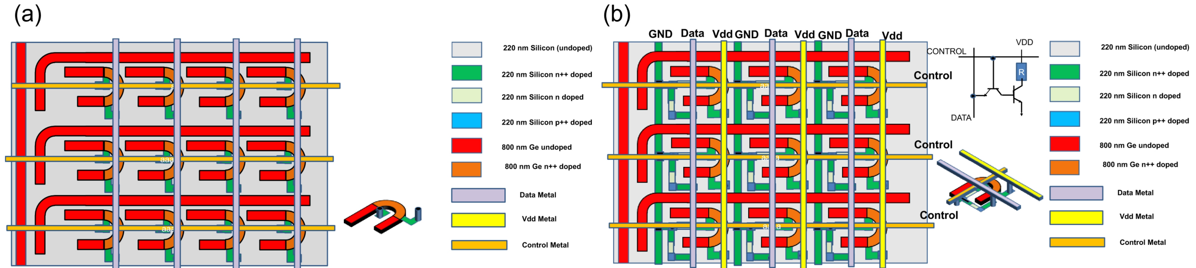

Figure 3.38. Schematic diagram of 128×128 PEPA array based on AIM PDK (a) without transistors and (b) with transistors.

Figure 3.38 depicts the schematic diagrams of two types of PEPA arrays: one with-

out transistors and another with transistors based on AIM PDK. In the design without transistors, we employed the bending region of each emitter unit as a heating element as illustrated in Figure 3.38(a). Specifically, the two ends of the bending waveguide were connected to metal vias through heavily doped Si regions. These metal vias were then linked to the metal lines designated for Control and DATA. As for the other PEPA version with transistors, the bending region of each emitter unit was also employed as a heating element. Initially, one end of the bending waveguide was connected to the Vdd metal line through a heavily doped Si region and a metal via. Subsequently, the other end was connected to a customized doped Si structure that functions as transistors, as depicted in Figure 3.38(b). Finally, the two ends of the Si doped structures were connected to metal vias, which were in turn connected to separate metal lines designated for Control and DATA.

After we completed the designs of the emitters and heating elements, we proceeded to create layouts for lateral-PEPAs in various configurations, including 16×16, 32×32, and 64×64 lateral-PEPAs, both with and without transistors as illustrated in Figure 3.39(a-c). The pitch of the emitter units is 7 μm for 3.8 μm wavelength, and 11 μm for 4.6 μm wavelength. To mitigate reflection and scattering, the ends of the bus waveguides and row bus waveguides are connected to 100 μm long tapers. The overall dimensions of the 64×64 lateral-PEPAs for 4.6 μm wavelength are 1657 μm×1675 μm with transistors and 1594 μm×1350 μm without transistors, respectively. In Figure 3.39(d-f), a 64×64 lateral-PEPA for 4.6 μm wavelength with transistors is packaged on a printed circuit board (PCB) using the wire bonding technique as shown in . Initially, the PEPA device was bonded onto a 5.5 mm×5.5 mm gold plate, which includes multiple holes to enhance heat dissipation. Subsequently, the bonding pads on both the PCB and the PEPA device were connected using gold wires. It is worth noting that the metal pads surrounding the PEPA device are very compact, with a width of 60.9 μm and a pitch of 70 μm. In order to prevent any potential interference between the input fiber and the bonding wires, we took care to position the input waveguide at a safe distance from the bonding pads. This arrangement minimizes the risk of collision and ensures uninterrupted fiber-to-waveguide

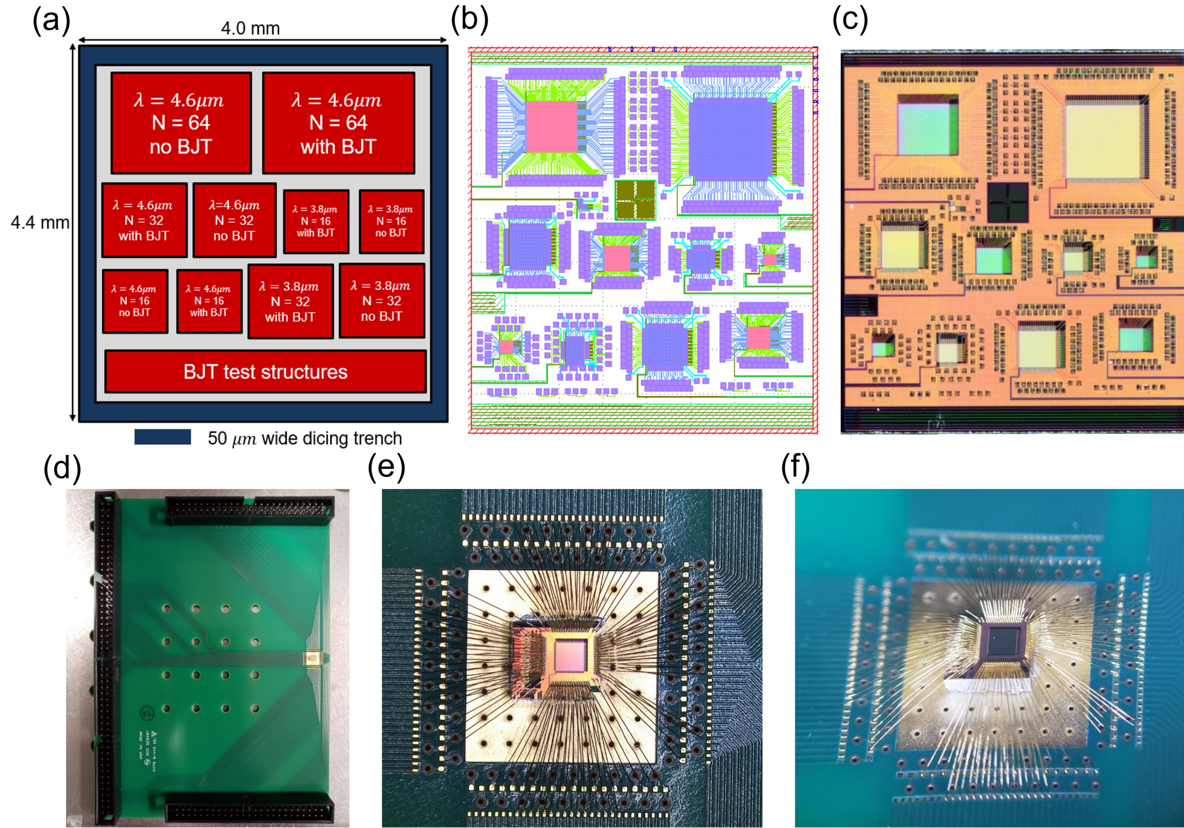

Figure 3.39. (a) Schematic diagram for PEPA arrays with different configurations. The corresponding GDS layout, and microscope image are shown in (b) and (c), respectively. Microscope images of the fully packaged 64 × 64 PEPA array with transistors are shown in (d-f) on different views.

coupling. The overall dimension of the PCB is 8.6 cm×14.4 cm, and multiple holes are placed in the center placed in the center to facilitate flexible mounting. Additionally, three rows of connectors are soldered on the side of the PCB to enable electrical control of the PEPA device.

3.4.4 Experimental setup and characterization

Figure 3.40 presents a comprehensive list of the key components utilized in the optical testing setup for conducting beam steering measurements. Considering that this is the initial characterization stage for the PEPA devices, and the SiO_2 cladding on the top has not been removed, we opted for a 1937 nm distributed-feedback (DFB) laser from Nanoplus and a 3250 nm interband cascade laser (ID3250HHLH) from Thorlabs. This

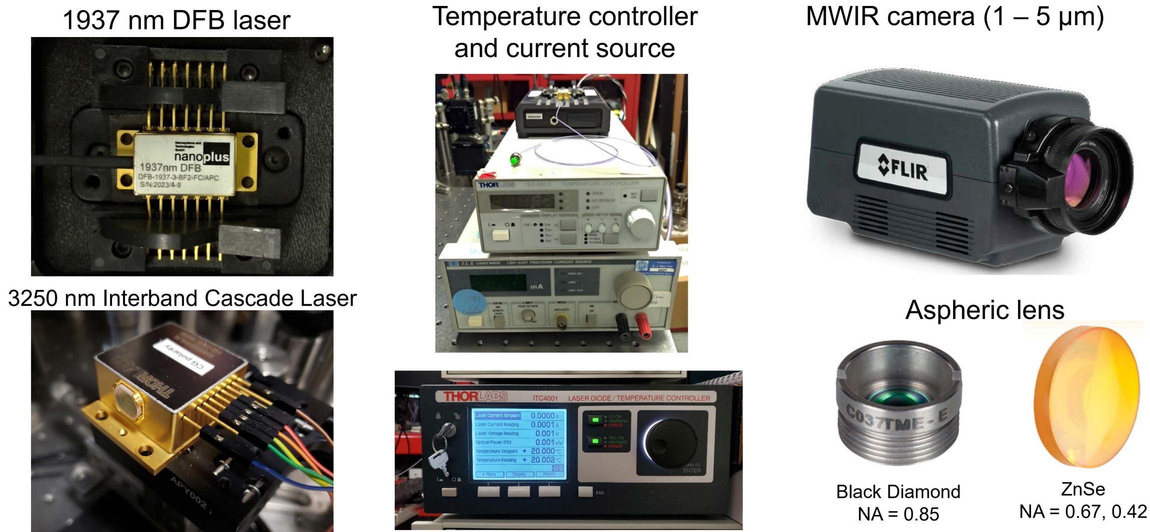

Figure 3.40. Pictures for the items used in the optical testing bench.

laser selection allows us to work around the high absorption loss typically associated with SiO_2 material in MWIR. Besides, we utilized Thorlabs' aspheric lenses fabricated from Black Diamond-2 (BD-2) and ZnSe materials for beam collimation and imaging purposes in MWIR. These lenses were specifically prepared to ensure efficient and accurate collimation of the beams as well as high-quality imaging capabilities. In terms of imaging, we utilized an A6700 MWIR camera manufactured by FLIR. This camera is capable of operating over a wide wavelength range from 1 μm to 5 μm with 15 μm detector pitch and a resolution of 640×512.

In order to maximize the efficiency of optical coupling, we explored two distinct strategies for coupling MWIR light into a Ge waveguide. These strategies involved the utilization of either a single mode fiber or a high-NA BD-2 aspheric lens, as illustrated in Figure 3.41. The former strategy offers easier alignment of the input light with the waveguides, but it results in higher edge coupling loss due to the mode mismatch between the fiber and the Ge waveguide. On the other hand, the latter strategy enables higher edge coupling efficiency by employing a high numerical aperture (NA) aspheric lens (NA = 0.85 in this study) while requiring additional effort in aligning the lenses for collimation and focusing along the light path. In terms of near-field imaging, a tube lens is positioned in front of the MWIR camera to project the near field of the PEPA device onto the sensor

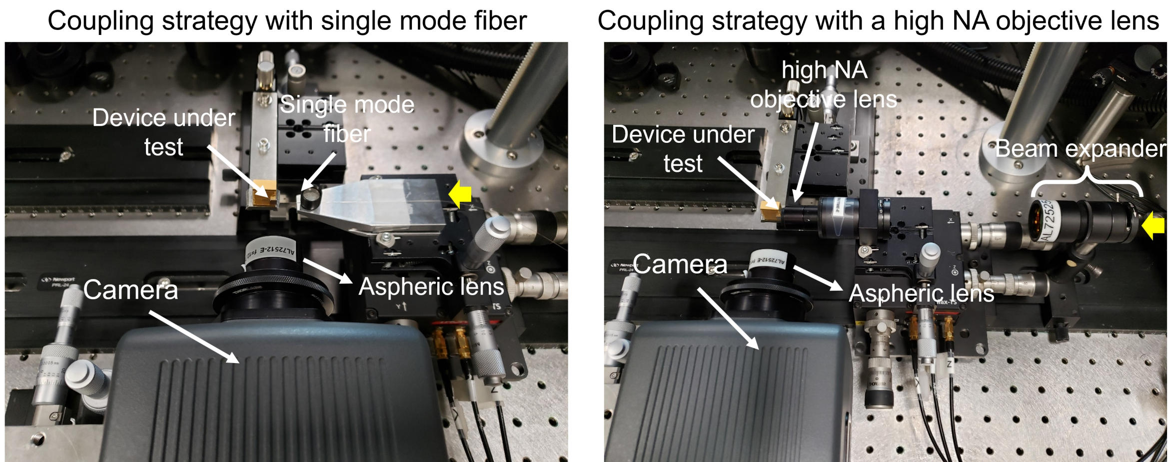

Figure 3.41. Different approaches for coupling light into a Ge waveguide using a single mode fiber and a high NA objective lens.

plane inside the MWIR camera.

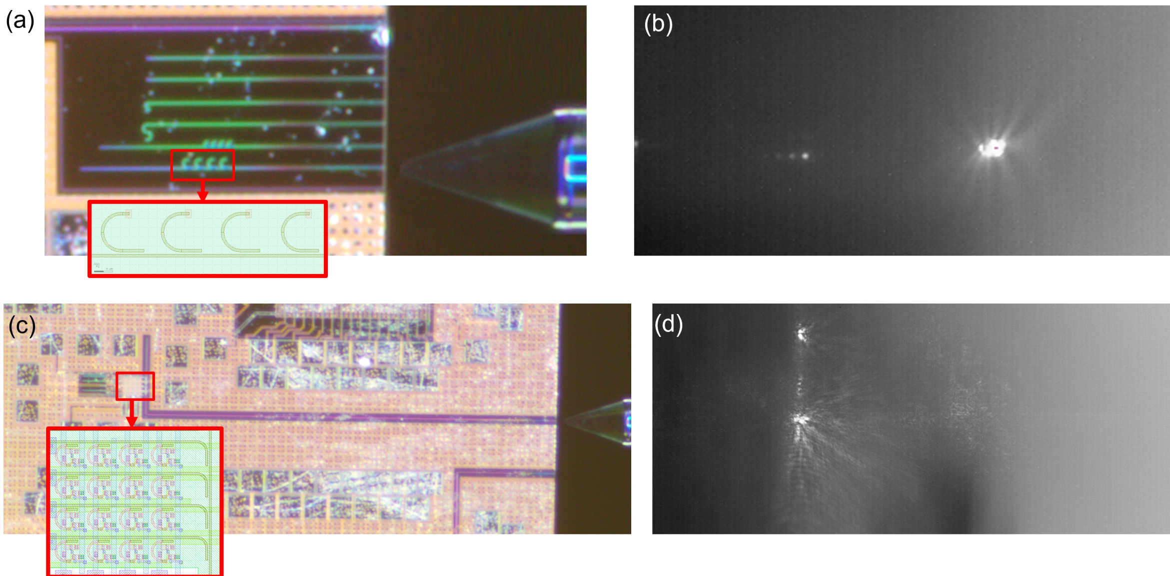

Figure 3.42. Microscope images and measured near fields for (a)-(b) a row of four emitters and (c)-(d) a 4×4 emitter array.

Since the fabrication process for the 45° reflectors was not fully developed at the time of these experiments, we began by characterizing a row of four emitters and a 4×4 emitter array as the initial demonstration, as depicted in Figure 3.42. Although the 45° reflectors were absent in these emitter units, we were still able to observe partial light scattered from the waveguide end of each emitter unit. Figure 3.42(a) displays the microscope image

of the row of four emitters along with their corresponding GDS layout. The measured near field exhibits four distinct light spots emitting from the top of the emitter units as shown in Figure 3.42(b). Since the coupler length for these four emitter units is identical, the intensity of the emitted spots gradually decreases along the propagation direction. The microscope image and the GDS layout of the 4×4 emitter array are presneted in Figure 3.42(c). However, it should be noted that due to the strong scattering light from the bending waveguide near the 4×4 emitter array, only a row of four light spots could be observed.

3.4.5 Summary

In this study, we successfully demonstrated beam steering devices compatible with foundry processes, utilizing 2D optical phased arrays operating at wavelengths of at 3.8 μm and 4.6 μm. We meticulously designed a 64×64 PEPA with integrated transistors based on a Ge-on-SOI platform. Subsequently, these devices were fabricated by a commercial foundry. Following fabrication, we performed comprehensive packaging of these arrays on printed circuit boards, employing the wire bonding technique. To evaluate their performance in beam steering, we conducted rigorous characterization using a MWIR optical testing bench. In future work, it is essential to further explore the propagation loss and bending loss of the Ge waveguides employed in the PEPA devices. By thoroughly investigating these factors, we can make significant advancements in optimizing the performance of the PEPA devices. Additionally, a significant aspect would be the complete development of the 45° reflectors, as it would enable the demonstration of a fully functional PEPA device.

Chapter 4

Highly-Dispersive Polarization-Diversifying Metalens for Hyperspectral Imaging

4.1 Compressive hyperspectral imaging

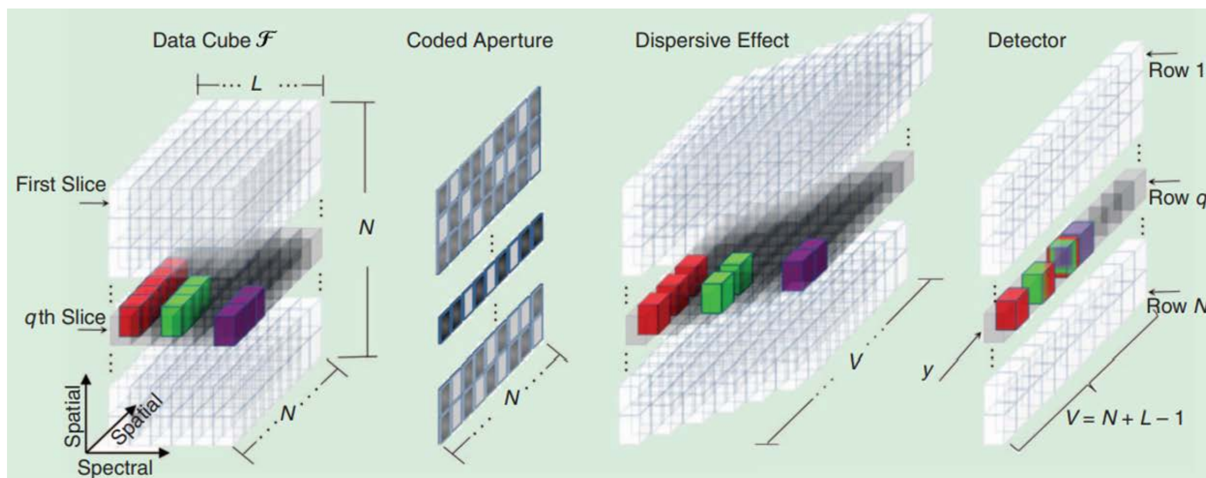

Figure 4.1. Spectral optical flow in coded aperture snapshot spectral imagers (CASSI).

Compressive sensing (CS) offers the ability to sense and reconstruct spectral scenes using significantly fewer measurements than traditional linear scanning spectral sensors [59–62]. This efficiency allows integrated CS imagers to capture hyperspectral images in an compressed data format directly from standard focal-plane arrays (FPAs), facilitating transmission at higher frame rates. Among the various approaches for compressive

sampling and reconstruction, one particularly notable CS-based architecture is the compressive coded aperture spectral imagers, also known as coded aperture snapshot spectral imagers (CASSI) [61–63]. Figure 4.1 provides an illustration of the spectral optical flow in CASSI [62]. A spectral data cube $\mathcal{F}$ having L spectral bands and $N \times N$ spatial pixels is first amplitude modulated by a pixelated $N \times N$ coded aperture T. In traditional hyperspectral imaging, capturing the entire voxel would necessitate $N \times N \times L$ measurements. However, in CASSI, $N \times N \times L$ dimensions of the spectral data cube are mapped to an array of $V \times N$ FPA measurements, where $V = N + L - 1$. This mapping takes advantage of the dispersion characteristics of the prism.

4.2 Design of polarization diversifying highly-dispersive metalens

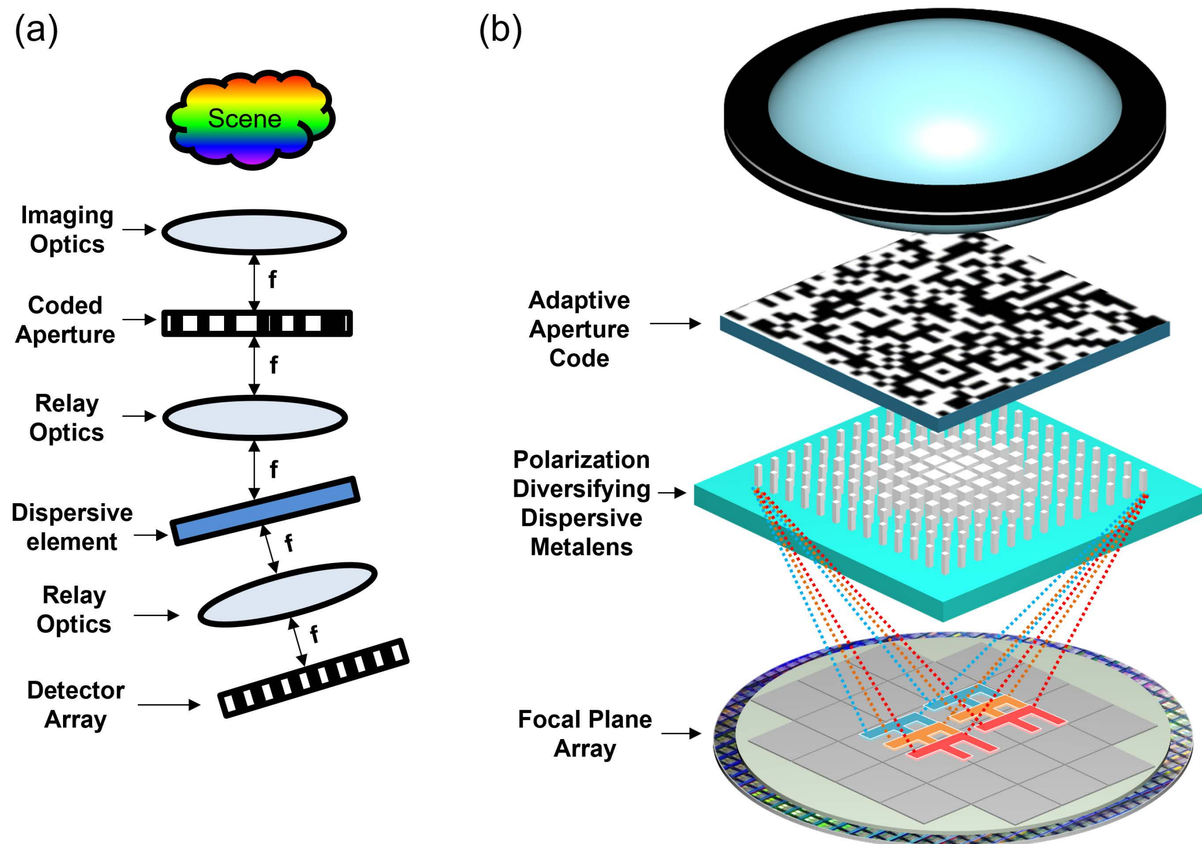

Figure 4.2. (a) Schematic of single dispersive CASSI. (b) Meta-CASSI.

Brady's group has applied the principle of CASSI to achieve a successful demonstration

of single dispersive CASSI [63], as depicted in Figure 4.2 (a). In our research, we introduce an exceptionally compact single dispersive CASSI system based on metalens technology, as depicted in Figure 4.2 (b). The proposed metalens-based CASSI employs a single metalens to replace both the two relay optics and the dispersive element found in the original single dispersive CASSI setup shown in Figure 4.2 (a). Additionally, the metalens is engineered to split images corresponding to the two polarizations.

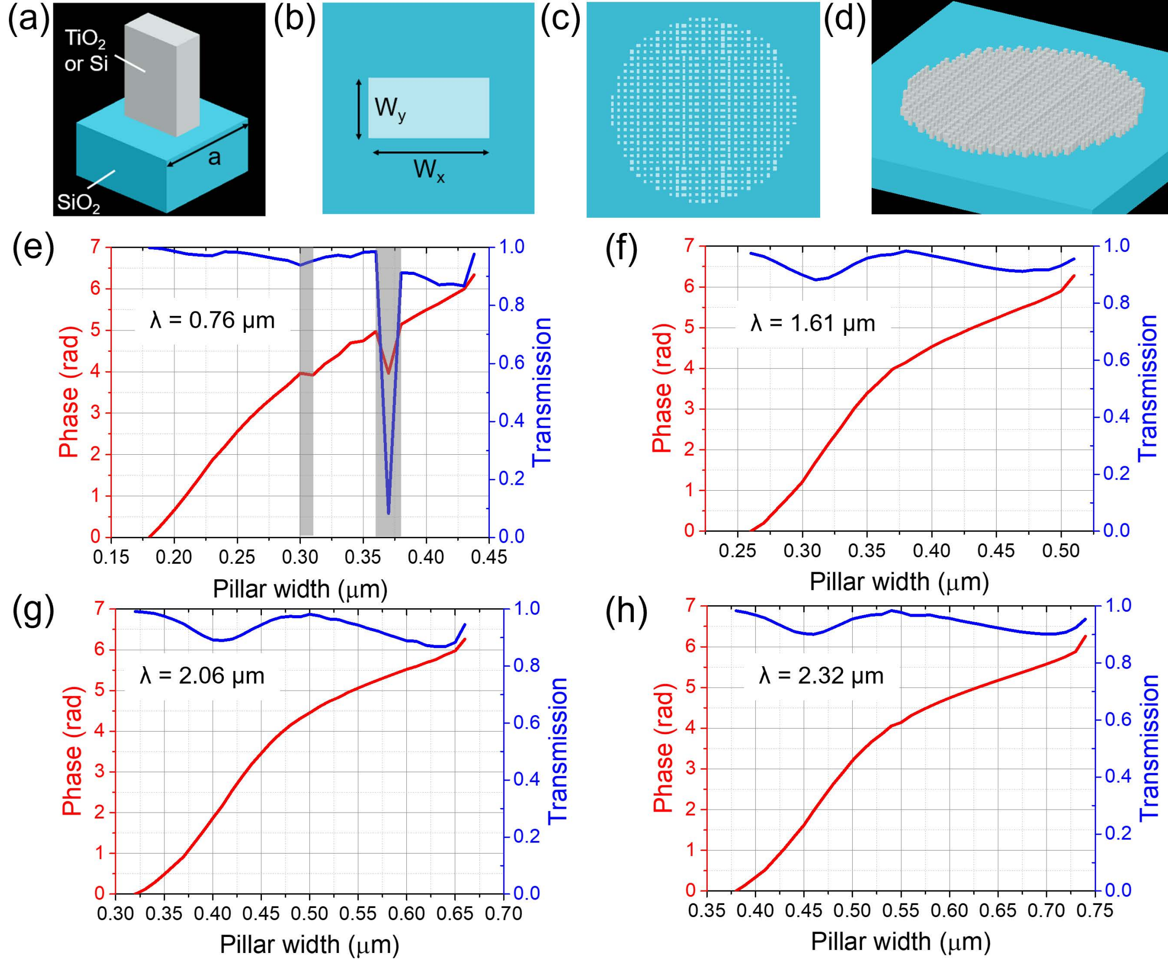

Figure 4.3. Schematic diagram of the metastructure (a-b) and metalens (c-d) with properly placed and sized dimensions to achieve (e-g) the desired phase shift of 0-2π while keeping the throughput nearly 100% for the four spectral bands. The pillar widths that sit in transmission dips (highlighted by gray stripes) are excluded from the design database.

By incorporating subwavelength 3D rectangular structure of Figure 4.3(a-b) of size w_x, w_y, and h, and placing them (Figure 4.3(c-d)) at the spacing to provide quadratic phase

shift shown in Figure 4.3(e-h), we can realize relatively highly dispersive dispersion lens with two linear polarizations split in two axial directions of the rectangular footprints. Here, TiO_2 metalens is used for the spectral band at around 0.76 μm, and Si metalenses are used for the other three spectral bands at around 1.61 μm, 2.06 μm, and 2.32 μm. The shift in the relative phase due to the metalens elements with respect to the center of the structure is given by $\varphi(x,y,\lambda) = \frac{2\pi}{\lambda}(f\text{-}\sqrt{x^2+y^2+f^2})$, where λ is the wavelength, f is the focal distance, x and y are the positions of each rectangular block. For the metalens design of 0.76 μm wavelength, the center-to-center distance is 0.48 μm and the height is 0.76 μm. By varying the element size from 0.18 μm to 0.44 μm, we can produce phase shift of 0-2π while keeping the throughput nearly 100%. Similarly, the metalenses designed for the other three spectral bands can be optimized as shown in Table 4.1.

Table 4.1. Metalens design parameters for the four spectral bands.

Center wavelength	Pillar material	Pillar height H	Unit cell size a	Pillar width W_{min}	Pillar width W_{max}
763.2 nm	TiO_2	0.76 μm	0.48 μm	0.18 μm	0.44 μm
1611.3 nm	Si	1.04 μm	0.72 μm	0.26 μm	0.51 μm
2065.0 nm	Si	1.28 μm	0.92 μm	0.32 μm	0.66 μm
2323.1 nm	Si	1.48 μm	1.08 μm	0.38 μm	0.74 μm

Figure 4.4 (a) and (b) show the proposed metalens with dispersive dispersion and polarization splitting in two axial directions. Simulation results vividly demonstrate the remarkable wavelength dispersion and polarization splitting achieved using a 140 μm diameter metalens while scanning wavelengths from 2170 nm to 2470 nm. Figure 4.4 (c-f) illustrates more detailed view of the dispersive focusing for the four wavelength bands designed for the spectral resolving power of $\sim$1000 (e.g. 2 nm spectral resolution at 2061 nm wavelength). This was accomplished using reasonably compact metalenses with a diameter of 2500*λ (e.g. D = 5 mm for λ = 2061 nm and D = 2 mm for λ = 763 nm wavelength). The off-axis focusing angle for these metalenses was designed to 22.5

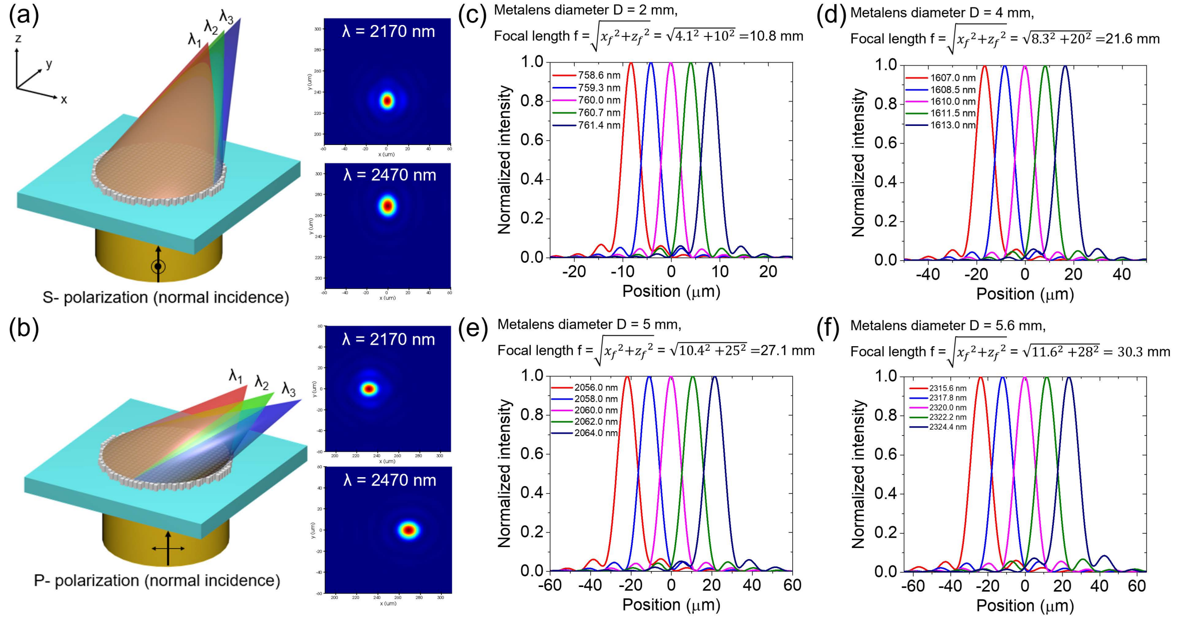

Figure 4.4. The rectangular metastructure design allows polarization diversifying as well as spectrally dispersive imaging as illustrated for (a) S-polarization and b) P-polarization at two different wavelengths. Calculated field intensity at the focal point for different wavelengths. Wavelength increases in steps from left to right for the four center wavelengths (c) 760 nm, (d) 1611 nm, (e) 2060 nm, and (f) 2320 nm.

degrees. With a larger metalens diameter, we anticipate achieving a spectral resolving power of ∼15,000.

Figure 4.5 displays the layout of the metalens designed for the center wavelength of 2323.1 nm. The intricate structures were defined and then converted into a GDSII format file using the Python module gdspy. In this configuration, Si metalenses are employed for spectral bands around 1.61 μm, 2.06 μm, and 2.32 μm, while TiO_2 metalens is used for spectral bands around 0.76 μm. The center-to-center distance in Figure 4.5 is 1.08 μm, with a height of 1.48 μm. By varying the element size from 0.38 μm to 0.74 μm, we can produce phase shift of 0-2π while keeping the throughput nearly 100%. The off-axis focusing angle for these metalenses was designed to be 22.5 degrees. For the initial metalens testing, $F/5$ design was chosen with the diameter of 5 mm, 10 mm, and 20 mm. These 20 mm metalenses for the four spectral bands (0.76 μm, 1.61 μm, 2.06 μm, and 2.32 μm) are expected to achieve the spectral resolving power of 10000, 5000, 4000, 3571, respectively.

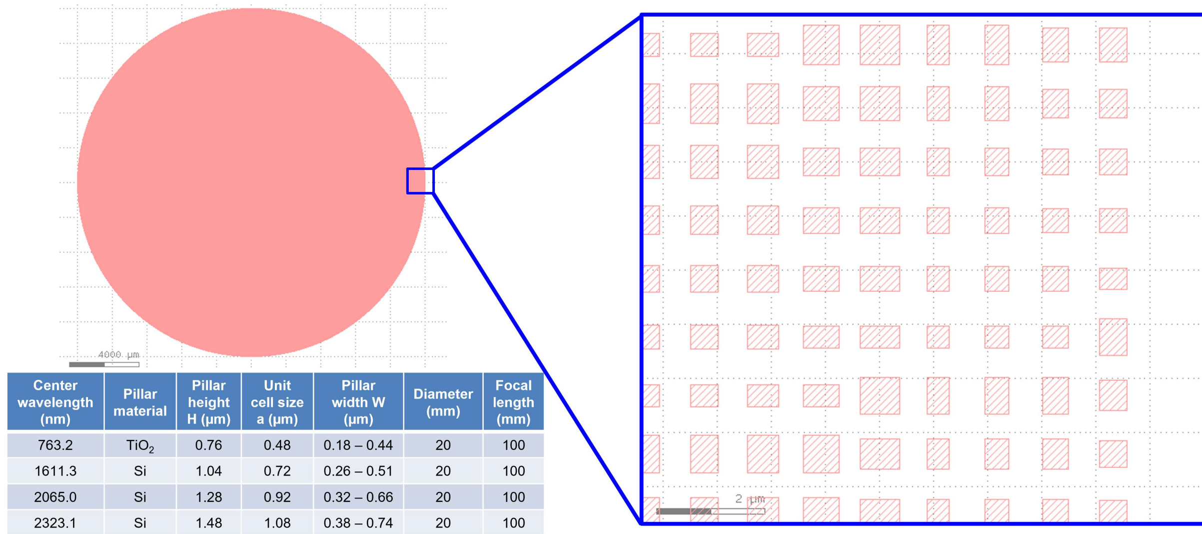

Center wavelength (nm)	Pillar material	Pillar height H (μm)	Unit cell size a (μm)	Pillar width W (μm)	Diameter (mm)	Focal length (mm)
763.2	TiO_2	0.76	0.48	0.18 – 0.44	20	100
1611.3	Si	1.04	0.72	0.26 – 0.51	20	100
2065.0	Si	1.28	0.92	0.32 – 0.66	20	100
2323.1	Si	1.48	1.08	0.38 – 0.74	20	100

Figure 4.5. Metalens layout for the center wavelength of 2323.1 nm and the design parameters for the F/5 metalenses at the four spectral bands 0.76 μm, 1.61 μm, 2.06 μm, and 2.32 μm.

4.3 Characterization results of on-axis and off-axis metalenses

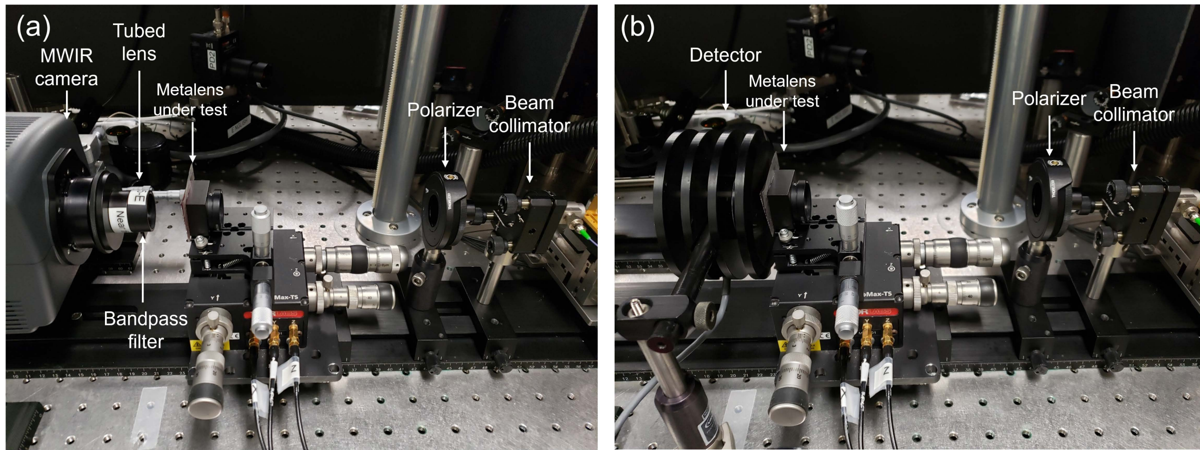

Figure 4.6. Measurement setups for (a) beam profile and (b) transmission.

We designed the measurement setups to characterize both the output beam profiles and the corresponding transmission efficiency of the fabricated metalens, as illustrated in Figure 4.6 (a) and (b), respectively. In our setup, we employed a 1937 nm distributed-feedback (DFB) laser to characterize the metalens, which was designed for a wavelength of 2.06 μm. The laser beam was collimated using a silver reflective collimator (Thorlabs,

RC02APC-P01) to generate a 1.8 mm diameter collimated beam. To ensure linear polarization, a polarizer (Thorlabs, LPNIR050) was used. After the light passes through the metalens, the output beam pattern was captured by an MWIR camera (FLIR, A6700). Additionally, we measured the corresponding transmission efficiency using a thermopile sensor with a 19 mm diameter active area (Coherent, PM30).

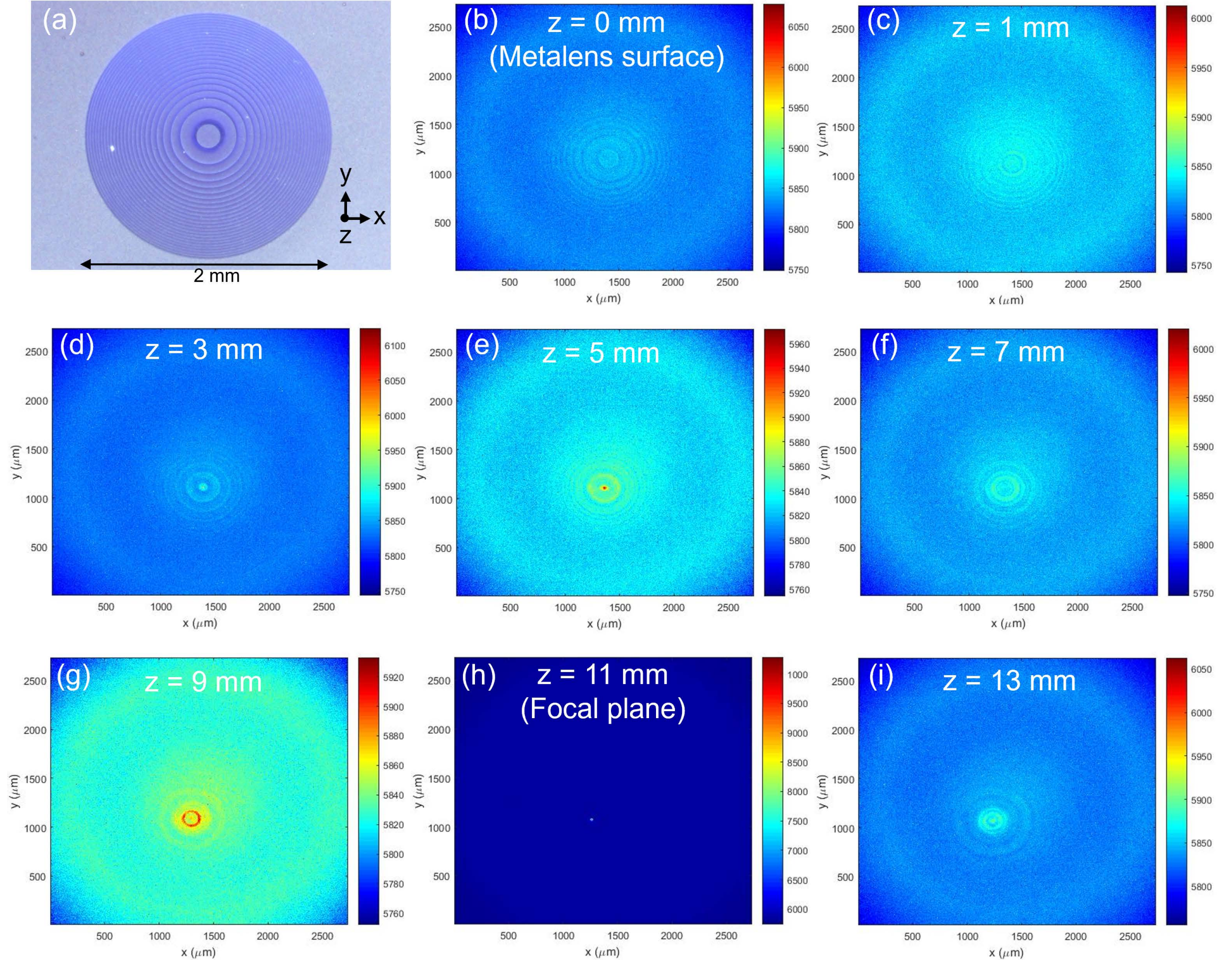

Figure 4.7. (a) Top-view microscope image for the fabricated on-axis metalens with a diameter of 2 mm. (b-i) Measured beam patterns at various positions away from the metalens.

Figure 4.7 (a) shows the on-axis metalens that was fabricated for investigating its focusing effect. This metalens has a diameter of 2 mm, a focal length of 10 mm, and it is designed for a wavelength of 2.06 μm. In Figure 4.7 (b-i), we present beam patterns at various positions along the optical axis of the metalens. We observed that the beam focuses at a distance of 11 mm away from the metalens, which closely matches the

simulation result of 10.63 mm as shown in Figure 4.8 (a). Furthermore, the measured transmission efficiency of the metalens is approximately 46 %.

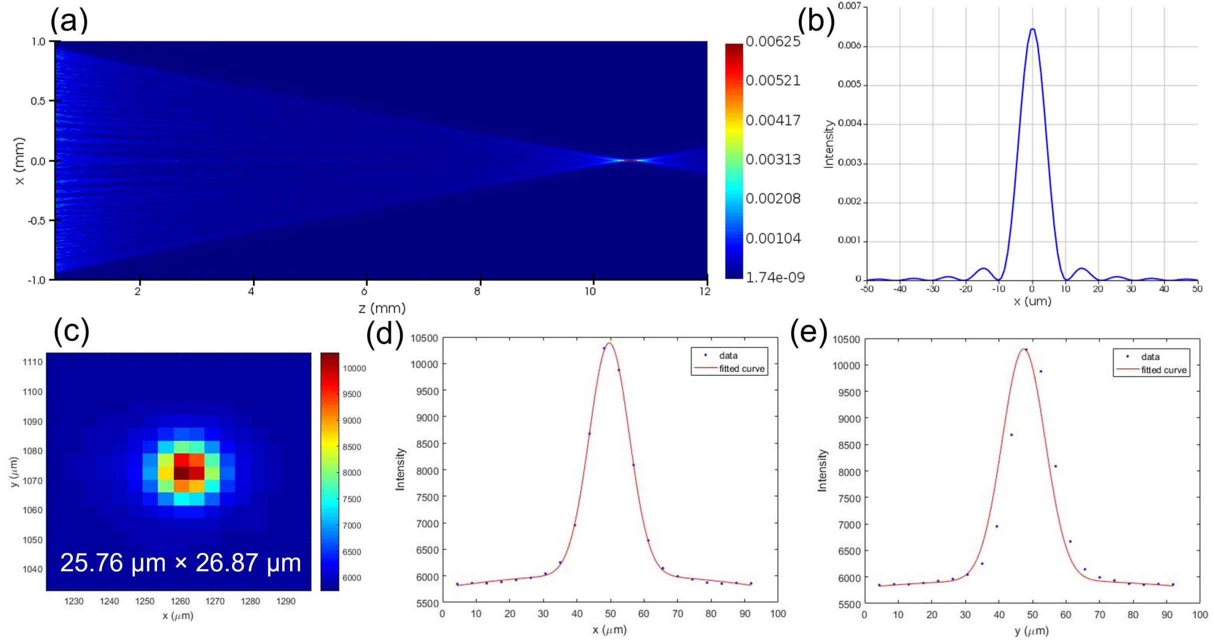

Figure 4.8. (a) Simulated light propagation on the x-z plane and (b) the simulated beam profile in the focal plane along x-axis. (c) Measured beam profiles in the focal plane of the metelens along (d) x-axis and (e) y-axis with Gaussian distribution fitting.

In Figure 4.8 (b) and (c), we present the simulated and measured beam profiles in the focal plane of the metalens. The simulated results indicate a focal spot size of 14.6 μm size for the focal spot. However, due to the lower resolution of the measured beam profile, we utilized Gaussian fitting, as depicted in Figure 4.8 (d) and (e), to estimate the size of the focal spot. This estimation resulted in a beam diameter of approximately 26 μm, nearly double the size indicated by the simulation results. This disparity can be attributed to fabrication defects.

After assessing the performance of the on-axis metalens, we now turn our attention to investigating the capabilities of the off-axis metalens in terms of polarization splitting and wavelength dispersion. In Figure 4.9 (a), we present the initial demonstration of an off-axis metalens with a 2 mm diameter, 6 mm focal length, and an off-axis focusing angle of 22.5 degrees. The designed wavelength for this metalens is also 2.06 μm. Figure 4.9 (b) displays the calculated field intensity at the focal plane of the metalens under different

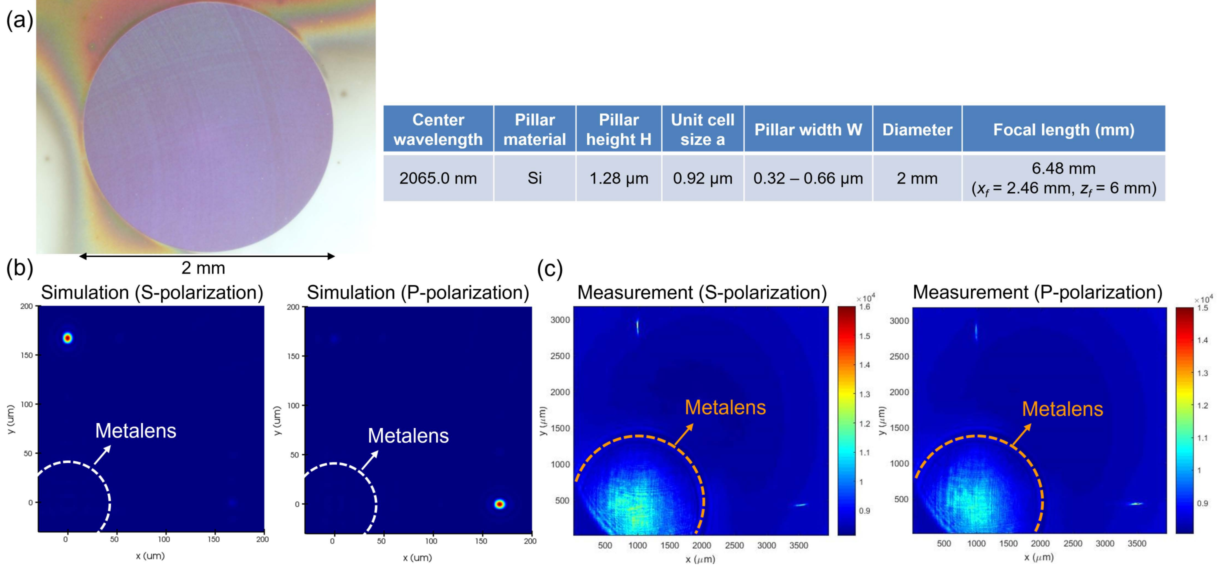

Center wavelength	Pillar material	Pillar height H	Unit cell size a	Pillar width W	Diameter	Focal length (mm)
2065.0 nm	Si	1.28 μm	0.92 μm	0.32 – 0.66 μm	2 mm	6.48 mm (x_f = 2.46 mm, z_f = 6 mm)

Figure 4.9. (a) Top-view microscope image for the fabricated off-axis metalens. Calculated and measured field intensity at the focal point for two polarizations are shown in (b) and (c) respectively.

polarizations for comparison with the measurement results shown in Figure 4.9 (c). For a decent simulation time, we scaled down the metalens diameter to 140 μm while maintaining the same focal ratio and off-axis angle. The measurement results for the 2-mm diameter metalens demonstrate the expected capability of polarization splitting in two axial directions, as seen in the simulation. However, the intensity contrast between the two polarizations is lower than what we anticipated from the simulation. This could be due to fabrication defects, and therefore, requires further improvement.

In Figure 4.10 (a), we present the calculated beam profiles in the focal plane of the metalens, with an estimated spot size of approximately 11.2 μm. Notably, the focal spot experiences a 3 μm shift along the y-axis as the wavelength is scanned from 1935 nm to 1937 nm. Regarding the measurement result, Figure 4.10 (b) displays a spot size of approximately 210 μm and a shift of about 12 μm along the y-axis as the wavelength undergoes scanning from 1935 nm to 1937 nm. The significant disparity between the simulation and measurement results can be attributed to underetched metalens elements, highlighting the need for further improvement.

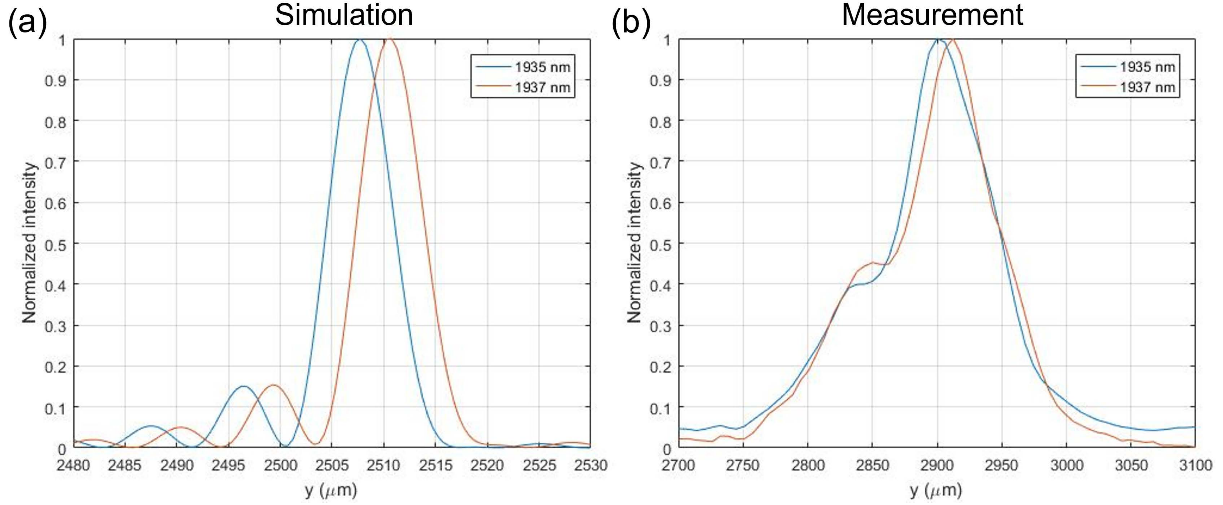

Figure 4.10. (a) Calculated and (b) measured beam profiles at the focal plane for S-polarization as the wavelength scans from 1935 nm to 1937 nm.

4.4 Summary

In summary, we have designed polarization-diversifying highly-dispersive metalenses for four spectral bands at 0.76 μm, 1.61 μm, 2.06 μm, and 2.32 μm to enable compressive hyperspectral imaging. With a diameter of 20 mm, these metalenses can achieve spectral resolving powers of 10000, 5000, 4000, 3571, respectively. Our initial step involved fabricating an on-axis metalens to demonstrate its focusing capabilities. The measurement results aligned closely with the simulations, and we achieved a transmission efficiency of 46 %. Subsequently, we fabricated an off-axis metalens to explore polarization diversity and spectral dispersion in imaging. Our findings reveal clear polarization splitting for both S-polarization and P-polarization. When scanning the wavelength from 1935 nm to 1937 nm, we observed a 12 μm shift in the focal spot along the focal plane of the metalens. These results underscore the promising potential of realizing highly dispersive and polarization-sensitive metalenses and metalens-based CASSI systems enabling compact hyperspectral imaging.

Chapter 5

Conclusion and Future Directions

In this dissertation, we have achieved significant milestones in the development of 3D photonic integration, harnessing a diverse range of cutting-edge technologies, including ultrafast laser inscription, optical phased arrays, and metalenses.

For ultrafast laser inscription, we demonstrated arbitrary vertical waveguides in deposited oxide on silicon substrate with impressive low propagation loss of 0.62 dB/cm and efficient chip-to-chip coupling to SiN inverse tapers. Future endeavors could focus on further refining the inscription conditions of ULI waveguides intended for intra-chip coupling with SiN couplers. Besides, we could explore the potential of alternative materials for laser inscription like various doped glasses and SU-8 photoresist with the objective of advancing the field of 3D photonic packaging. In addition to the previous achievements, we introduced a 3D fan-in/fan-out device designed for multi-core fiber integration with SMF-28 fiber arrays. Our innovative waveguide routing algorithm for ultrafast laser inscription allowed us to maintain consistent photonic path lengths while optimizing waveguide bending. With promising outcomes, we achieved low propagation losses of 0.3 dB/cm on boro-aluminosilicate glass and even lower losses of 0.16 dB/cm on germanium-oxide doped glass. A critical consideration for effective packaging involves the rapid and precise alignment of SMF-28 fiber arrays and multi-core fibers. Future directions may include investigating the creation of efficient sockets to facilitate the coupling of light into or from the 3D fan-in/fan-out device fabricated using ultrafast laser inscription. Moreover, we presented the first-ever demonstration of a 3D arrayed waveguide grating router op-

erating at 1550 nm, achieved through ultrafast laser inscription. Leveraging multi-scan technique, we obtained a refractive index contrast of 8.8×10^{-3} and realized a AWGR with impressive channel spacing of 399.1 GHz and a 3 dB-passband width of 2.02 nm. The AWGR is further integrated with a fan-in/fan-out structure to exhibit its versatility for 3D photonic integration. The future works could concentrate on the ongoing optimization of optical losses generated from each component within the AWGR. Additionally, our research will delve into identifying and mitigating phase errors induced in the arrayed waveguides, further advancing this innovative technology.

In our optical beam steering research, we achieved significant milestones. Firstly, we developed a 24-channel OPA with an emitting area of 5 mm and a waveguide pitch as small as 1.3 μm. Our experiments resulted in remarkable outcomes, including a 3.3° axial beam steering achieved through a 20 nm wavelength tuning, and an impressive lateral beam steering capability exceeding 40°. Importantly, this lateral steering exhibited no sidelobes within the ±33° field-of-regard. These achievements pave the way for scalability, allowing us to scale up such devices to a 1 cm × 1 cm footprint and utilize them as unit cells in larger assemblies. Furthermore, employing vertical U-shaped couplers [57], we have the potential to tile these unit cells to create large coherent apertures, such as 10 cm × 10 cm configurations, for advanced long-range LIDAR systems. Second, we presented the first demonstration of 2D beam steering in MWIR using a germanium-silicon photonic platform. Our breakthrough includes the successful presentation of a fully packaged non-mechanical beam-steering device featuring a 2-mm-long 12-channel grating emitter array. This accomplishment has resulted in a remarkable reduction in beam divergence, achieving as low as 0.18° in the perpendicular direction, with wavelength tunability of 0.069°/nm. In the lateral direction, we demonstrated a substantial beam-steering angle of 12.7° with a beam divergence of 0.47°×2.86°. To further enhance the performance of the grating emitters, we intend to customize the grating structures to create a uniform emitting profile and introduce reflectors beneath the emitters to increase emitting efficiency. We anticipate that the same approach can be effectively employed to design LWIR beam steering devices. This groundbreaking development extends the operational capabilities

of OPA for FSOC and gas sensing with MWIR with low sensitivity to the atmosphere turbulence and scintillation. Additionally, our device is fully compatible with the CMOS process for large-scale fabrication and electronic co-integration. Our future work will focus on increasing the number of the channels and decreasing the pitch for the emitter array. Last, We have successfully demonstrated beam steering devices that are compatible with foundry processes. These devices utilize 2D optical phased arrays operating at wavelengths of 3.8 μm and 4.6 μm. Our meticulous design involved a 64×64 PEPA with integrated transistors, which was based on a Ge-on-SOI platform. After being fabricated by a commercial foundry, these devices were fully packaged on printed circuit boards utilizing the wire bonding technique. To assess their performance in beam steering, we conducted rigorous characterization using an MWIR optical testing bench. For the future work, it is essential to delve deeper into the investigation of propagation loss and bending loss of the Ge waveguides used in the PEPA devices. By thoroughly understanding and optimizing these factors, we can make significant advancements in enhancing the performance of the PEPA devices. Additionally, a significant aspect of our future research will focus on the complete development of 45° reflectors, as this development will enable the demonstration of fully functional PEPA devices.

For metalenses, we developed polarization-diversifying highly-dispersive metalenses tailored for four distinct spectral bands at 0.76 μm, 1.61 μm, 2.06 μm, and 2.32 μm, with the primary objective of facilitating compressive hyperspectral imaging. These metalenses with a 20 mm diameter can deliver impressive spectral resolving powers of 10,000, 5,000, 4,000, and 3,571, respectively. Our initial phase involved the fabrication of an on-axis metalens to validate its focusing capabilities, with measurement results closely aligning with simulations and a transmission efficiency of 46 %. Subsequently, we extended our efforts to create an off-axis metalens for polarization diversity and spectral dispersion in imaging. The characterization unveiled clear polarization splitting for both S-polarization and P-polarization. As we scanned the wavelength across the range from 1935 nm to 1937 nm, a significant 12 μm shift in the focal spot along the focal plane of the metalens was observed. These outcomes pave the way for metalens-based CASSI systems that

promise compact and efficient hyperspectral imaging solutions. Our future prospects involve further refinements in metalens design and fabrication techniques to enhance their performance and broaden their applicability in hyperspectral imaging systems.

References

[1] [Online]. Available: https://ic.tweakimg.net/ext/i.dsp/1109883395.png

[2] S. Behere and M. Törngren, "A functional architecture for autonomous driving," in *Proceedings of the First International Workshop on Automotive Software Architecture*, 2015, pp. 3–10.

[3] S. Yoo, B. Guan, and R. P. Scott, "Heterogeneous 2d/3d photonic integrated microsystems," *Microsystems & Nanoengineering*, vol. 2, no. 1, pp. 1–9, 2016.

[4] N. Lindenmann, G. Balthasar, D. Hillerkuss, R. Schmogrow, M. Jordan, J. Leuthold, W. Freude, and C. Koos, "Photonic wire bonding: a novel concept for chip-scale interconnects," *Optics express*, vol. 20, no. 16, pp. 17 667–17 677, 2012.

[5] M. Khorasaninejad and F. Capasso, "Metalenses: Versatile multifunctional photonic components," *Science*, vol. 358, no. 6367, p. eaam8100, 2017.

[6] W. T. Chen, A. Y. Zhu, V. Sanjeev, M. Khorasaninejad, Z. Shi, E. Lee, and F. Capasso, "A broadband achromatic metalens for focusing and imaging in the visible," *Nature nanotechnology*, vol. 13, no. 3, pp. 220–226, 2018.

[7] R. Osellame, G. Cerullo, and R. Ramponi, *Femtosecond laser micromachining: photonic and microfluidic devices in transparent materials*. Springer, 2012, vol. 123.

[8] I.-B. Sohn, H.-K. Choi, Y.-C. Noh, J. Kim, and M. S. Ahsan, "Laser assisted fabrication of micro-lens array and characterization of their beam shaping property," *Applied Surface Science*, vol. 479, pp. 375–385, 2019.

[9] H.-K. Choi, M. S. Ahsan, D. Yoo, I.-B. Sohn, Y.-C. Noh, J.-T. Kim, D. Jung, J.-H. Kim, and H.-M. Kang, "Formation of cylindrical micro-lens array on fused silica glass surface using co2 laser assisted reshaping technique," *Optics & Laser Technology*, vol. 75, pp. 63–70, 2015.

[10] F. Sima, K. Sugioka, R. M. Vázquez, R. Osellame, L. Kelemen, and P. Ormos, "Three-dimensional femtosecond laser processing for lab-on-a-chip applications," *Nanophotonics*, vol. 7, no. 3, pp. 613–634, 2018.

[11] A. Martinez, M. Dubov, I. Khrushchev, and I. Bennion, "Direct writing of fibre bragg gratings by femtosecond laser," *Electronics letters*, vol. 40, no. 19, p. 1, 2004.

[12] A. Martinez, I. Khrushchev, and I. Bennion, "Thermal properties of fibre bragg gratings inscribed point-by-point by infrared femtosecond laser," *Electronics letters*, vol. 41, no. 4, pp. 176–178, 2005.

[13] A. Lacraz, M. Polis, A. Theodosiou, C. Koutsides, and K. Kalli, "Femtosecond laser inscribed bragg gratings in low loss cytop polymer optical fiber," *IEEE Photonics Technology Letters*, vol. 27, no. 7, pp. 693–696, 2015.

[14] D. Grobnic, C. W. Smelser, S. J. Mihailov, and R. B. Walker, "Long-term thermal stability tests at 1000 c of silica fibre bragg gratings made with ultrafast laser radiation," *Measurement Science and Technology*, vol. 17, no. 5, p. 1009, 2006.

[15] R. R. Thomson, H. T. Bookey, N. D. Psaila, A. Fender, S. Campbell, W. N. Macpherson, J. S. Barton, D. T. Reid, and A. K. Kar, "Ultrafast-laser inscription of a three dimensional fan-out device for multicore fiber coupling applications," *Optics express*, vol. 15, no. 18, pp. 11 691–11 697, 2007.

[16] G. Djogo, J. Li, S. Ho, M. Haque, E. Ertorer, J. Liu, X. Song, J. Suo, and P. R. Herman, "Femtosecond laser additive and subtractive micro-processing: enabling a high-channel-density silica interposer for multicore fibre to silicon-photonic packaging," *International Journal of Extreme Manufacturing*, vol. 1, no. 4, p. 045002, 2019.

[17] M. C. Wu, O. Solgaard, and J. E. Ford, "Optical mems for lightwave communication," *Journal of Lightwave Technology*, vol. 24, no. 12, pp. 4433–4454, 2006.

[18] Y. Pan, H. Xie, and G. K. Fedder, "Endoscopic optical coherence tomography based on a microelectromechanical mirror," *Optics letters*, vol. 26, no. 24, pp. 1966–1968, 2001.

[19] N. R. Smith, D. C. Abeysinghe, J. W. Haus, and J. Heikenfeld, "Agile wide-angle beam steering with electrowetting microprisms," *Optics Express*, vol. 14, no. 14, pp. 6557–6563, 2006.

[20] S. R. Davis, S. D. Rommel, D. Gann, B. Luey, J. D. Gamble, M. Ziemkiewicz, and M. Anderson, "A lightweight, rugged, solid state laser radar system enabled by non-mechanical electro-optic beam steerers," in *Laser Radar Technology and Applications XXI*, vol. 9832. SPIE, 2016, pp. 186–196.

[21] M. J. Heck, "Highly integrated optical phased arrays: photonic integrated circuits for optical beam shaping and beam steering," *Nanophotonics*, vol. 6, no. 1, pp. 93–107, 2017.

[22] C. V. Poulton, A. Yaacobi, D. B. Cole, M. J. Byrd, M. Raval, D. Vermeulen, and M. R. Watts, "Coherent solid-state lidar with silicon photonic optical phased arrays," *Optics letters*, vol. 42, no. 20, pp. 4091–4094, 2017.

[23] C. V. Poulton, M. J. Byrd, M. Raval, Z. Su, N. Li, E. Timurdogan, D. Coolbaugh, D. Vermeulen, and M. R. Watts, "Large-scale silicon nitride nanophotonic phased arrays at infrared and visible wavelengths," *Optics letters*, vol. 42, no. 1, pp. 21–24, 2017.

[24] S. Chung, H. Abediasl, and H. Hashemi, "A monolithically integrated large-scale optical phased array in silicon-on-insulator cmos," *IEEE Journal of Solid-State Circuits*, vol. 53, no. 1, pp. 275–296, 2017.

[25] D. N. Hutchison, J. Sun, J. K. Doylend, R. Kumar, J. Heck, W. Kim, C. T. Phare, A. Feshali, and H. Rong, "High-resolution aliasing-free optical beam steering," *Optica*, vol. 3, no. 8, pp. 887–890, 2016.

[26] J. Hulme, J. Doylend, M. Heck, J. Peters, M. Davenport, J. Bovington, L. Coldren, and J. Bowers, "Fully integrated hybrid silicon two dimensional beam scanner," *Optics express*, vol. 23, no. 5, pp. 5861–5874, 2015.

[27] M. Khorasaninejad, W. T. Chen, R. C. Devlin, J. Oh, A. Y. Zhu, and F. Capasso, "Metalenses at visible wavelengths: Diffraction-limited focusing and subwavelength resolution imaging," *Science*, vol. 352, no. 6290, pp. 1190–1194, 2016.

[28] M. Khorasaninejad, A. Y. Zhu, C. Roques-Carmes, W. T. Chen, J. Oh, I. Mishra, R. C. Devlin, and F. Capasso, "Polarization-insensitive metalenses at visible wavelengths," *Nano letters*, vol. 16, no. 11, pp. 7229–7234, 2016.

[29] M. Khorasaninejad, W. Chen, A. Zhu, J. Oh, R. Devlin, D. Rousso, and F. Capasso, "Multispectral chiral imaging with a metalens," *Nano letters*, vol. 16, no. 7, pp. 4595–4600, 2016.

[30] R. C. Devlin, M. Khorasaninejad, W. T. Chen, J. Oh, and F. Capasso, "Broadband high-efficiency dielectric metasurfaces for the visible spectrum," *Proceedings of the National Academy of Sciences*, vol. 113, no. 38, pp. 10 473–10 478, 2016.

[31] S. M. Eaton, G. Cerullo, and R. Osellame, "Fundamentals of femtosecond laser modification of bulk dielectrics," in *Femtosecond Laser Micromachining: Photonic and Microfluidic Devices in Transparent Materials*. Springer, 2011, pp. 3–18.

[32] R. R. Thomson, N. D. Psaila, H. T. Bookey, D. T. Reid, and A. K. Kar, "Controlling the cross-section of ultrafast laser inscribed optical waveguides," *Femtosecond Laser Micromachining: Photonic and Microfluidic Devices in Transparent Materials*, pp. 93–125, 2012.

[33] Y. Nasu, M. Kohtoku, and Y. Hibino, "Low-loss waveguides written with a femtosecond laser for flexible interconnection in a planar light-wave circuit," *Optics letters*, vol. 30, no. 7, pp. 723–725, 2005.

[34] Y. Nasu, M. Kohtoku, Y. Hibino, and Y. Inoue, "Waveguide interconnection in silica-based planar lightwave circuit using femtosecond laser," *Journal of lightwave technology*, vol. 27, no. 18, pp. 4033–4039, 2009.

[35] T. Hayashi, T. Taru, O. Shimakawa, T. Sasaki, and E. Sasaoka, "Design and fabrication of ultra-low crosstalk and low-loss multi-core fiber," *Optics express*, vol. 19, no. 17, pp. 16 576–16 592, 2011.

[36] K. Saitoh and S. Matsuo, "Multicore fiber technology," *Journal of Lightwave Technology*, vol. 34, no. 1, pp. 55–66, 2016.

[37] M. Koshiba, K. Saitoh, and Y. Kokubun, "Heterogeneous multi-core fibers: proposal and design principle," *IEICE Electronics Express*, vol. 6, no. 2, pp. 98–103, 2009.

[38] B. J. Puttnam, R. S. Luis, W. Klaus, J. Sakaguchi, J.-M. D. Mendinueta, Y. Awaji, N. Wada, Y. Tamura, T. Hayashi, M. Hirano *et al.*, "2.15 pb/s transmission using a 22 core homogeneous single-mode multi-core fiber and wideband optical comb," in *2015 European Conference on Optical Communication (ECOC)*. IEEE, 2015, pp. 1–3.

[39] L. Carroll, J.-S. Lee, C. Scarcella, K. Gradkowski, M. Duperron, H. Lu, Y. Zhao, C. Eason, P. Morrissey, M. Rensing *et al.*, "Photonic packaging: transforming silicon photonic integrated circuits into photonic devices," *Applied Sciences*, vol. 6, no. 12, p. 426, 2016.

[40] Y.-C. Ling, Y. Zhang, and S. B. Yoo, "Arbitrary vertical low-loss waveguides in deposited oxide of optical interposers for low-loss 3d photonic packaging," in *CLEO: Science and Innovations*. Optical Society of America, 2018, pp. STh3I–4.

[41] S. Cheung, T. Su, K. Okamoto, and S. Yoo, "Ultra-compact silicon photonic 512× 512 25 ghz arrayed waveguide grating router," *IEEE Journal of Selected Topics in Quantum Electronics*, vol. 20, no. 4, pp. 310–316, 2013.

[42] Y. Sano and T. Yoshino, "Fast optical wavelength interrogator employing arrayed waveguide grating fordistributed fiber bragg grating sensors," *Journal of Lightwave Technology*, vol. 21, no. 1, p. 132, 2003.

[43] P. Cheben, J. Schmid, A. Delâge, A. Densmore, S. Janz, B. Lamontagne, J. Lapointe, E. Post, P. Waldron, and D.-X. Xu, "A high-resolution silicon-on-insulator arrayed waveguide grating microspectrometer with sub-micrometer aperture waveguides," *Optics express*, vol. 15, no. 5, pp. 2299–2306, 2007.

[44] G. Douglass, F. Dreisow, S. Gross, S. Nolte, and M. Withford, "Towards femtosecond laser written arrayed waveguide gratings," *Optics express*, vol. 23, no. 16, pp. 21 392–21 402, 2015.

[45] G. Douglass, F. Dreisow, S. Gross, and M. Withford, "Femtosecond laser written arrayed waveguide gratings with integrated photonic lanterns," *Optics express*, vol. 26, no. 2, pp. 1497–1505, 2018.

[46] C. V. Poulton, A. Yaacobi, D. B. Cole, M. J. Byrd, M. Raval, D. Vermeulen, and M. R. Watts, "Coherent solid-state lidar with silicon photonic optical phased arrays," *Optics letters*, vol. 42, no. 20, pp. 4091–4094, 2017.

[47] J. Sun, E. Timurdogan, A. Yaacobi, E. S. Hosseini, and M. R. Watts, "Large-scale nanophotonic phased array," *Nature*, vol. 493, no. 7431, pp. 195–199, 2013.

[48] K. Van Acoleyen, W. Bogaerts, J. Jágerská, N. Le Thomas, R. Houdré, and R. Baets,

"Off-chip beam steering with a one-dimensional optical phased array on silicon-on-insulator," *Optics letters*, vol. 34, no. 9, pp. 1477–1479, 2009.

[49] T. Komljenovic and P. Pintus, "On-chip calibration and control of optical phased arrays," *Optics express*, vol. 26, no. 3, pp. 3199–3210, 2018.

[50] J. Hecht, "Lidar for self-driving cars," *Optics and Photonics News*, vol. 29, no. 1, pp. 26–33, 2018.

[51] P. F. Ambrico, A. Amodeo, P. Di Girolamo, and N. Spinelli, "Sensitivity analysis of differential absorption lidar measurements in the mid-infrared region," *Applied optics*, vol. 39, no. 36, pp. 6847–6865, 2000.

[52] E. Leitgeb, T. Plank, M. S. Awan, P. Brandl, W. Popoola, Z. Ghassemlooy, F. Ozek, and M. Wittig, "Analysis and evaluation of optimum wavelengths for free-space optical transceivers," in *2010 12th International Conference on Transparent Optical Networks*. IEEE, 2010, pp. 1–7.

[53] P. Corrigan, R. Martini, E. A. Whittaker, and C. Bethea, "Quantum cascade lasers and the kruse model in free space optical communication," *Optics Express*, vol. 17, no. 6, pp. 4355–4359, 2009.

[54] C. A. Balanis, *Antenna theory: analysis and design*. John wiley & sons, 2015.

[55] P. Cheben, R. Halir, J. H. Schmid, H. A. Atwater, and D. R. Smith, "Subwavelength integrated photonics," *Nature*, vol. 560, no. 7720, pp. 565–572, 2018.

[56] R. Soref, "Mid-infrared photonics in silicon and germanium," *Nature photonics*, vol. 4, no. 8, pp. 495–497, 2010.

[57] Y. Zhang, Y.-C. Ling, Y. Zhang, K. Shang, and S. B. Yoo, "High-density wafer-scale 3-d silicon-photonic integrated circuits," *IEEE Journal of Selected Topics in Quantum Electronics*, vol. 24, no. 6, pp. 1–10, 2018.

[58] K. Shang, C. Qin, Y. Zhang, G. Liu, X. Xiao, S. Feng, and S. Yoo, "Uniform emission, constant wavevector silicon grating surface emitter for beam steering with ultra-sharp instantaneous field-of-view," *Optics express*, vol. 25, no. 17, pp. 19 655–19 661, 2017.

[59] M. E. Gehm, R. John, D. J. Brady, R. M. Willett, and T. J. Schulz, "Single-shot compressive spectral imaging with a dual-disperser architecture," *Optics express*, vol. 15, no. 21, pp. 14 013–14 027, 2007.

[60] H. Arguello, H. F. Rueda, and G. R. Arce, "Spatial super-resolution in code aperture spectral imaging," in *Compressive Sensing*, vol. 8365. Spie, 2012, pp. 43–48.

[61] D. J. Brady, *Optical imaging and spectroscopy*. John Wiley & Sons, 2009.

[62] G. R. Arce, D. J. Brady, L. Carin, H. Arguello, and D. S. Kittle, "Compressive

coded aperture spectral imaging: An introduction," *IEEE Signal Processing Magazine*, vol. 31, no. 1, pp. 105–115, 2013.

[63] A. Wagadarikar, R. John, R. Willett, and D. Brady, "Single disperser design for coded aperture snapshot spectral imaging," *Applied optics*, vol. 47, no. 10, pp. B44–B51, 2008.